Tuning in on cosmic rays

Polarization of radio signals from air showers as a probe of emission mechanisms

ISBN: 978–90–9027039–5

Cover illustration: Sunset at the Balloon Launching Station, Harm Schoorlemmer (2008)

This work is part of the research programme of the Foundation for Fundamental Research on Matter (FOM), which is part of the Netherlands Organisation for Scientific Research (NWO).

Tuning in on cosmic rays

Polarization of radio signals from air showers as a probe of emission mechanisms

Proefschrift

ter verkrijging van de graad van doctor
aan de Radboud Universiteit Nijmegen
op gezag van de rector magnificus
prof. mr. S. C. J. J. Kortmann,
volgens besluit van het College van Decanen
in het openbaar te verdedigen op vrijdag 14 september 2012
om 10.30 uur precies

door

Harm Schoorlemmer

geboren op 8 januari 1983
te Bennebroek

Promotor: Prof. dr. S. J. de Jong

Copromotor: Dr. C. W. J. P. Timmermans

Manuscriptcommissie: Prof. dr. H. Falcke

Prof. dr. O. Scholten
— Rijksuniversiteit Groningen

Prof. dr. A. Letessier-Selvon
— Laboratoire de Physique Nucléaire
et de Hautes Energies, Paris

Prof. dr. A. A. Watson
— University of Leeds

Prof. dr. F. L. Linde
— Nikhef, Amsterdam

Contents

1 General Introduction **1**

2 Theory **5**
- 2.1 Radio emission from extensive air showers 5
- 2.2 Shower development and particle distribution functions . . 6
- 2.3 Geomagnetic mechanism 10
- 2.4 Charge-excess mechanism 13
- 2.5 Cherenkov effect 15
- 2.6 Interference and polarization. 16

3 Detectors **21**
- 3.1 The Pierre Auger Observatory 21
- 3.2 Radio detectors 25
  - 3.2.1 First prototype at the Balloon Launching Station (BLS 2007 / 2008) 27
  - 3.2.2 Multiple Antenna eXperiment In Malargüe Argentina (MAXIMA) 29
  - 3.2.3 Auger Engineering Radio Array (AERA) 31
- 3.3 From ADC value to an electric field 33

4 Data sets and event selection **39**
- 4.1 Surface detector event selection 40
- 4.2 Surface detector - radio detector coincidences 40

4.3 Hardware properties 42
4.4 Selecting frequency ranges and removal of narrowband transmitters 44
4.5 Signal search window and noise windows 51
4.6 Simulation sets 57
4.7 Thunderstorms 57
4.8 Geomagnetic field 59

5 Analysis methods 61
5.1 Hilbert transformation and envelope 61
5.2 Stokes parameters 65
5.3 Calculating and testing uncertainties on parameters 66
5.4 Uncertainties on the Stokes parameters 70
5.5 Biases on the Stokes parameters 76
5.6 Derivatives of Stokes parameters 79

6 Emission mechanisms and their polarization 85
6.1 Polarization signature of geomagnetic radiation 86
6.2 Polarization signature of charge-excess radiation 91
6.3 Strength of the radial component 96
  6.3.1 Geometry and polarization angle 96
  6.3.2 Generating probability density functions 98
  6.3.3 The relative strength of the radial component in individual measurements 99
6.4 Dependencies on EAS parameters 104
  6.4.1 Simulations 110
6.5 One-to-one comparison to MGMR simulations 113

7 Discussion and Conclusion 119

A Validation of the estimation of the uncertainty on a 125

Summary 137

Samenvatting 141

Acknowledgements **145**

Curriculum Vitae **147**

List of publications **149**

Chapter 1

General Introduction

The Earth's atmosphere is continuously bombarded by sub-atomic particles that are called cosmic rays. In the beginning of the 20th century, it was found that electrometers were discharging by an unknown source of radiation. Theodor Wulf found that the amount of radiation decreases in caves, and that it is higher than expected on the top of the Eiffel Tower. Inspired by the results of Theodor Wulf and Albert Gockel, Victor Hess initiated balloon flights. They observed that the amount of radiation was increasing with altitude, and that therefore its origin must be extra terrestrial.

When the energy of a cosmic-ray particle is high enough, it can generate a cascade of secondary particles that can be detected at ground level. Such a cascade was discovered by Pierre Auger in 1939 [1], and is nowadays known as an Extensive Air Shower (EAS).

The energy of the cosmic rays spans many decades as shown in figure 1.1. Already in 1962, John Linsley measured an EAS with an energy above 10^{20} eV [2]. However, as can be deduced from figure 1.1, these EASs are very rare. To study such high energetic events, experiments with a large collection area are necessary. The Pierre Auger Observatory is the largest cosmic-ray detector in the world and is located near the town of Malargüe in Argentina. It is designed to address the following questions: Where do these ultra-high-energy cosmic rays originate from and what is their nature?

At the Pierre Auger Observatory several techniques are combined to measure EASs. An array of particle detectors, which covers an area of $3000\,\mathrm{km}^2$,

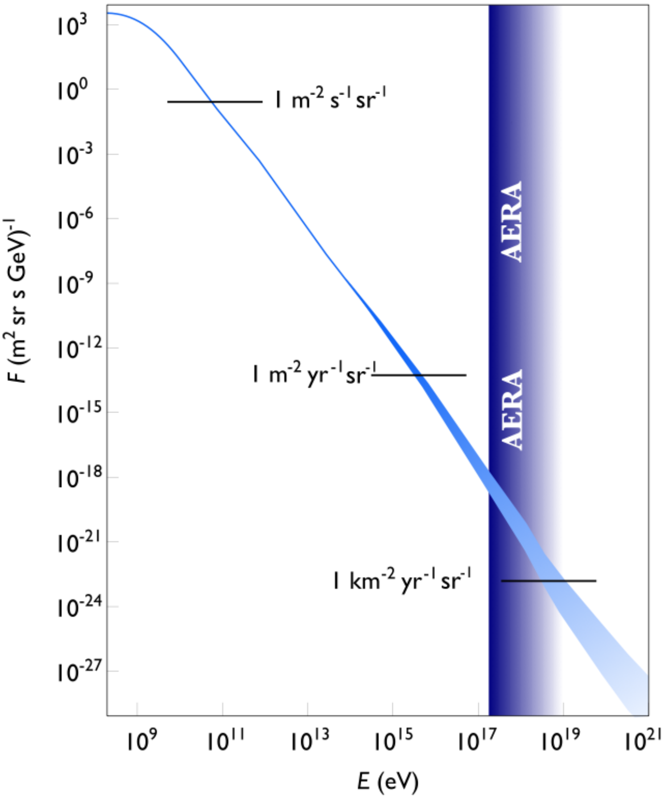

Figure 1.1: The energy spectrum of cosmic rays. The energy flux F of the cosmic-ray particles as a function of their energy E is shown. The dark blue band indicates the energy band for which the Auger Engineering Radio Array is designed (figure by S. Lafebre, modified to indicate the AERA band).

measures the footprint of the EAS on the ground. Telescopes detecting fluorescence light provide a measurement of the longitudinal development of the EAS, while it propagates through the atmosphere. The direction and the energy of the cosmic-ray particle are obtained from these measurements. The nature of the cosmic-ray particles is deduced by comparing measurements to interaction models. In addition to the mentioned detectors, several other techniques are being developed and calibrated at the observatory. One of them is using radio antennas, that are sensitive in the MHz domain. The analysis of measurements obtained with this technique is the topic of this thesis.

In 1962 Askaryan calculated that the build-up of a negative charge excess in the shower front can lead to coherent radiation [3]. The first observations of radio pulses associated with EASs were reported by Jelley *et al* in 1965 [4]. Subsequently several setups were deployed. With more measurements, it became urgent to model the emission mechanisms in more detail. Kahn and Lerche [5, 6] pointed out the importance of radiation from the deflection of charges in the geomagnetic field. An overview of the results from several experiments in the late sixties and early seventies is given by Allan [7]. He concluded that most of the measurements were supportive of a dominant geomagnetic emission mechanism.

In the last decade, the field has been revived by experiments like CODALEMA [1] and LOPES [2]. At the moment, an array of $20\,\mathrm{km}^2$ covered with antennas is being deployed at the Pierre Auger Observatory: the Auger Engineering Radio Array (AERA). It is designed to measure EASs with an energy above $10^{17}\,\mathrm{eV}$, as is indicated in figure 1.1.

The most important motivation for developing the radio detection technique is that the radio signal (may) carry information about the longitudinal shower development. The EAS development can in principle be used to deduce information about the nature of the cosmic-ray particle. The Pierre Auger Observatory provides an excellent location to cross-calibrate the radio signal with well established techniques. To use the radio signal

---

[1] `http://codalema.in2p3.fr/`

[2] `http://www.astro.ru.nl/lopes/`

to obtain information about the cosmic-ray particle, it is important to understand the emission mechanisms causing it.

The polarization of the radio signal, i.e. the orientation of the electric field, can be used to disentangle the emission mechanisms. In this thesis, the polarization of radio signals from EASs, measured at the Pierre Auger Observatory using several experimental setups, is analyzed. In chapter 2, individual emission processes are explained. Chapter 3 gives an overview of the Pierre Auger Observatory, and a description of the radio setups that are used in this thesis. In chapter 4, the data selected for analysis is described. In chapter 5, the tools necessary to analyze the polarization of a radio pulse are developed. These are applied in chapter 6, in which the polarization is used to identify and quantify the contributions of the emission mechanisms. The results from this polarization analysis are discussed in chapter 7.

Chapter 2

Theory

2.1 Radio emission from extensive air showers

To model emission from extensive air showers (EASs) in radio frequencies there are two approaches that one can choose. One could go for a microscopic description, in which single particles are followed and their individual radiation losses are calculated. On the other hand, one could go for a macroscopic view, in which the radiation is calculated from the (macroscopic) particle distributions in the EAS.

The microscopic approach is incorporated in models such as REAS3 [8], ReAires [9] and ZHAireS [10]. Whereas, a macroscopic approach is used in the MGMR [11] model. Despite the different nature of these approaches, the underlying physics is the same. Therefore, both methods should result in the same radio signature from EAS. Recently, it has been shown that both approaches indeed give comparable results [12].

In the following sections, a macroscopic approach based on the MGMR model [11, 13, 14] is used. The macroscopic approach has been chosen because it has the advantage that contributions from different physics processes to the total emitted radio emission are described separately.

The general idea of a macroscopic theory is to identify the macroscopic 4-current J^α, and calculate the Liénard-Wiechert [15] potential A^α from it. The 4-current is defined as $J^{\alpha} = (\rho c, \mathbf{j})$, in which ρ gives the charge density and $\mathbf{j}$ the current density. The Liènard-Wiechert potential can be calculated in terms of the 4-current

$$A^{\alpha} = \int_V \mathrm{d}V \left[\frac{J^{\alpha}}{(1 - n\boldsymbol{\beta}\cdot\hat{r})R}\right]_{\mathrm{ret}}, \tag{2.1}$$

with $\boldsymbol{\beta} = \boldsymbol{v}/c$ the velocity of the current, with n the refractive index of the medium, and with R the distance between the location of the current and the observer. Unit vector $\hat{\boldsymbol{r}}$ points from the location of the 4-current to the location of the observer. The subscript *ret* means that the potential needs to be evaluated at the retarded time. The integral is carried over the complete volume containing the 4-current.

From the four potential the electric field can be obtained by

$$\mathbf{E} = -\nabla A^0 - \frac{\partial}{\partial t}\mathbf{A}. \tag{2.2}$$

In the following sections, the dominant contributions to the total electric field are discussed.

2.2 Shower development and particle distribution functions

To understand the radio emission from EAS, it is crucial to understand the charge and current densities within the EAS. By far the most abundant charge carriers are electrons and positrons. Therefore, only their contributions to the radio emission are considered.

The parameterization of the charge and current densities presented in this section is based on the one given in [13]. Figure 2.1 shows the coordinate system that is chosen to describe the properties of the EAS. In the model an EAS propagating along the $\hat{z}$ axis is considered. The time coordinate t is chosen such that the shower front is arriving at $(x = 0, y = 0, z = 0)$ at time $t = 0$. At a given retarded time t_{r}, the shower front is at height $z_s = -\beta_s c t_{\mathrm{r}}$, with $\beta_s = v_s/c$ the velocity of the shower front. To describe the density above the shower front, a height h with respect to the shower front is introduced (figure 2.1).

The total number of electrons and positrons in the EAS, N, can be described using density functions

$$N = N(t, x, y, h) = N_{\mathrm{M}} f_l(t) f_{\mathrm{V}}(x, y, h), \tag{2.3}$$

with N_{M} the maximum number of electrons and positrons that occurs during the propagation through the atmosphere. The normalized density functions are shown in figure 2.1 and will be explained below.

The total number of electrons and positrons in the EAS at moment t is given by the longitudinal shower development $N = N_{\mathrm{M}} f_l(t)$. Usually, the longitudinal shower development is described as a function of the amount of atmosphere X (expressed in $\mathrm{g\,cm^{-2}}$) that is passed by the shower front [16]

$$f_l(t) = e^{\left(X(t) - X_M - 1.5X(t)\ln(s(t))\right)/X_0}, \tag{2.4}$$

in which X_{M} is the atmospheric depth at which N_{M} occurs, and X_0 gives the atmospheric depth of the first interaction on average. The function $s(t)$ is the shower age which is defined as

$$s(t) = \frac{3X(t)/X_0}{X(t)/X_0 + 2X_M/X_0}. \tag{2.5}$$

However, for modeling the radio emission it is beneficial to go for a geometric description. Assuming an atmospheric density function, X can be expressed as a function of shower height or time. In the MGMR model a simple atmospheric density function is chosen

$$X(t_s) = \frac{\rho_0}{C} e^{-Cz_s} = \frac{\rho_0}{C} e^{C\beta_{\mathrm{s}} c t_s} \tag{2.6}$$

in which ρ_0 is the atmospheric density at ground level and C is a constant to convert a density into an atmospheric depth.

Integrating the volume containing the whole shower at a given moment should result in $N(t_s)$, this implies the following normalization condition

$$\int_V f_V(x, y, h) dV = 1. \tag{2.7}$$

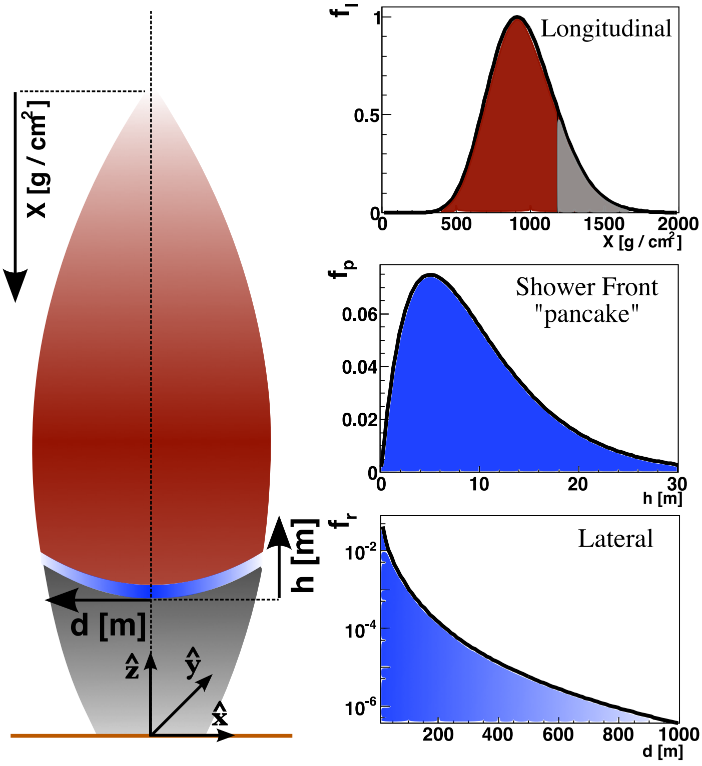

Figure 2.1: Coordinate system and normalized density functions. The origin of the coordinate system is at ground level. The $\hat{y}$ axis points to the geomagnetic north, the $\hat{x}$ axis is perpendicular to $\hat{y}$ and positive eastwards and the $\hat{z}$ axis is pointing upwards. The three normalized density functions on the right are discussed in the text.

In the MGMR model the density functions are separated into a radial (lateral), f_r, and a longitudinal shower front,f_p, component

$$f_V(x, y, h) = f_r(x, y)f_p(h) = f_r(d)f_p(h), \tag{2.8}$$

in which $d = \sqrt{x^2 + y^2}$ is the distance to the shower axis. The longitudinal shower-front profile, $f_p(h)$ is called the *pancake* function and in the MGMR-model its shape is parametrized with a Γ-distribution

$$f_p(h) = Ah^B e^{-hC} \approx \frac{4h^{\beta_s} e^{-2h/L}}{L^2}, \tag{2.9}$$

in which A is a normalization constant, B and C contain the information about the shape of the *pancake*. In the MGMR-simulations that are used in this thesis $L = 3.9\,\mathrm{m}$ and $\beta_s = 1$ are used.

The radial (lateral) extend of the EAS shower can be parametrized with the Nishimura-Kamata-Greisen (NKG) [17, 18] function

$$f_r(d) = \frac{2.5}{2\pi d_\mathrm{M}^2} \left(\frac{d}{d_\mathrm{M}}\right) \left(1 + \frac{d}{d_\mathrm{M}}\right)^{-3.5}, \tag{2.10}$$

in which d_M is the Molière radius and $d = \sqrt{x^2 + y^2}$ the distance to the shower axis. The Molière radius is a function of atmospheric density and is given by $d_\mathrm{M} = 9.6\,\mathrm{g\,cm^{-2}}/\rho_\mathrm{atm}(z)$ [19]. Equation (2.10) is normalized such that $2\pi \int_0^\infty d' f_r(d')\mathrm{d}d' = 1$.

To simplify calculations some approximations are made in the MGMR model. The first approximation is that the majority of charged particles are near the shower axis, and that therefore the radial extend of the shower can be neglected

$$\int_V f_p(h)\delta(d)\mathrm{d}V = \int_0^\infty f_p(h)\mathrm{d}h. \tag{2.11}$$

However, in recent work [14] it is argued that, especially for observers near the shower axis ($d < 200\,\mathrm{m}$), the radial extend should be taken into account. Another approximation is made for the typical length scale L of the pancake function. In the MGMR model it is taken to be constant, and therefore any dependency on the shower height is not taken into account. This value should describe the pancake distribution near the shower axis. However, this has not been measured. In this thesis simulations are used in which a value of $L = 3.9\,\mathrm{m}$ was adopted. However, recent Monte Carlo studies [14] indicate that this value should be significantly smaller ($L \approx 0.5\,\mathrm{m}$). Smaller values for L could lead to higher power at higher frequencies.

2.3 Geomagnetic mechanism

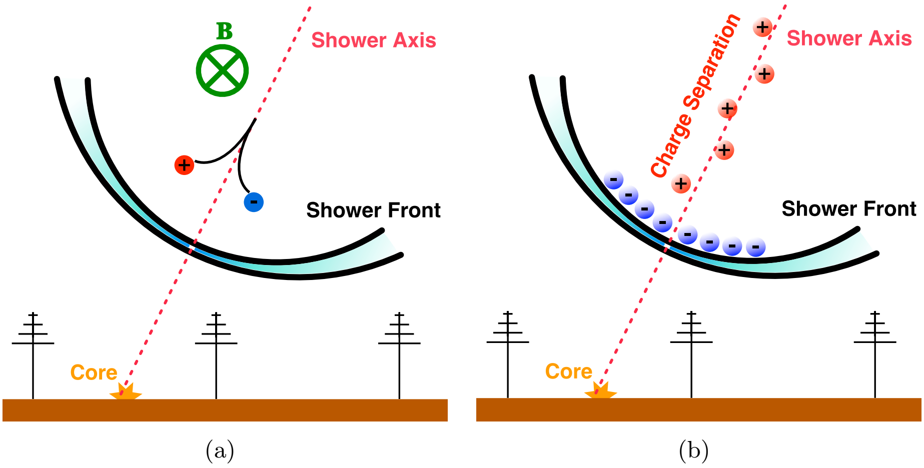

(a) (b)

Figure 2.2: Schematic overview of the geomagnetic (a) and charge-excess (b) emission mechanisms.

While traveling through the geomagnetic field in the atmosphere, trajectories of particles, with charge q, are bent under the influence of the Lorentz force

$$\mathbf{F}_\mathrm{l} = q(\mathbf{v}_\mathrm{s} \times \mathbf{B}). \tag{2.12}$$

This force is perpendicular to the geomagnetic field $\mathbf{B}$, and the direction of the propagation of the particles $\mathbf{v}_{\mathrm{s}}$. Therefore, its strength is equal to

$$F_{\mathrm{l}} = qv_sB\sin(\alpha), \tag{2.13}$$

with α the angle between $\mathbf{B}$ and $\mathbf{v}_s$. The electrons and positrons gain a velocity component, v_t, transverse to v_s. The angular deflection ψ, due to $\mathbf{F}_{\mathrm{l}}$, of the trajectory of an electron or positron with mass m_e is approximated by

$$\psi = \frac{L_f}{R_B} = \frac{qBL_f\sin\alpha}{m_e\beta_sc}, \tag{2.14}$$

in which R_B is the radius of curvature of the trajectory of an electron in magnetic field B with an energy $\epsilon = \gamma mc^2$. The length L_f gives the mean free path of an electron passing through air, which should depend on the air density ρ_{air} and the γ factor of the electrons. The average drift velocity of the electrons is approximated to be

$$<v_d>= \frac{c\psi}{2} = \frac{qBL_f(\gamma,\rho_{air})\sin\alpha}{2m_e\beta_sc}, \tag{2.15}$$

in which the factor 2 results from averaging over the whole trajectory. The direction of the drift velocity depends on the sign of q. Within the MGMR model the drift velocity is approximated by a constant value, deduced from Monte Carlo simulations. For simulations of EASs measured by the Pierre Auger Observatory a value of $<v_d>= 0.025c$ is adopted from [11].
In the coordinate system introduced in section 2.2, there will be a geomagnetic induced current in the $\hat{x}$ direction

$$J^x = - <v_d> eN(h,t), \tag{2.16}$$

in which e is the elementary charge, an electron has a charge of $q = -e$. The vector potential (equation (2.1)) can be written as

$$A^x(t_{\mathrm{obs}},d) = J_0 \int \frac{f_{\mathrm{l}}(t_r)f_p(h)}{D}dh, \tag{2.17}$$

in which $J_0 =< v_d > Ne/(4\pi\epsilon_0c)$, $D = R(1 - n\boldsymbol{\beta_s}\cdot\hat{\boldsymbol{r}})|_{\mathrm{ret}}$ the retarded distance and t_r the retarded time. Let us consider a photon that is emitted at a height $z = -c\beta_s t_r + h$, then the distance to an observer at $(x, y, z = 0)$ is given by

$$R = \sqrt{x^2 + y^2 + (-c\beta_s t_r + h)^2} = \sqrt{d^2 + (-c\beta_s t_r + h)^2}. \tag{2.18}$$

A photon emitted at time t_r would travel a time

$$\Delta t = (t_{\text{obs}} - t_r) = \frac{nR}{c} \tag{2.19}$$

before reaching the observer, where t_{obs} is the time at the observer. Solving this equation for ct_r results in

$$ct_r = \frac{ct_{\text{obs}} - n^2\beta_s h - n\sqrt{(-\beta_s ct_{\text{obs}} + h)^2 + (1 - n^2\beta_s^2)d^2}}{(1 - n^2\beta_s^2)}, \tag{2.20}$$

in which the sign of ct_r is chosen such that it will be negative for EAS above the ground. Using this expression for ct_r, the following expression for D is obtained

$$\begin{aligned} D &= R(1 - n\boldsymbol{\beta_s} \cdot \hat{\boldsymbol{r}})|_{\text{ret}} = \frac{ct_{\text{obs}} - ct_r}{n} - n\beta_s h + nc\beta_s^2 t_r \\ &= \sqrt{(-c\beta_s t_{\text{obs}} + h)^2 + (1 - n^2\beta_s^2)d^2}. \end{aligned} \tag{2.21}$$

By taking the time derivative of the vector potential the electric field is obtained

$$\begin{aligned} E^x(t_{obs}, d) = & - J_0 \int_{t_r^-(t)}^{t_r^+(t)} \mathrm{d}t_r f_1(t_r) \frac{\beta_s}{z_s} \frac{\mathrm{d}f_p(h)}{\mathrm{d}h} \\ & - J_0 \int_{t_r^-(t)}^{t_r^+(t)} \mathrm{d}t_r \frac{\mathrm{d}f_1(t_r)}{\mathrm{d}t_r} \frac{f_p(h)}{z_s} \end{aligned} \tag{2.22}$$

with $t_r^- = -\infty$ and $t_r^+(t_{\text{obs}}) = t_r(t_{\text{obs}}, h = 0)$. In equation (2.22) the dependency on t_{obs} and d are obtained using equation (2.20).

Note that the electric field in equation (2.22) only has a component in direction of the Lorentz force. Therefore, the electric field orientation does not depend on the location of the observer, but only on the direction in which the EAS propagates.

2.4 Charge-excess mechanism

While propagating through the atmosphere a negative charge excess will build up in the shower front as shown in figure 2.2. There are two effects contributing to this excess: Electrons are knocked out the atmospheric molecules due to interaction with particles from the air shower. They obtain relativistic velocities and travel with the air shower towards the ground. Therefore, they can be considered as part of the air shower. The other contribution is due to the annihilation of positrons in the shower front. The build up of this charge excess can result in coherent radiation as was pointed out by Askaryan [3].
This charge excess leads to two contributions in the zeroth component of the vector potential. The contribution caused by the excess of electrons in the shower front is

$$A^0_{\mathrm{e}} = \frac{-eN_{\mathrm{M}}C_x}{4\pi\epsilon_0}\int_0^\infty \mathrm{d}h\frac{f_{\mathrm{l}}(t_r)f_p(h)}{D} \tag{2.23}$$

in which C_x is the fraction of particles that contributes to the charge excess with respect to the total number of positron and electrons. For the MGMR simulations used in this thesis, this fraction is approximated to be independent of shower height, and a value of $C_x = 0.23$ is adopted from Monte Carlo simulations. In reality this fraction varies with altitude.
The EAS leaves behind a positive trail of ions which contributes to the vector potential. The charge left behind by the shower front at a retarded time t'_r is

$$eN_{\mathrm{M}}\int_0^\infty \mathrm{d}hf_p(h)\frac{\partial f_l(t'_r)}{\partial t'_r}. \tag{2.24}$$

The contribution to the potential becomes

$$A^0_{\mathrm{ions}} = \frac{-eN_{\mathrm{M}}C_x}{4\pi\epsilon_0}\int_{-\infty}^{t_{\mathrm{r}}}\left(\int_0^\infty \frac{\partial f_l(t'_r)}{\partial t'_r}\frac{f_p(h)}{R}\mathrm{d}h\right)\mathrm{d}t'_r, \tag{2.25}$$

in which the total positive ion tail is taken into account by integrating over the history of the shower development. The assumption is made that the speed of the ions is much smaller than the speed of light, which results in

$$D = R(1 - \boldsymbol{\beta} \cdot \hat{\boldsymbol{r}})|_{\mathrm{ret}} = R - \beta_{\mathrm{ions}} z \approx R, \tag{2.26}$$

in which R is the distance between the emission point and the observer. Taking the spatial derivative to x of equation (2.23) results in

$$E_{x,\mathrm{e}} = -\frac{\partial A^0_{\mathrm{e}}}{\partial x} = \int_0^\infty \mathrm{d}h f_p(h) \left(\frac{1}{D} \frac{\partial f_l}{\partial ct_r} \frac{\partial ct_r}{\partial x} + f_l \frac{\partial}{\partial x} \frac{1}{D} \right). \tag{2.27}$$

Using the assumption $\beta_s = 1$ and $n = 1$ this reduces to

$$E_{x,\mathrm{e}} = \frac{-eN_{\mathrm{M}} C_x}{4\pi\epsilon_0} \int_0^\infty \mathrm{d}h f_p(h) \frac{x}{D^2} \dot{f}_l(t_r), \tag{2.28}$$

in which is used that $\partial ct_r / \partial x = -x/D$. The main contribution to the electric field induced by the ions results from the spatial derivative acting on the upper limit of the integral,

$$E_{x,\mathrm{ions}} = -\frac{\partial A^0_{\mathrm{ions}}}{\partial x} = \frac{eN_{\mathrm{M}} C_x}{4\pi\epsilon_0} \int_0^\infty \frac{x}{D} \dot{f}_l(t_r) \frac{f_p(h)}{R} + \mathcal{O}\left(\frac{x}{R^2}\right). \tag{2.29}$$

The induced static field that scales as $\frac{x}{R^2}$ is neglected. Combining equation (2.28) and (2.29) results in the total field in the x-direction

$$E_x(t_{\mathrm{obs}}, x) = \frac{-eN_{\mathrm{M}} C_x}{4\pi\epsilon_0} \left(\int_0^\infty dh \frac{x z_s}{R D^2} \dot{f}_{\mathrm{l}}(t_r) f_p(h) \right), \tag{2.30}$$

in which it is used that $R - D = z_s$ when $\beta_s = 1$. The derivation of E_y is similar and it is given by

$$E_y(t_{\mathrm{obs}}, y) = \frac{-eN_{\mathrm{M}} C_x}{4\pi\epsilon_0} \left(\int_0^\infty dh \frac{y z_s}{R D^2} \dot{f}_{\mathrm{l}}(t_r) f_p(h) \right). \tag{2.31}$$

The z-component has two contributions to the electric field. The zeroth component of the vector potential contributes similar like the x and y component

$$\frac{\partial A^0}{\partial z} = \frac{-eN_{\mathrm{M}} C_x}{4\pi\epsilon_0} \int_0^\infty dh \dot{f}_{\mathrm{l}}(t_r) f_p(h) \left(\frac{z}{D^2} - \frac{z}{RD} \right). \tag{2.32}$$

in which it is used that $\partial ct_r/\partial z = -\partial ct_r/\partial h = z/D$. The z-component of the vector potential contributes as:

$$\frac{\partial A^z}{\partial ct_{\rm obs}} = \frac{-eN_{\rm M}C_x}{4\pi\epsilon_0}\int_0^\infty dh\left(\frac{R}{D^2}\dot{f}_1(t_r)f_p(h)\right). \qquad (2.33)$$

in which it is used that $\partial ct_r/\partial ct_{\rm obs} = R/D$. The $z-$component of the electric field is then obtained by combining equation (2.32) and (2.33)

$$\begin{aligned}
E_z(t_{\rm obs},d) &= -\frac{\partial A^0}{\partial z} - \frac{\partial A^z}{\partial ct} \\
&= \frac{-eN_{\rm M}C_x}{4\pi\epsilon_0}\int_0^\infty dh\dot{f}_1(t_r)f_p(h)\left(\frac{z}{D^2} - \frac{z}{RD} - \frac{R}{D^2}\right) \\
&= \frac{-eN_{\rm M}C_x}{4\pi\epsilon_0}\int_0^\infty dh\frac{\dot{f}_1(t_r)f_p(h)}{RD^2}\left(zR - zD - R^2\right) \\
&= \frac{-eN_{\rm M}C_x}{4\pi\epsilon_0}\int_0^\infty dh\frac{\dot{f}_1(t_r)f_p(h)}{RD^2}\left(zR - z(R-z) - (d^2+z^2)\right) \\
&= \frac{-eN_{\rm M}C_x}{4\pi\epsilon_0}\int_0^\infty dh\frac{\dot{f}_1(t_r)f_p(h)d^2}{RD^2} \qquad (2.34)
\end{aligned}$$

The orientation of the electric field perpendicular to the shower axis is in the direction of the shower axis. This is expected for a negative charge which is mainly located near the shower axis. This means that, unlike the geomagnetic emission, the orientation of the electric field of the charge-excess contribution depends on the position of the observer.

2.5 Cherenkov effect

Recently the MGMR model [14] incorporated a realistic refractive index ($n = n(z) \neq 1$), which results in a boost of the charge-excess and geomagnetic contribution at distances near the shower axis. The reason for this is that the vector potential gains a singularity when $D = 0$ (equation (2.21)), which corresponds to Cherenkov emission.

If the electron densities are approximated with a point-like distribution

$$\int_V f_V(h,x,y)dV = \int_V \delta(h)\delta(x)\delta(y)dV, \tag{2.35}$$

then time when this singularity occurs is derived from equation (2.21),

$$ct_{\mathrm{c,obs}} = d\sqrt{1-n^2\beta_s^2}. \tag{2.36}$$

At this critical time the contribution of Cherenkov radiation is seen by the observer. Transforming this Cherenkov time to the retarded emission time $t_{r,\mathrm{c}} = t_{\mathrm{c,obs}}/(n^2-1)$ gives us the opportunity to convert it to a Cherenkov height

$$z_c = -ct_{r,\mathrm{c}}. \tag{2.37}$$

This height corresponds with a distance, d_{c}, from the shower axis were this Cherenkov contribution is seen

$$d_c = z_c\sqrt{n^2\beta - 1}. \tag{2.38}$$

For a vertical shower where N_M occurs at 4 km height this distance would correspond to $d_c \approx 100\,\mathrm{m}$ if $n = 1.0003$, as it is for standard temperature and pressure.

In the MGMR simulations used in this thesis the refractive index was chosen to be unity, and therefore no Cherenkov effects are taken into account. This might have consequences for the comparison of measurements with simulations, as will be discussed in Chapter 7.

2.6 Interference and polarization.

In figure 2.3 an example is shown for the electric field components of the geomagnetic and the charge-excess contributions. These pulses are generated from the MGMR model, as explained in the previous sections. Figure 2.3 shows a destructive interference between the contributions. This interference depends on the location of the observer, since this determines the orientation of the electric field of the charge-excess contribution. The

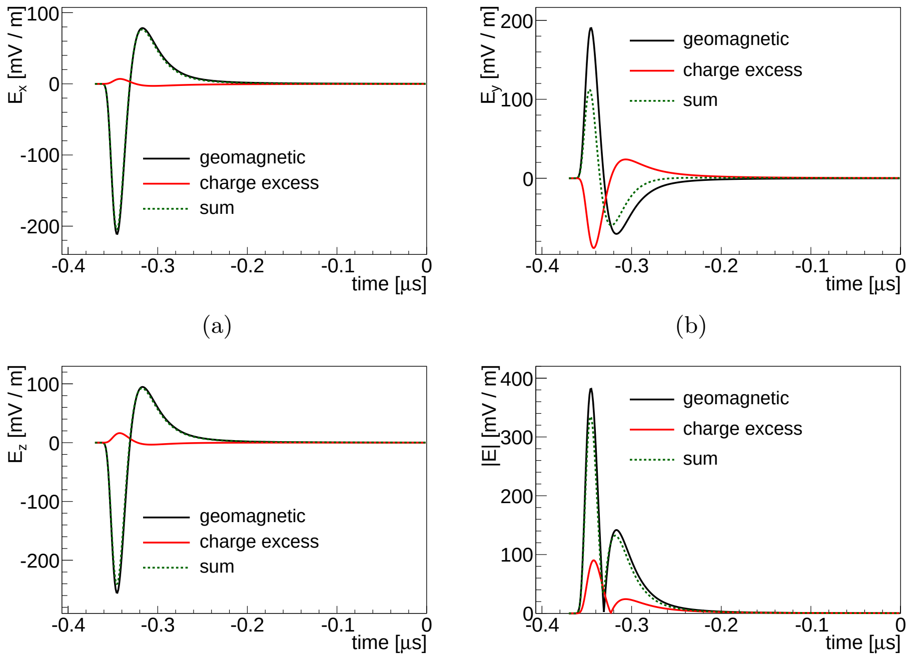

(a) (b)

(c) (d)

Figure 2.3: An example of the individual electric fields from the charge-excess and geomagnetic contribution and their sum. Figures (a), (b), and (c) show the individual components. Figure (d) shows the magnitude of the electric field. Note that in figure (a) and (c) the lines of geomagnetic and the sum are on top of each other.

orientation of the electric field from the geomagnetic contribution does not depend on the location of the observer.
The electric field presented in 2.3 is not bandpass limited. However, radio detectors are only sensitive in a limited frequency band (chapter 3). Therefore, an example of a bandpass filtered pulse is shown in figure 2.4.

The individual emission mechanisms described in the previous sections lead to a single polarized pulse. With this we mean that the orientation

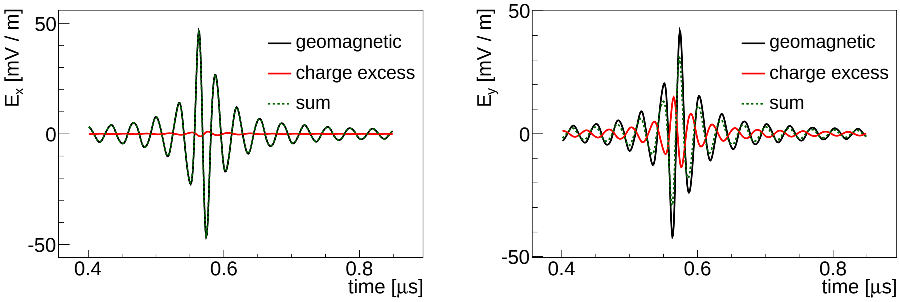

(a)

(b)

Figure 2.4: An example of the individual bandpassed electric fields from the charge-excess and geomagnetic contribution and their sum. In (a) the x component is shown, while (b) shows the y component. The pulses are filtered by a rectangular bandpass filter between 30-80 MHz. Note that in figure (a) the lines of geomagnetic and the sum are on top of each other.

of the electric field at a given location has one defined direction for the duration of the pulse. Such a pulse we will refer to as being completely linearly polarized. However, by adding the electric fields from two or more emission mechanisms, linearity can only be conserved if the time structure of the pulses are identical for each individual contribution or when the orientations of the electric fields are equal. For example, if we have two (linear) emission mechanisms with electric fields $\mathbf{E}_A(t, \mathbf{x})$ and $\mathbf{E}_B(t, \mathbf{x})$, then linearity of the combined electric field is conserved if

$$\mathbf{E}(t, \mathbf{x}) = \mathbf{E}_A(t, \mathbf{x}) + \mathbf{E}_B(t, \mathbf{x}) = (l_A(\mathbf{x}) + l_B(\mathbf{x}))\mathbf{g}(t). \tag{2.39}$$

The example in figure 2.5 shows the effect on the polarization when the charge-excess and geomagnetic contributions are added. This example only shows the effects on the horizontal (x, y) components of the electric field, this is chosen because in later chapters these are the components that are measured and are used in analyses.

The example in figure 2.5 shows that the orientation of the electric field changes if the charge-excess contribution is added to the geomagnetic con-

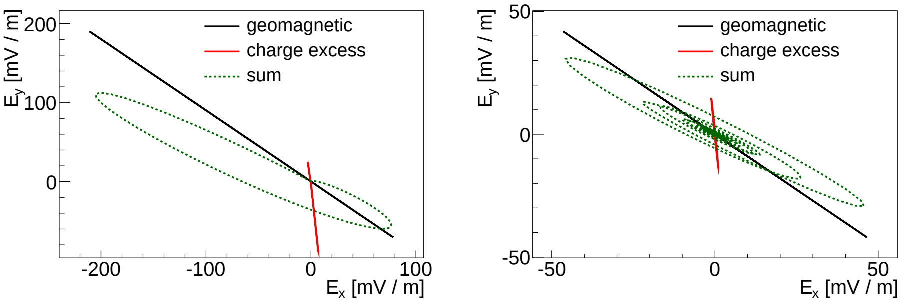

(a)

(b)

Figure 2.5: Example of the polarization of the horizontal electric field. The full electric field is shown in (a) (same pulses as figures 2.3(a) & (b)), while (b) shows the bandpass limited polarization (same pulses as figures 2.4(a) & (b).

tribution. This change in orientation will be the basis for the analysis presented in Chapter 6, where it will be used to disentangle the charge-excess and the geomagnetic contributions.

Next to the change in orientation, the total electric field gains a circular component. This circular component contains information about the difference in pulse shape of individual contributions. Measuring a circular polarization is already an indication that more than one contribution is responsible for the radio signal. However, the pulse shape strongly depends on the particle distributions near the shower axis, which are not well known at the energies we are interested in. Therefore, interpretation of the circularity is very model dependent and will not be considered futher in this thesis.

The interference of multiple contributions, and the Cherenkov effect, leads to a complex signal pattern at the surface of the Earth. Therefore, a simple one dimensional, strictly decreasing, lateral distribution function will not describe the measured distribution of signal amplitudes. To constrain a lateral distribution fit to the radio signals, events should be measured with stations at many different positions. This has implications on the required density of stations in a stand-alone RD cosmic ray detector.

On the other hand, since the radio signal shape depends mainly on the electron-positron distributions near the shower axis, measuring radio signals may probe EAS physics that is out of reach for standard particle detectors, such as the surface detector and the fluorescence detectors of the Pierre Auger Observatory.

Chapter 3

Detectors

The data used in this thesis is recorded using several types of detectors, which will be described in this chapter. Section 3.1 gives an overview of the Pierre Auger Observatory. In the following section, an overview of the individual radio detectors used for this thesis is given. In section 3.3 the method for calibrating the radio signal is presented.

3.1 The Pierre Auger Observatory

The southern site of the Pierre Auger Observatory is located on the Pampa Amarilla, near the town of Malargüe in the province of Mendoza, Argentina. It is a hybrid observatory in which a so-called surface detector (SD) [20] and a fluorescence detector (FD) [21] are combined. It is designed to measure extensive air showers (EASs) which have an energy above 10^{18} eV. A site overview is shown in figure 3.1.

The SD is an array of more than 1600 water tanks, each equipped with three photomultiplier tubes (PMTs). An example of one of the water tanks is shown in figure 3.2. When charged particles from the EAS pass through the water, they emit Cherenkov light. This light is reflected from the walls of the tank and recorded by the PMTs installed at the top of the tank. The water tanks are placed on a regular triangular grid and are separated by

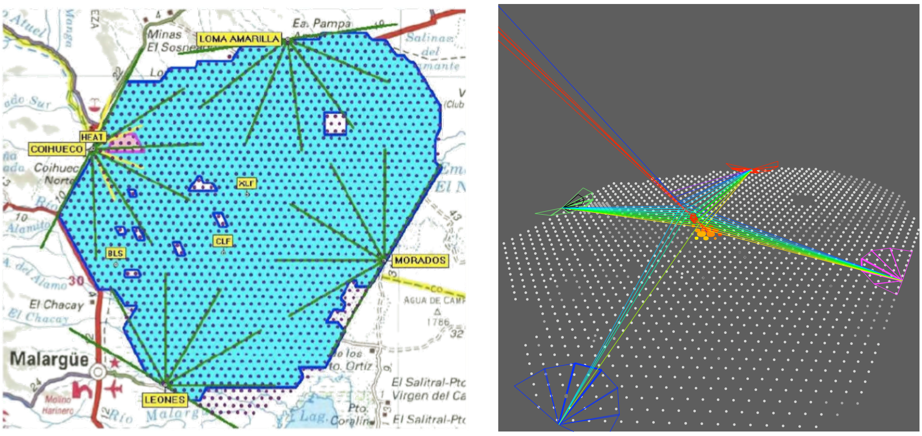

(a) (b)

Figure 3.1: The layout of the Pierre Auger Observatory is shown in (a). The blue region indicates the area covered by the SD. At the edge of the SD, the locations and the names of the four FD buildings (called *eyes*) are shown. The green lines indicate the field of view of the six telescopes within an *eye*. The pink area in the north-west of the array is the location of AERA. The label BLS in the mid-west of the array, gives the location of the balloon launching station. In (b) an EAS reconstructed by the SD and all four FD *eyes* is shown. The color coding gives the arrival time of the signals, from blue to red for the FD, and from yellow to red for the SD. The size of the circles indicates the signal strength recorded by the SD tanks.

1500 m. In total the SD covers an area of about 3000 km^2.

By using the arrival times of the recorded signals, the direction of the primary cosmic ray is reconstructed. Using the signal strength recorded in the tanks, the footprint of the EAS at ground level is reconstructed. The reconstructed footprint provides a measure of the energy of the primary cosmic ray.

The FD is placed on the periphery of the SD, and consists of 24 fluores-

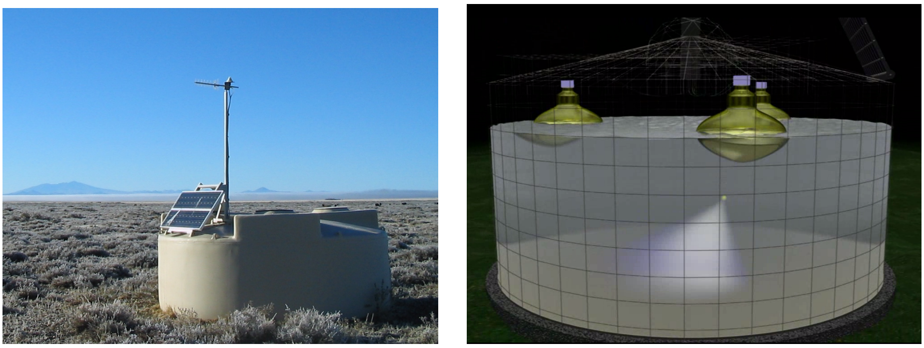

(a)

(b)

Figure 3.2: One of the water tanks of the SD in the field is shown in (a). The power is obtained using solar panels and the communication to the central DAQ is performed with a wireless network. In (b) an artists impression of a charged particle emitting Cherenkov light in the water is shown. The light is reflected from the walls and recorded with the three PMTs at the top.

cence telescopes located in four buildings. Such an FD building is called an *eye*. One of the *eyes* and a fluorescence telescope are shown in figure 3.3. The telescopes record ultraviolet fluorescence light emitted by atmospheric nitrogen molecules. These molecules are excited due to interactions with charged particles in the EAS. This light is very faint. Therefore, the FD is very sensitive and can only be operated during cloudless and moonless nights. This results in a duty cycle of about 15%.

The amount of emitted fluorescence light is proportional to the number of charged particles in the EAS. Therefore, the intensity of the track of fluorescence light gives a direct measure of the longitudinal shower development. This longitudinal shower development depends on the composition of the primary cosmic-ray particles. The energy of the primary cosmic-ray particle is proportional the total emitted fluorescence light. From the arrival time of the signal, the direction of the EAS is reconstructed.

Using hybrid events, like the one in figure 3.1(b), EAS properties that can


(a) (b)

Figure 3.3: A picture of the most southern FD *eye* Los Leones is shown in (a). The white doors function as the shutters of the telescopes. On the tower, behind the building, network antennas are attached to provide the network link to the central campus building in Malargüe. In (a) a picture of an FD telescope is shown. The mirror collects the fluorescence light and focusses it on an array of PMTs. Just after the shutter, a filter blocks all light outside the UV band and a corrector ring reduces the effect of spherical aberration.

be reconstructed by both techniques are cross-calibrated. This reduces the dependency on monte carlo simulations in the interpretation of the data. Furthermore, by using measurements from both detectors, the models that are fit to the data are better constrained. An example of this hybrid reconstruction is the shower axis reconstruction using the FD. While the direction can be reconstructed from the timing, the distance to the shower axis cannot be resolved if the event was measured by only one FD *eye*. Using the SD measurement, the shower axis is located.

Several enhancements are being deployed at the Observatory. Established techniques are used to lower the energy threshold of the observatory, or

new techniques are investigated and calibrated.
In addition to the regular FD, three additional fluorescence telescopes are deployed: the high elevation auger telescopes (HEAT). These telescopes are tilted to extend the field of view to angles of higher elevation. As the energy of the EAS becomes lower, the shower develops higher in the atmosphere. Therefore, HEAT extends the measurements of longitudinal shower development to lower energies.
In the area overlooked by HEAT and the FD-*eye* Coihueco, a higher density array of particle detectors is deployed, the Auger Muons and Infill for the Ground Array (AMIGA). It consists of 42 additional regular SD tanks placed on a grid with smaller spacings than the regular SD array. Each tank will be associated with $10\,\mathrm{m}^2$ of scintillators buried under several meters of soil. These scintillators will measure the muon component of the EASs. Measuring the muon component, in addition to the electron component, will tell us more about the composition of the primary cosmic-ray particle.
In addition to the well established techniques, new detection methods are being tested. Especially, detecting emission from EASs at radio frequencies gets a lot of attention. There are two categories, separated by their frequency bands: the MHz and the GHz-domain. In the lab GHz radiation has been measured from plasma clouds [22], which encouraged several initiatives [23] at the Pierre Auger Observatory.
In the MHz domain several prototypes have been operated. The detectors that delivered data for this thesis will be discussed in the following section. Other setups that are operated can be found for example in [23] (EASIER) and in [24] (RAuger).

3.2 Radio detectors

The data used in this thesis are obtained with three different setups. Before describing the individual setups in detail, the general concept of a radio detector (RD) is described. An RD is an array of radio detector stations (RDS). A schematic sketch of a general RD is shown in figure 3.4. Each

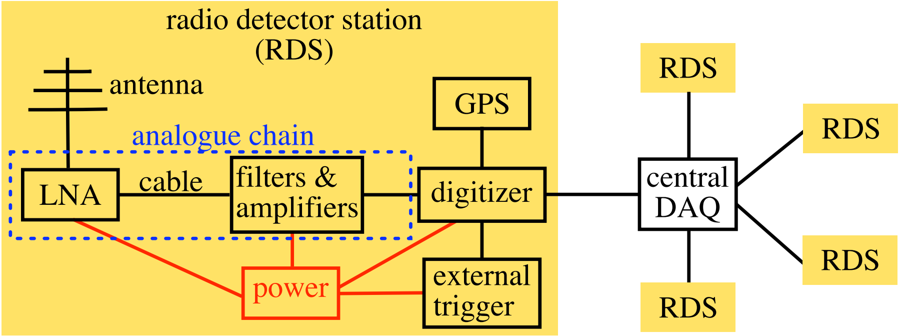

Figure 3.4: The general concept of a radio detector. The individual components of one analogue chain are drawn. See text for a more detailed description.

RDS has an antenna that is sensitive in the MHz domain. In this thesis only data measured with several types of dual-polarized log-periodic dipole antennas (LPDAs) were used. The frequency band in which they are sensitive is about 30-80 MHz. These antennas have two perpendicular arms, providing measurements of the electric field in the horizontal plane. The signal outputs of both arms are amplified at the foot of the antenna with a low-noise amplifier (LNA). Before being digitized, the signal passes through a series of cables, filters, and amplifiers. The filtering is performed to reduce the influence of unwanted background like narrowband transmitters from radio stations in the FM band. Amplification is needed to get the signal at the proper level before digitization. The signal chain from the foot of the antenna to the input of the digitizer we will call the analogue chain.
The digitizer converts the analogue signal into a digital signal using an analog-to-digital converter (ADC). The digitized data can be analyzed, in realtime, by a field-programmable gate array (FPGA) and/or a regular central processor unit (CPU). Furthermore, the digitizer has a local memory buffer in which the data can be stored. An absolute time stamp can be assigned to the data by the use of a global positioning system (GPS).

The RDS might have the possibility for an external trigger. If the trigger decision is made using the FPGA, it is called a level-1 trigger. After passing the level-1 trigger, the data might be further analyzed using the CPU, which is the level-2 trigger. Passing both trigger levels, the full data is stored in local memory and its time stamp is sent to the central data acquisition (DAQ). At the central DAQ a level-3 trigger decision is made based on the time stamps of several RDSs. If the event passes the level-3 trigger, the full data is collected from the RDSs and written to disk.

3.2.1 First prototype at the Balloon Launching Station (BLS 2007 / 2008)

A first prototype RD was installed in 2007, which was an array of three antennas. An overview of this RD is shown in figure 3.5. It was located in the middle-west of the SD array, next to the balloon launching station (BLS). At the BLS, weather balloons were launched and tracked to monitor atmospheric conditions.

This prototype RD was used to test hardware configurations. Several types of antennas have been mounted. However, in this thesis only data is used that was obtained with dual-polarized aluminum log-periodic-dipole antennas (ALPDAs) [25]. These antennas were mounted at P1 and P2, while at P3 most of the time other antennas were mounted. The arms have been aligned such that one arm is roughly aligned with north-south, and the other arm with east-west. The accuracy of this alignment was never measured (or documented) and therefore the exact alignment is unknown. After amplification by the LNA, the signal is transported to the BLS over a 160 m long coax cable. This cable length was the same for each antenna. Therefore, the time delay introduced by the cable (about 850 ns) is identical for each antenna. In the BLS, the signal was amplified and filtered by commercially available electronics purchased from MiniCircuits[1]. Several filter combinations were tested. However, in this thesis only data are used

---

[1] `www.minicircuits.com`

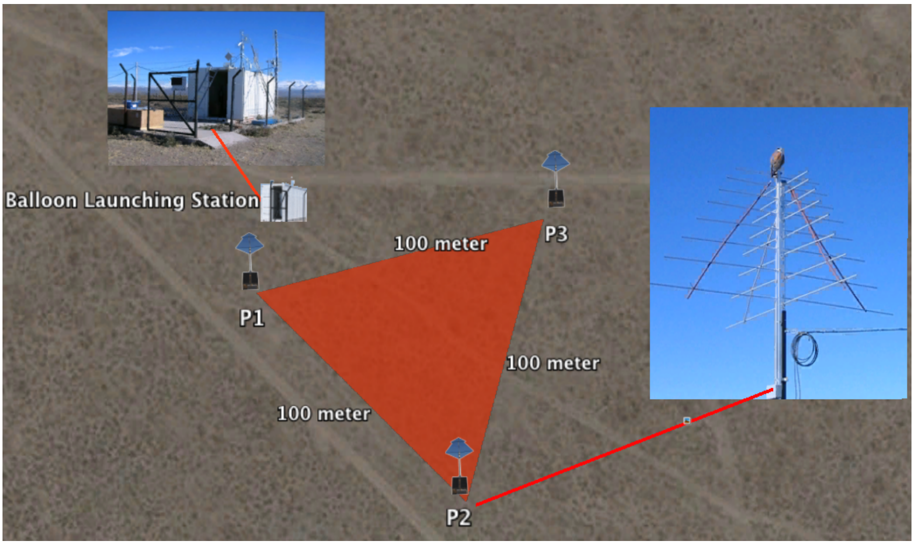

Figure 3.5: Radio detector layout of the first prototype at the BLS. At the location P1, P2 and P3 antennas were mounted. A picture of an aluminum LPDA and of the balloon launching station are shown as insets. The scintillators are placed on both sides of the balloon launching station, one is of them is visible (blue box on right of the BLS).

that were taken with either a series of high pass (SHP-25+) and low pass (SLP-70-) filters, or with bandpass (SBP60+) filters. The digitization was performed by digitizers that sample the signal with a frequency of 400 MHz. The readout of the antennas was triggered by an external particle detector. This particle detector consisted of two scintillator plates with a collection area of about $0.5\,\mathrm{m}^2$ each. The plates were separated by $\sim 6\,\mathrm{m}$. When in both plates a signal was recorded simultaneously, a trigger signal was sent, and the digitizers were read out.
In the vicinity of the BLS an additional SD tank, called *Olaia* (figure 3.6), was deployed in order to locally lower the energy threshold of the SD. The

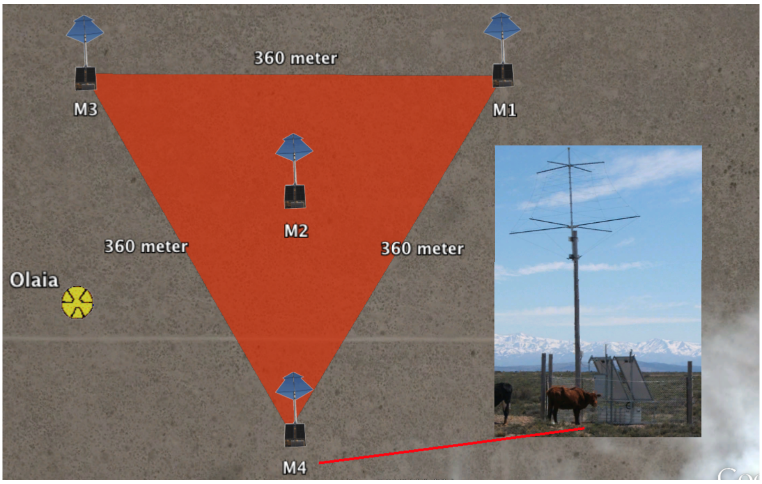

Figure 3.6: The MAXIMA setup. The four RDSs are located at M1, M2, M3, and M4. Also the additional SD tank *Olaia* is shown. A picture of an RDS accompanied by some cows is added.

timing of the radio and the SD data were compared offline. In May 2007 this resulted in the first radio signals from EAS measured at the Pierre Auger Observatory [26, 27].

In this configuration the setup ran from May 2007 until May 2008 and in total it was read out 495 times in time coincidence with the SD (see section 4.2). A detailed description of data taking and analyses with this setup is given in [28, 29, 30].

3.2.2 Multiple Antenna eXperiment In Malargüe Argentina (MAXIMA)

In order to cover large areas with RDSs, they should be able to function autonomously. To develop such a system, a next generation prototype RD was deployed called Multiple Antenna eXperiment In Malargüe Argentina (MAXIMA). This is an array of four identical RDSs and is located a few hundred meters to the east of the first prototype. A site overview is shown in figure 3.6.

The antenna of the RDS is a dual-polarized wire-LPDA, called the *black spider*. The initial mounting was with one arm roughly parallel to north-south and the other parallel to east-west. However, by studying the polarization of the radio signal it became obvious that an accurate antenna alignment is crucial. Therefore, the antennas have been realigned, with one arm parallel to geomagnetic north, and the other perpendicular to this [31].

The electronics of the RDS are placed in a metal box, which shields the antenna from noise induced by the electronics. The digitizer has four input channels and samples the signal at 200 MHz. The signal chain connected to the east-west arm of the *black spider* is split into two. The filters installed in the analogue chains are listed in table 3.1.

Channel	Source	Filters
1	LPDA NS	2×(SHP-25+) + 2×(SLP-70+)
2	LPDA EW	2×(SHP-25+) + 2×(SLP-70+)
3	LPDA EW	no filters
4	Scintillator	different BP filters

Table 3.1: MAXIMA RDS channel layout. Filter types refer to the Mini-Circuits catalogue.

The first two channels contain the broadband physics channels, while in channel 3 no filtering is applied. The fourth channel is connected to a small scintillator, which gives the possibility to make a level-1 trigger decision on a particle detector. The scintillator plate is rather small, it has an area 12 cm×18 cm.

To provide each RDS with power, two solar panels are installed. When the power consumed by the RDS is lower than provided by the solar panels, the remainder is stored using four batteries placed in another metal box. When the solar panels cannot provide enough power directly, the station is powered from these batteries.

The communication between the RDSs and the central DAQ in the BLS was initially performed by a wireless network. However, this wireless network had severe problems with stability, which made stable running impossible. On top of that, it turned out that the electronics of the wireless network were generating a lot of noise, which was picked up by the *black spiders*. Therefore, it was decided to replace the wireless network with an optical fiber.

The FPGA in the digitizer runs a level-1 trigger algorithm in realtime. If the data passes the level-1 trigger, the time stamp is sent over the network to the central DAQ in the BLS. In the central DAQ a level-3 trigger algorithm checks for time coincidences between several RDSs. If two, or more, stations have a level-1 trigger in time coincidence, a request is sent to the RDSs to send the full readout of all channels to the central DAQ. In the central DAQ, the data from the individual RDSs are bundled in an event structure and written to disk. The data set that has been used in this thesis is taken with a level-1 trigger decision on the scintillator channel.

In this configuration MAXIMA started data taking in May 2010. It ran until September 2010, at that moment the digitizers were moved to AERA (see next section). This data set is described in [31]. In March 2011 new digitizers were installed, and the layout in the metal housing was slightly altered. Therefore, the data set of the MAXIMA setup is split in two sets that are dealt with separately (see chapter 4).

3.2.3 Auger Engineering Radio Array (AERA)

Groups from France, Germany and the Netherlands joined their effort to build the Auger Engineering Radio Array (AERA), which will be an RD that covers roughly 20 km^2 with RDSs. In September 2010, the first stage of AERA was deployed. In the coming years the array will be expanded to full size in two subsequent stages. The site overview is given in figure 3.7, which shows the co-location with the AMIGA detector, and the vicinity of FD *eye Coihueco* and HEAT.

Like the MAXIMA setup, AERA is designed such that the RDSs can

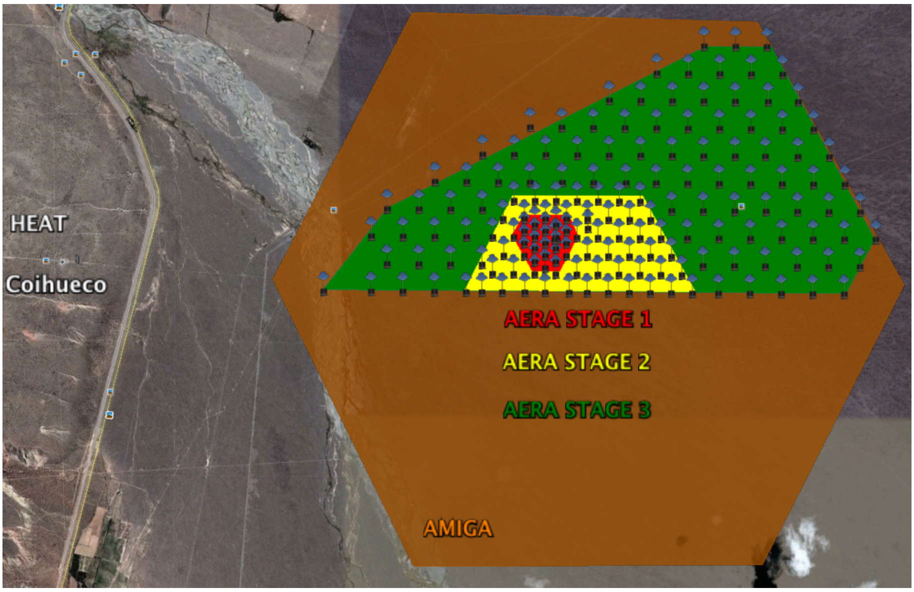

Figure 3.7: Overview of the AERA site. The different stages are indicated, stage 1 is currently running. In the coming years stage 2 and 3 will be deployed. The figure also shows the area of AMIGA, and the location of FD *eye Coihueco* and HEAT (on the left).

function autonomously. The central DAQ is in the Central Radio Station (CRS), which is a 40 ft shipping container. An array of solar panels provides its power. Therefore, it does not dependent on the regular power grid.

Stage one of AERA consists out of 21 radio detector stations placed in a regular grid with a spacing of 150 m. The RDSs and the CRS communicate over an optical fiber network. In the following stages an optical fiber is no longer feasible. Therefore, tests with wireless networks are ongoing.

The individual RDSs are equipped with a dual-polarized Wire-LPDA called the *small black spider*. The digitizers are the same as in MAXIMA. The filter-amplifier chain contains a custom made 30-80 MHz bandpass filter. The signal chains are split in a high gain and a low gain channel. The housing of the electronics and storage of the batteries is done in one metal box, and the number of batteries is reduced to two. Since the stations are not equipped with their own particle detector, they have to trigger on the radio signal itself.

Although the AERA site is remote, there is still a lot of human interference in the 30-80 MHz bandwidth. One type of interference is due to narrow-band transmitters, which can be suppressed digitally in real time. This allows using a lower signal threshold to trigger on air showers. Another type of noise sources are short pulses, which mimic a real signal coming from an EAS. The rate of these pulses is so high, that it becomes hard to process them all. Luckily they have some distinct features that are used to discriminate them from cosmic rays. Most of these pulses originate from certain directions on the horizon, which allows for a directional veto at the level-3 trigger.

After implementing and applying these vetoes, the recorded events are compared offline with events recorded by the SD. In the beginning of April 2011 this resulted in the first self-triggered events from AERA that were confirmed by a coinciding SD event. Soon thereafter, the first coincidence between AERA, SD, and FD was measured. This proved the feasibility of super-hybrid measurements of cosmic rays.

In figure 3.8 the first confirmed radio signal from an EAS measured by AERA is shown together with a view of an event measured in 8 RDSs.

3.3 From ADC value to an electric field

The data from the SD and FD are processed in one software package, which is called Offline [32]. Because it can simultaneously process data from different detectors, it reflects the hybrid nature of the Pierre Auger Observatory. Within Offline, there is a clear separation between the hardware description of the *detector*, and the data within an *event*. Individual steps in data processing, like calibration and event reconstruction, are separated by

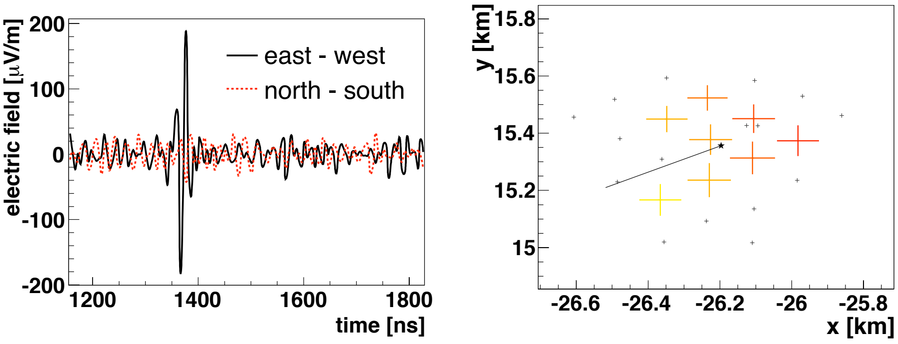

(a) (b)

Figure 3.8: The first cosmic-ray-induced pulse measured by AERA that was confirmed by the SD is shown in (a). In (b) the top view of the array with a reconstructed event is shown. The size of the colored crosses gives an indication of the signal strength in each polarization per station. The color coding indicates the relative timing of the pulses, and the black line is pointing from the barycenter of the radio signals towards the reconstructed direction.

modules. The *modules* have access to the *event* and the *detector* structures and there is no communication between individual *modules*. The only way to propagate information is by the *event* structure. In this way individual analysis steps can be replaced easily and the software package can be modified easily.

To process data coming from radio detectors and simulations, the Offline software package has been expanded [33]. The Offline framework is capable of processing data from all individual RD used in this thesis. Furthermore, output of the following radio simulation codes can be processed: REAS3[8], MGMR[13], and ReAires[9].

Usually, the radio signal is evaluated at a given location as function of time. This is either the outcome of a radio simulation or the result of a measurement. However, a lot of steps in processing radio data are performed in the frequency domain. Therefore, a data container is provided that holds both frequency and time domain of the same radio data. This data container makes sure that both domains are always up-to-date and therefore the user does not have to invoke Fourier transforms him/herself.

The radio data is treated on two levels, a *channel* level and a *station* level. The *channel* holds scalar data, for example the time series of ADC values recorded in one channel of a digitizer. At *station* level, the radio data is stored in a three-dimensional time-dependent vector, which represents the electric field at the location of a station. It is at this *station* level that the analyses in this thesis is performed.

In the following we will explain how to get from a measured time series of ADC counts, to a three-dimensional electric field vector. For this, we need to explain the concept of *response functions* used in the software package. The propagation of a signal through an element (hardware component) can be described by its complex gain. The complex gain transforms the amplitude and phase of an incoming signal to the amplitude and phase of the outgoing signal. The complex gain as a function of frequency is what we will call the *response function.* Note that this is only the so-called forward gain, the software package does not take into account reflections. Furthermore, the backward gain is being assumed equal to the inverse of the forward gain. This assumption is only valid when there is a perfect matching between the individual components.

By convoluting the recorded signal with the inverse *response function*, the influence of an element can be calibrated out. Therefore, if the *response function* of a detector is known, its influence can be calibrated out. The *response function* will only be known in the sensitive bandwidth of the detector. Therefore, the calibrated signal will still be bandpass limited.

The forward gain of the components used in the analogue chains of the RDSs are measured using a spectrum analyzer. Instead of measurements of the individual components in the chains (which is also possible), the overall measured forward gain of the analogue chains are filled in the *de-*

tector description.[2]

The response function of the antenna (the so-called *effective antenna length*) is frequency and direction dependent. Therefore, the direction of the incident electric field needs to be known. The measurement of the effective antenna length (gain and phase) is a difficult measurement; for a detailed description of such measurements see [34]. In Offline the effective antenna length is obtained from NEC-2 simulation software [35] and it includes the influence of reflections from the ground.

Within Offline the direction of the incident electric field is approximated from the direction of the shower axis. There are two ways to obtain this direction.

The first approach is to perform a directional reconstruction using the arrival times of the radio signals at the individual station of events. The direction of the radio signal in Offline is approximated by fitting a plane to the arrival times of the electric field. To obtain a first approximation of the electric field, the *channel* level data is divided by the *effective antenna height* using a default direction. This results in an electric field on which a direction can be reconstructed. Since the *channel* level is separated from the *station* level, this step can be repeated with the direction reconstructed from the previous step. This iterative procedure is repeated until the direction is converged. The default criteria for convergence is either that the direction of two subsequent iterations differ less than 0.5° or a maximum number of iterations is reached. Note that in this procedure the direction is reconstructed using the time domain, while the response function is applied in the frequency domain.

A second approach is to exploit the hybrid nature of the software package. Instead of reconstructing the direction of the shower axis from the radio signal, the shower axis obtained by the SD reconstruction is used. This only works if the radio event has a reconstructed SD counterpart. This method has two advantages. First, it does not need an iterative procedure

---

[2] When the BLS setup was taking measurements, the radio extension of Offline was not yet developed. Therefore the response functions weren't measured, and all channels are treated identical. The response function used in that case is a multiplication of general measurements of individual components.

and therefore it is considerably faster. Second, for direction reconstruction on the radio signal at least three stations with a signal are needed. By using the SD reconstructed axis, the electric field can be reconstructed for radio events with less than three stations. In this thesis only events are considered that have an SD counterpart, and therefore the latter method is used to reconstruct the electric field.

Chapter 4

Data sets and event selection

In this chapter the data that are selected for the polarization analyses in chapter 6 are described. The data that will be introduced in the following analyses contain EAS events that are measured with both the radio detectors and the surface detector. The selection of the SD reconstructed events is discussed in section 4.1. The criteria for selecting coinciding SD and RD events are described in section 4.2. Hardware configurations that have an influence on the quality of the data are discussed in section 4.3. The radio signal can be contaminated by noise sources. To minimize the influence of noise sources, proper windows are deselected in the frequency (section 4.4) and time domain (section 4.5). In order to compare the measured radio events to theoretical predictions, sets of simulations are generated, which are described in section 4.6. These simulations are also used to test the influence of noise on polarization parameters in chapter 5. During data taking the atmospheric electric field is monitored. Events are divided in different sets depending on electric field and monitoring conditions in section 4.7. Section 4.8 describes which geomagnetic field parameters are applied in further analyses.

4.1 Surface detector event selection

In the polarization analyses (see chapter 6), the dependence of the radio signal on the EAS geometry is investigated. The geometry of an EAS is obtained from the coinciding measurement by the SD. The SD reconstruction is performed using the reconstruction code from the Central Data Acquisition System: CDAS-v4r8 [36].
For the search of RD-SD time coincidences only EAS are considered when the shower axis is reconstructed near or in the field where the RDs are located. This is done in order to search efficiently and to reduce the background from random time coincidences. Therefore, two SD-reconstruction output selection files are generated. One selection is made of events near the BLS which is used to look for coincidences between the first prototype and SD or MAXIMA and SD. This selection consists of the following criteria:

1. The distance from the SD-reconstructed shower axis is less than 1500 m from RDS M2 *or*
2. SD tank *Olaia* (tank id 1325) is part of the event (see figure 3.6).

Another selection is made for events reconstructed near, or in, the AERA field. The selected reconstructed EASs fulfill these conditions:

1. The distance from the SD-reconstructed shower axis to SD tank Kathy Turner (tank id 1764) is less than 2500 m *or*
2. the event contains one of the SD tank shown in figure 4.1.

4.2 Surface detector - radio detector coincidences

For each radio detector described in chapter 3, a number of events is measured in coincidence with the SD. The event arrival time measured by the RD, t_{RD}, can be compared to the arrival time of its SD counterpart, t_{SD}. In figure 4.2 the distributions of time differences between t_{RD} and t_{SD} are shown for each individual RD. The data from the maxima setup is split

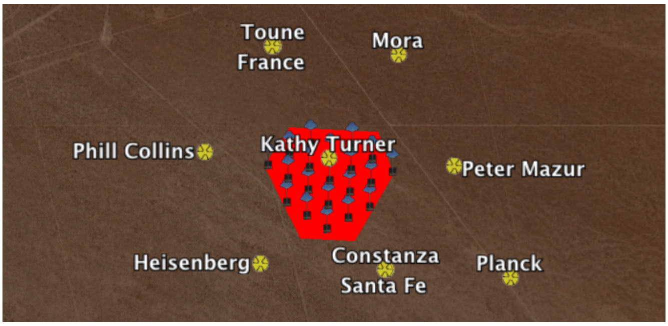

Figure 4.1: The RDSs of the first stage of AERA. The neighboring SD tanks are also shown.

in a set from 2010 and 2011, since the trigger settings were different. In addition, the noise situation of these two periods differ slightly, as becomes clear in section 4.4.

Within ±10 μs there is a clear excess around a central value, which is a strong indication that the RDs are triggering on the same EASs as the SD. The reasons for the time offset in $t_{\mathrm{RD}} - t_{\mathrm{SD}}$ are the different trigger settings in the DAQ and hardware properties (delays due to cables etc etc). This also explains the difference in time offsets between the individual series of RD measurements.
Figure 4.2 shows a few events that are triggered within 10 μs but that are far away from the peak of the distribution. These events are unlikely to be triggered by the same EAS as measured by the SD. Therefore we consider them as random coincidences and they will be rejected from physics analyses. To do so, a stricter time window for coincidences is defined in table 4.1. Note that the mean value in table 4.1 differs from the mean value in figure 4.2, this is because in table 4.1 the mean is calculated from events within the stricter coincidence windows only.

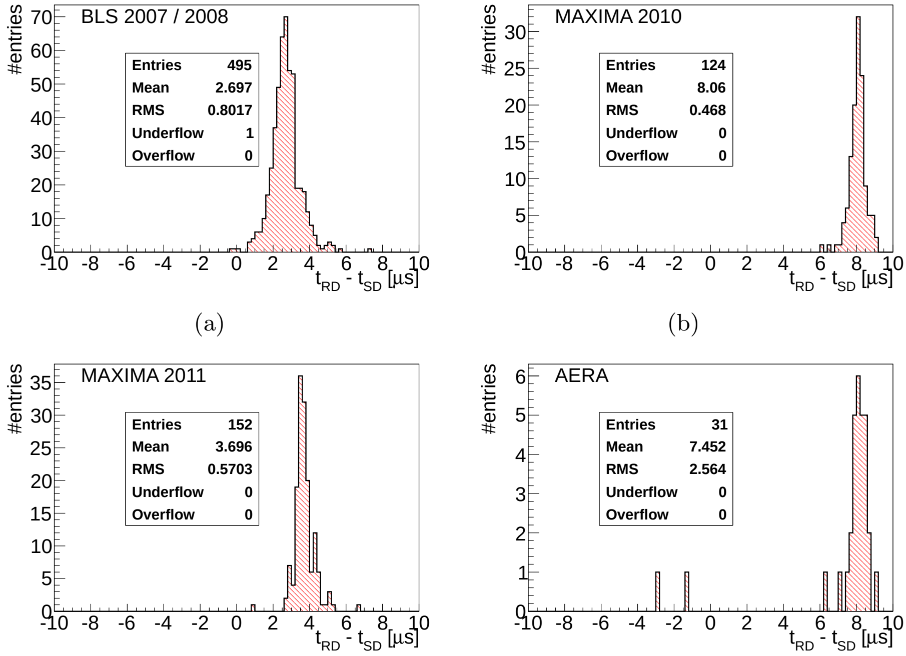

(a) (b)

(c) (d)

Figure 4.2: Time differences between the arrival time of the radio event, t_{RD}, and the surface detector event, t_{SD}.

4.3 Hardware properties

The hardware configuration has an influence on the data quality, which makes that some data are more suitable for physics analyses than others. The most important hardware components that have an influence on the data quality are listed below.

Filtering: During data taking several filter configurations were tested. In some cases there was different filtering in the individual channels of one RDS. If the frequency range of the filters in both channels do not overlap, it becomes hard to understand the polarization properties of

Setup	Mean (μs)	Window (μs)	Coincidences	Rejected
BLS 2007 / 2008	2.7	±2	482	13
MAXIMA 2010	8.1	±1.25	122	2
MAXIMA 2011	3.7	±1.7	150	2
AERA	8.1	±1.2	29	3

Table 4.1: The time windows in which events are defined as being RD-SD coincidences. The windows are centered on the mean value of the $t_{\mathrm{RD}} - t_{\mathrm{SD}}$. The resulting number of coincidences and the rejected random coincidences are presented.

these data.

Antenna type: On P3 (in the wired BLS setup) two antenna types (Wire - LPDA and LOFAR) have been tested, which were different from the antennas at P1 and P2 (Aluminum - LPDA). For this Wire - LPDA there is no antenna model available in the Offline framework. Because of the inverted V-shape of the LOFAR antenna the vertical and horizontal components are superimposed. For these reasons, it becomes impossible to reconstruct the polarization of the electric field from the measurements made at P3.

Antenna alignment: The importance of exactly knowing the orientation of the antennas came to light while trying to interpret the polarization properties of the data. Poorly knowing the orientation will result in a systematic uncertainty on the polarization of the signal from EAS in any analysis.

For the BLS 2007 / 2008 data set all points listed above need to be considered. Since the antennas are no longer there, the exact alignment is unknown. This introduces a systematic uncertainty on the polarization measurement of this data. For the MAXIMA 2010 data, the antennas were aligned with geomagnetic north on 20 May 2010. Before this date their exact orientations were unknown. Therefore this data will not be considered in physics analyses.

4.4 Selecting frequency ranges and removal of narrowband transmitters

As described in chapter 3, the RDSs are bandpass limited. Outside the sensitive bandwidth, it is not possible to reconstruct the electric field vector correctly. Therefore, a digital rectangular bandpass filter is applied after unfolding the detector response to constrain the data to the sensitive bandwidth.

The frequency range in which the RDSs are measuring is not free from narrowband transmitters. These narrowband transmitters interfere with the signal from EASs in the time domain. In addition, they influence the detection of the continuous galactic background [28], which is the main contribution to the uncertainty on any parameter derived from the EAS-signal. Therefore, it is crucial to clean the measurements from narrowband transmitters. They can easily be identified and removed by investigating the frequency spectrum.

Before removing any narrowband transmitter a Hann window is applied to the first and last 10% of the time series, which is done in order to reduce artificial side lobes of narrowband transmitters [37]. The first 10% of the samples are multiplied with a function that increases smoothly from 0 to 1, while in the last 10% they are multiplied with a function that decreases smoothly from 1 to 0. As a result, the time series becomes periodic.

From the modified time series a frequency spectrum is obtained, in which the power is set to zero at the frequencies containing a narrowband transmitters. Afterwards, an inverse Fourier transformation is performed to obtain the cleaned time series.

To identify the narrowband transmitters, average amplitude spectra are generated for the RD-SD coincidence events. This is done for each individual RDS, and the results are given in figures 4.3, 4.4, 4.5, 4.6 and 4.7. For each setup the caption mentions the frequency ranges from which the power is removed. Note that for the BLS setup there are two periods in which the analog filter chains are different. Therefore, different frequency ranges are selected. If a narrowband transmitter is present in only one electric field component, the power will be removed from the others as well. This is done in order to keep the selected frequency ranges of all electric field components equal.

It should be noticed that the average amplitude spectra still show some wiggles. These might be due to incorrect simulations of the *effective antenna length*. This is currently under investigation.

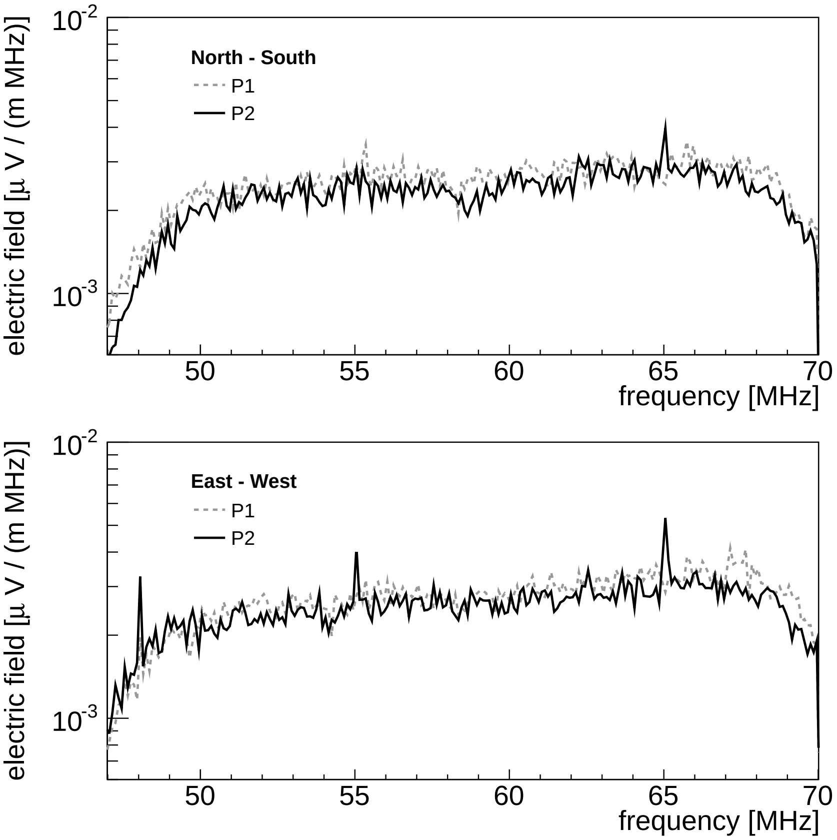

Figure 4.3: Average amplitude spectrum of the BLS setup with SBP60 filters for north-south (top) and east-west polarization (bottom). Frequency ranges that are removed offline are 55-55.2 MHz and 64.8-65.25 MHz in combination with a bandpass filter between 50 and 68 MHz.

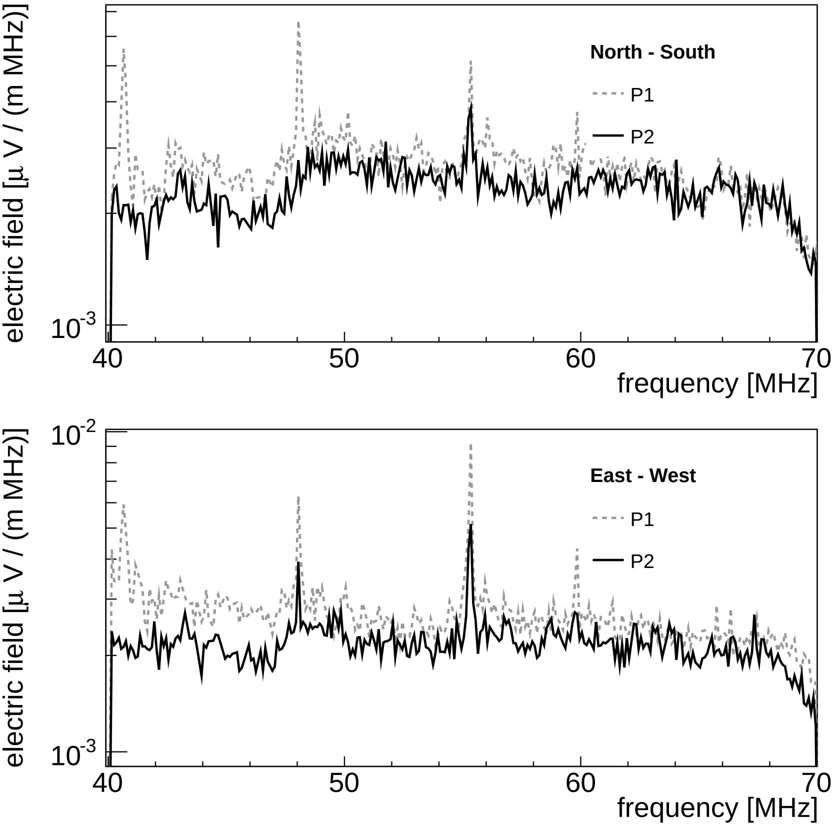

Figure 4.4: Average amplitude spectrum of the BLS setup with SHP25-SLP75 filters for north-south (top) and east-west (bottom) polarization. Frequency ranges that are removed offline are 47.8-48.3 MHz, 55.1-55.4 MHz and 61.1-61.5 MHz. In addition a bandpass filter between 42 to 68 MHz is applied.

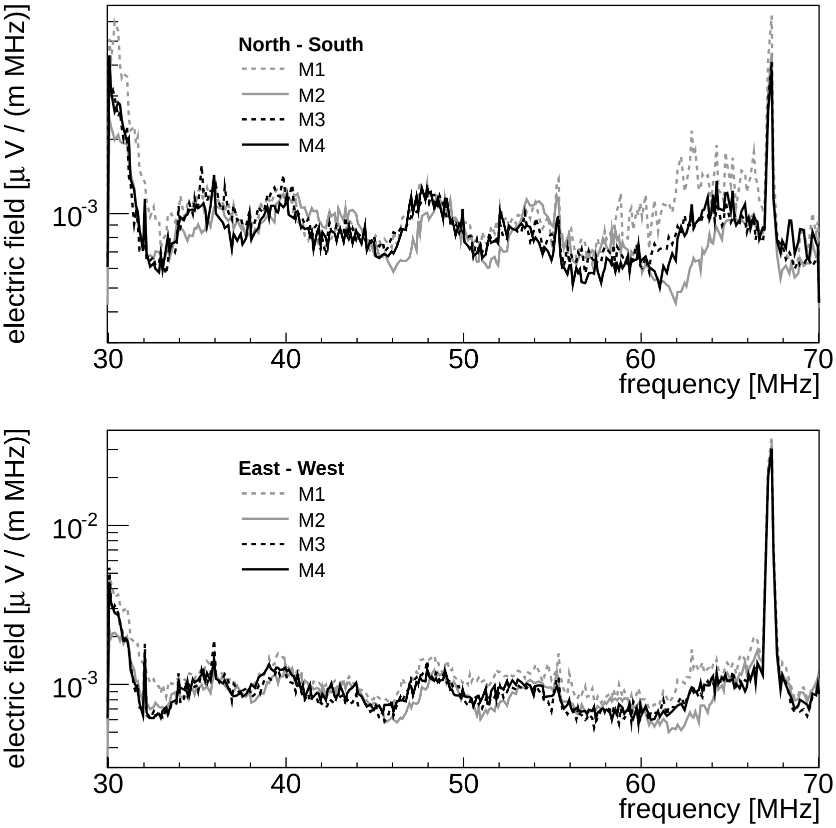

Figure 4.5: Average amplitude spectrum of the MAXIMA 2010 data set for north-south (top) and east-west (bottom) polarization. The frequency range 55-55.5 MHz is removed offline. In addition a bandpass filter between 35 to 58 MHz is applied.

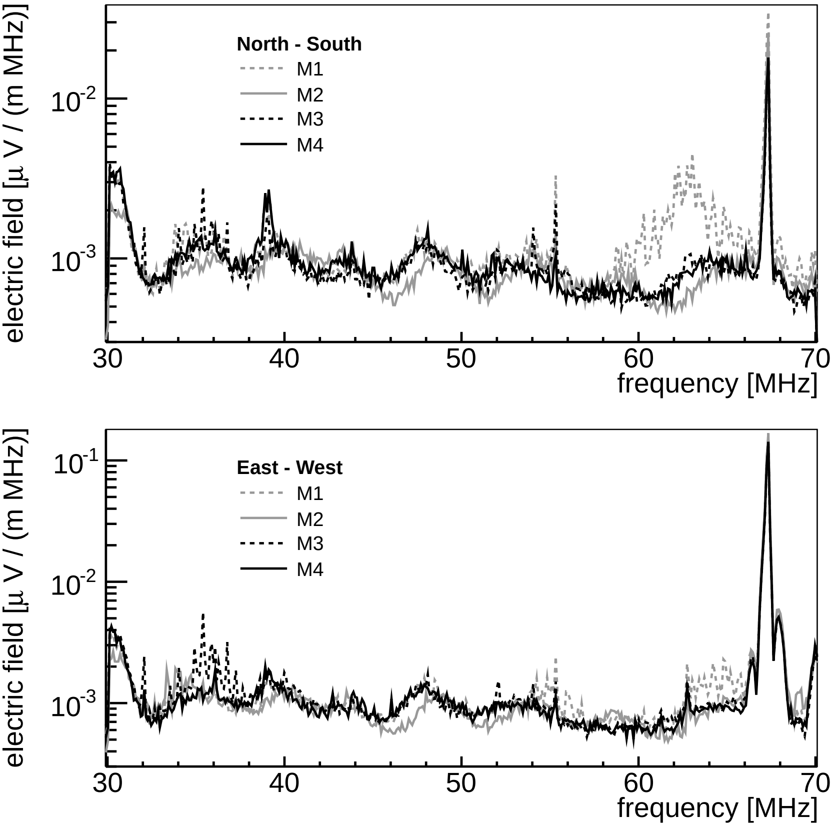

Figure 4.6: Average amplitude spectrum of the MAXIMA 2011 data set for north-south (top) and east-west (bottom) polarization. The frequency range 55-55.5 MHz is removed offline. In addition a bandpass filter between 40 to 58 MHz is applied.

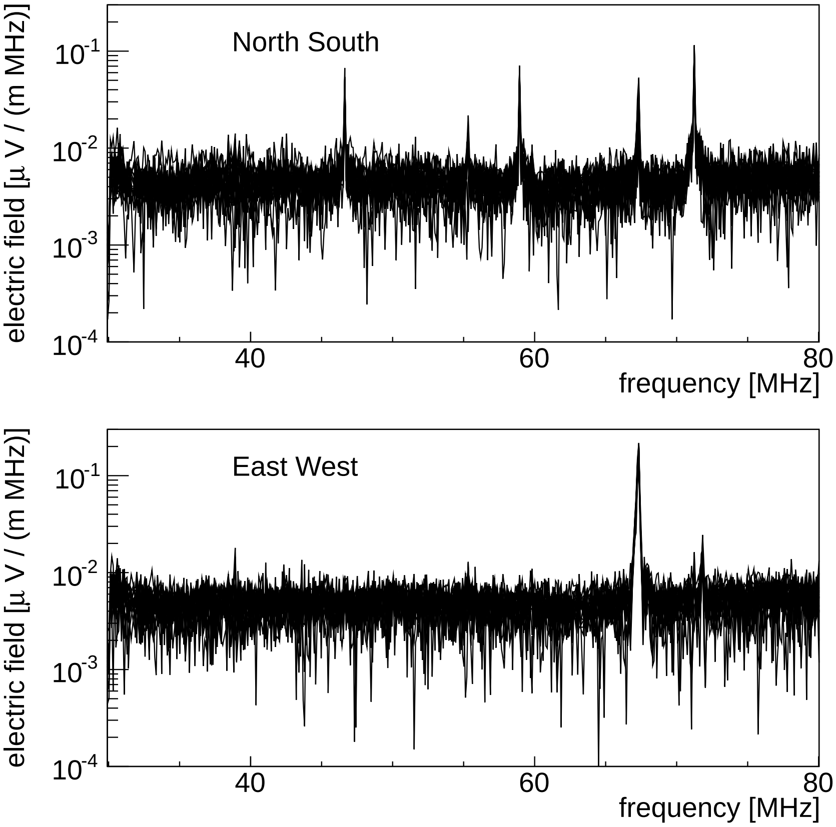

Figure 4.7: Average amplitude spectrum of all the individual AERA RDSs for north-south (top) and east-west (bottom) polarization. Frequency ranges that are removed are 46.56-46.70 MHz, 55.1-55.4 MHz, 58.8-59.1 MHz, 66.81-67.5 MHz and 71.19-71.3 MHz. In addition a bandpass filter between 30 to 80 MHz is applied.

4.5 Signal search window and noise windows

The EAS-signal can only be found in a limited region within the time-series, depending on the hardware configuration and DAQ settings. This can be used to limit the probability of selecting false pulses. To make a reliable estimate of the uncertainties on any derived parameter, a region in the time series is selected that is dominated by galactic noise. Taking these two points into consideration a signal search window (SSW) and a noise window (NW) are defined.

After cleaning the time series from narrowband transmitters an envelope can be calculated using a Hilbert transformation (section 5.1). The average enveloped time series is calculated per RDS for each RD-SD coincidence data set and for each RD the results are presented in figure 4.8, 4.9, 4.10, 4.11 and 4.12. In the captions it is stated how the SSW and the NW are chosen. The rise in the first μs and fall in the last μ is because of the applied Hann window.

For the MAXIMA and AERA data there is a clear peak at the location expected from the trigger settings. This EAS-signal peak is expected to show up at a fixed position in the time-series since the trigger decision is made locally in each RDS. However, for the BLS data set there is only one external trigger used for all RDSs. This means that depending on the shower geometry, the EAS-signals are at different locations within the time-series. In the average envelopes this results in a less prominent and sharp signal peak. The signal peak in AERA has by far the largest signal peak, this has two reasons. Since AERA is running in self-triggering mode each recorded measurement has a pulse with an amplitude above a certain threshold value. The BLS and the MAXIMA setups are triggering on particle detectors. Therefore, the strength of radio signal can be below the noise floor. The second reason is that the selected frequency band of AREA data is significantly larger than that for the MAXIMA and BLS prototype.

The noise floor of the BLS data shows some structure after the SSW. This is due to the trigger signal sent by the scintillator trigger and picked up in the signal chain, and is described for example in [28] and [29]. Because of the narrower selected frequency ranges in section 4.4 it is not as prominent as in the earlier observation. In both MAXIMA data sets there seem to be some clear peaks outside the SSWs. These peaks are caused by a few events that have enormous pulses outside the SSW. The NWs are chosen in such a way that they don't contain any of these peaks.

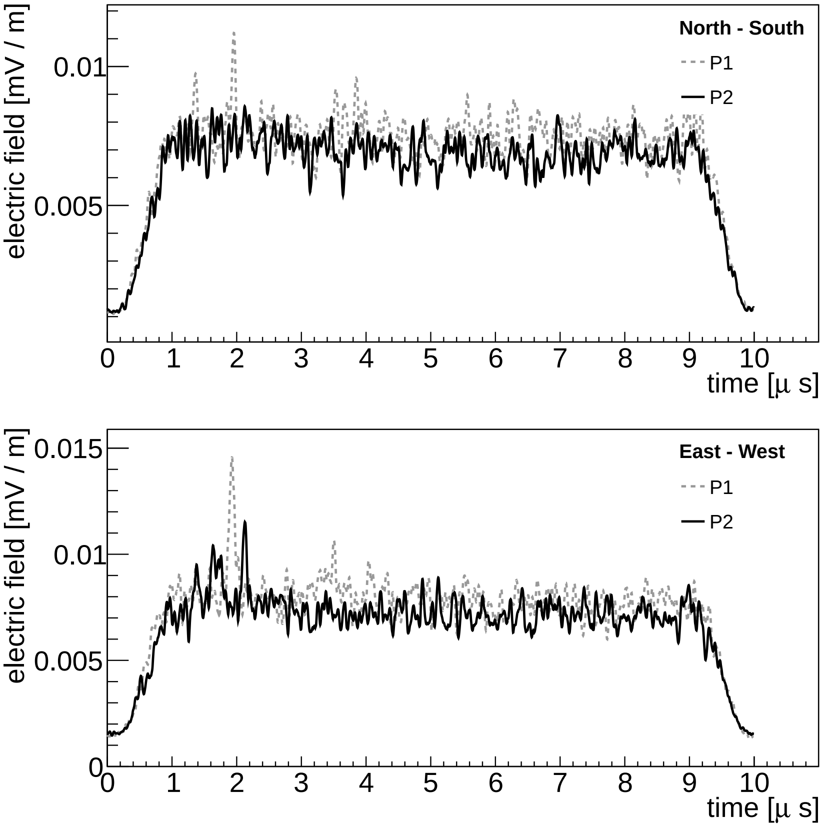

Figure 4.8: The average envelope of the BLS narrowband data set. From DAQ and hardware settings the signal search window is set between 1.65 and 2.35 μs. The noise window is set between 7 and 9 μs.

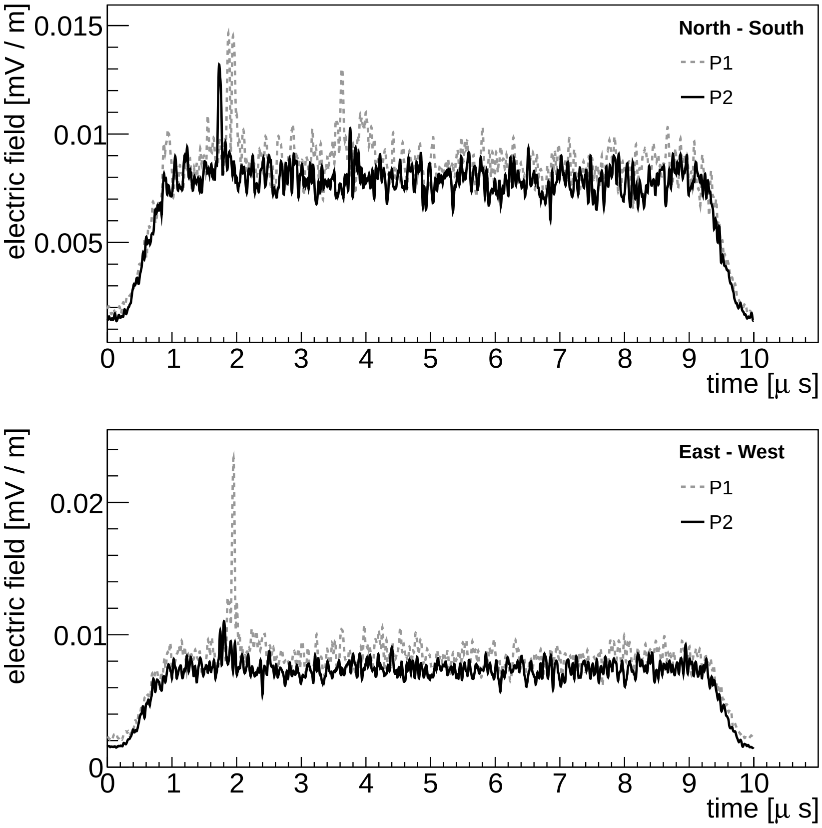

Figure 4.9: The average envelope of the BLS broadband data set. From DAQ and hardware settings the signal search window is set between 1.65 and 2.35 μs. The noise window is set between 4.5 and 6.2 μs.

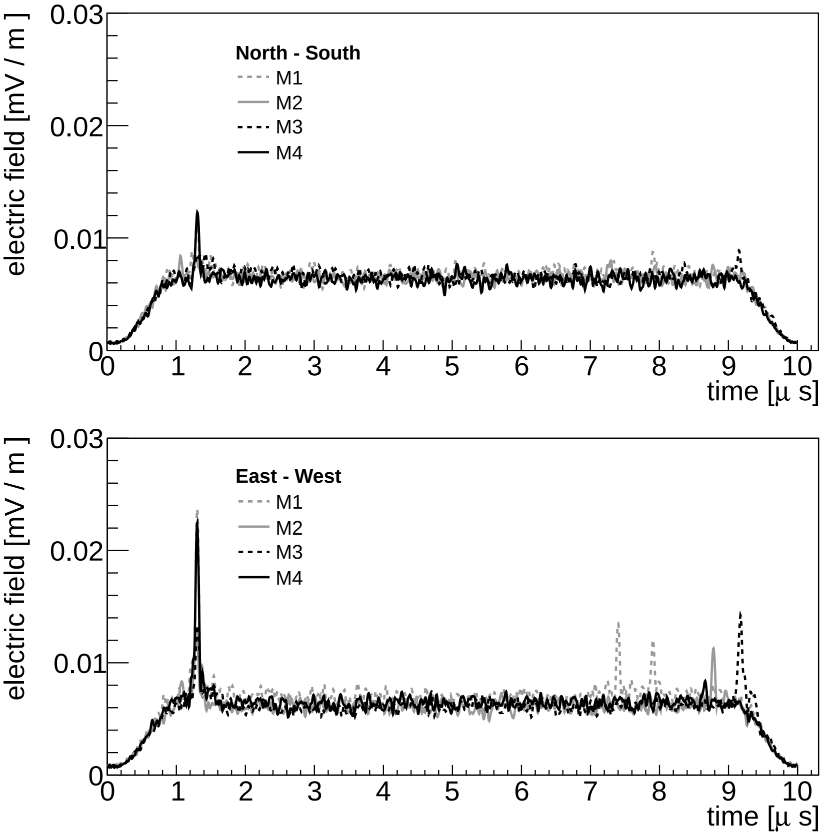

Figure 4.10: The average envelope of the MAXIMA 2010 data set. The average envelopes show a signal pulse around 1.3 μs. Therefore, the signal search window is set from 1 to 2 μs. The noise window is set between 3 and 6 μs.

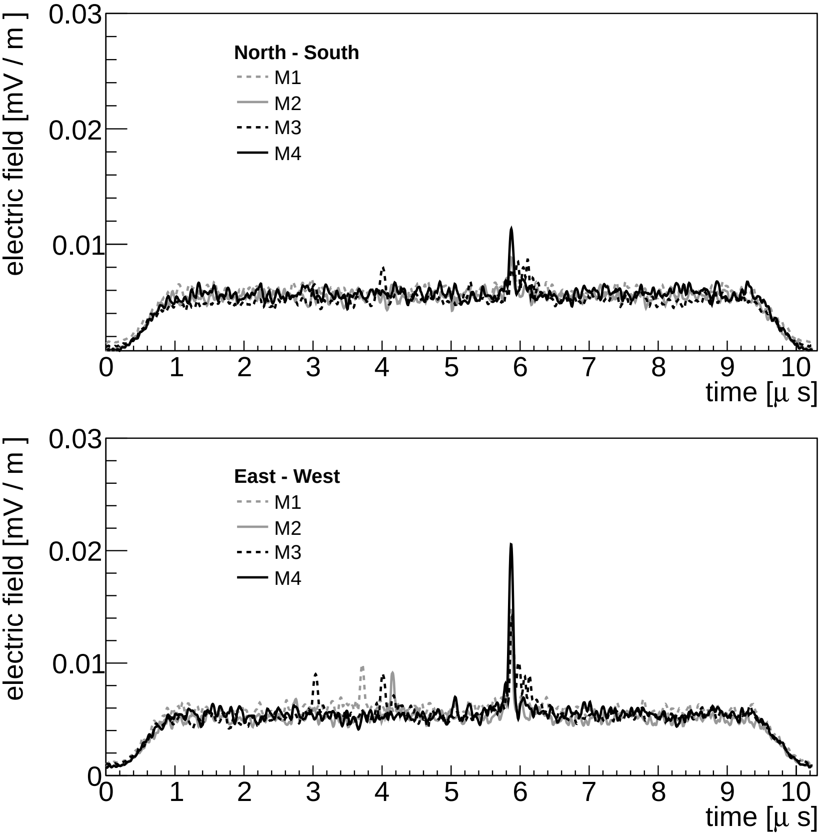

Figure 4.11: The average envelope of the MAXIMA 2011 data set. The average envelopes show a signal pulse around 6 μs. Therefore, the signal search window is set from 5.5 to 6.5 μs. The noise window is set between 7 and 9 μs.

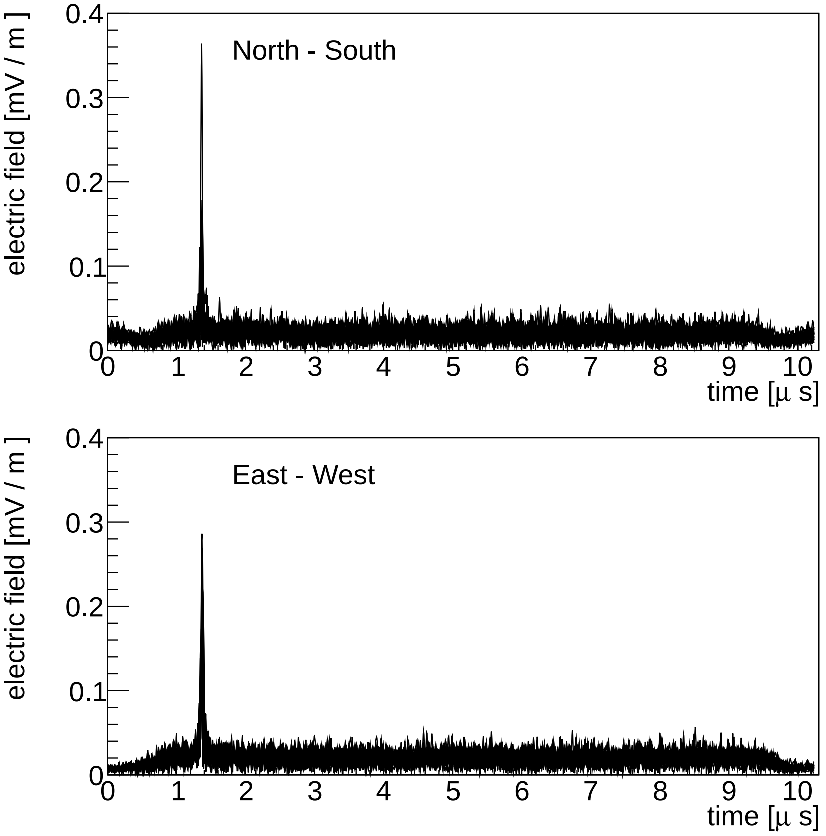

Figure 4.12: The average envelope of the AERA data set. The average envelopes shows a signal pulse around 1.4 μs. Therefore, the signal search window is set from 1 to 2 μs. The noise window is set between 4 and 7 μs.

4.6 Simulation sets

There are several packages available to simulate the emitted electric field by EAS. As described in chapter 2, they can be divided into two categories, microscopic and macroscopic. In this thesis only a comparison with data to the macroscopic geomagnetic radiation (MGMR) is performed. At the time of the writing of this thesis there was a set of simulations available for the RD-SD coincidences of MAXIMA in 2010 and a set for the BLS data. One MGMR-simulation (MGMR-v1.6) per event is generated using the SD-reconstructed parameters as input. In addition, sets of 100 shower parameters are generated per event according to the covariances of the SD-reconstructed parameters. Simulated events are also generated using these parameters sets as input. The method used for this procedure is documented in [38]. This results in a total of 101 simulations per event.
Within the MGMR model it is rather easy to switch off independent emission mechanisms. The set described above is once generated for MGMR including a charge-excess contribution and once without. The microscopic REAS3 simulations are not used as at the time of writing this thesis the simulated set was not yet created.

4.7 Thunderstorms

During thunderstorms, the radio signal emitted from air showers can be enhanced [39, 40]. The polarization of radio signals might also be altered by the influence of thunderstorms. To test this hypothesis, it is necessary to monitor the weather condition and flag events that have been measured during thunderstorms.

At the BLS and CRS weather stations equipped with an atmospheric electric field monitor are operated [41]. These electric field monitors take one measurement per second. These measurements indicate that the atmospheric electric field varies regularly within a period of one day, as shown in figure 4.13(a). However, during thunderstorms, larger fluctuations of the electric fields are measured. A period with large fluctuations is shown in

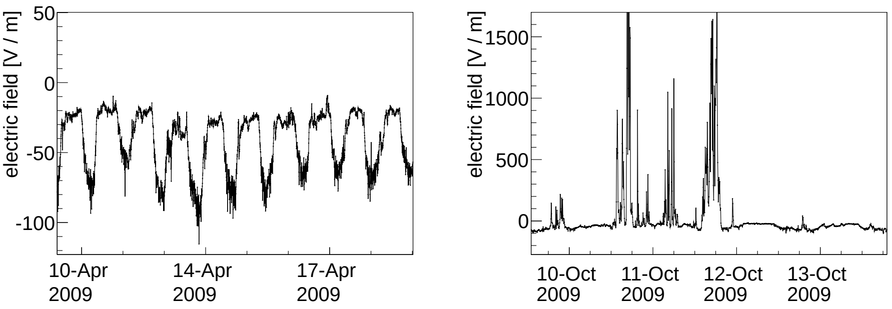

(a)

(b)

Figure 4.13: Electric field measurements at the BLS. In (a) the daily modulation of the atmospheric electric field is shown for a period of 10 days. In (b) a period of 4 days with large fluctuating atmospheric electric fields is shown.

4.13(b). Using the atmospheric electric field measurements, a flag has been designed to mark events that are likely to be influenced by thunderstorms. The measurements from the electric field monitors are analyzed in a time window of half an hour centered on the arrival time of the event. In this period the mean and the root mean square of the atmospheric electric field are calculated to monitor deviations from the regular daily modulation. In figure 4.14 the distributions of these means and root mean squares are shown for all events measured with SD tank *Olaia* in the years 2007 and 2008. From these distributions it is decided that we will flag an event as possibly influenced by a thunderstorm when the mean electric field $< -150\,\mathrm{V/m}$ or $> 50\,\mathrm{V/m}$ or when the root mean square of the electric field $> 30\,\mathrm{V/m}$. Events that are measured when the electric field monitor was not operating will also be flagged.

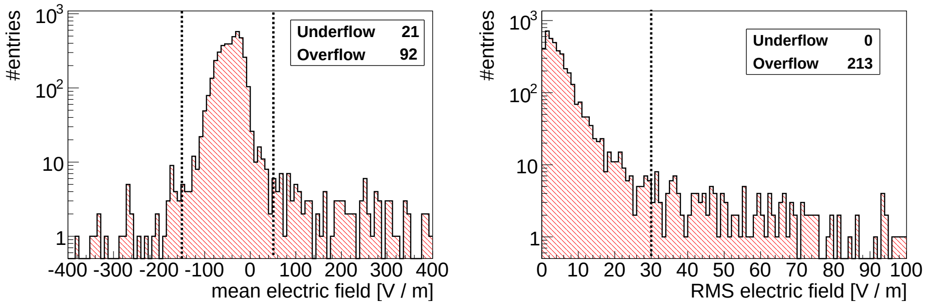

(a) (b)

Figure 4.14: Electric field measurements around SD events in the period 2007 and 2008 containing SD tank *Olaia*. In (a) the distribution of electric field averaged over 30 minutes around the events is shown, while in (b) the distribution of the rms for these events is shown. If the deviation from the mean distributions is larger than the conditions indicated with the dotted lines the events are flagged as possibly influenced by thunderstorms.

4.8 Geomagnetic field

The geomagnetic field plays an important role in the radio emission mechanism (Chapter 2). Therefore, it needs to be known at the time and location of the measurement. Global time dependent geomagnetic field models can be found on `http://www.ngdc.noaa.gov/geomagmodels/`, which also provides an online calculator. In figure 4.15(a) the total intensity of the model is shown in the region of South America. It should be noticed that the intensity in Malargüe Argentina is close to the world minimum. This has consequences for the strength of the leading geomagnetic emission mechanism, which will also be close to its world minimum. However, this has the effect that the Pierre Auger Observatory is an excellent location to study sub-leading emission mechanisms. In figure 4.15(b) the intensity of the geomagnetic field is shown in Malargüe in the time interval in which the RDs measured RD-SD coincidences.

Figure 4.16 shows how the direction of the geomagnetic field evolves in

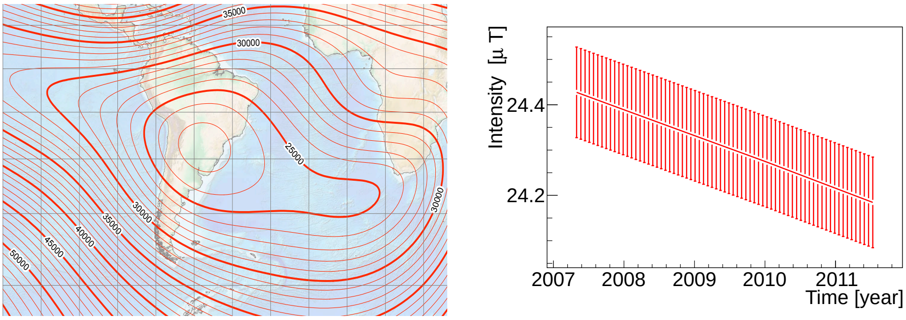

(a) (b)

Figure 4.15: The geomagnetic field. In (a) the intensity of the world magnetic field model is shown for the epoch of 2010, each contour interval corresponds to $1\,\mu T$. In (b) the intensity of the geomagnetic field in Malargüe Argentina is shown as a function of time.

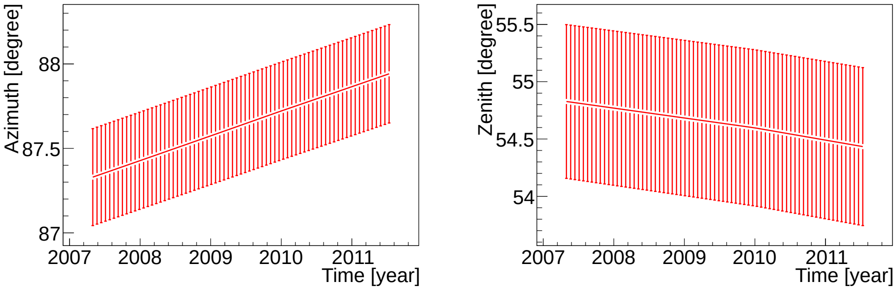

(a) (b)

Figure 4.16: Orientation of the geomagnetic field. In (a) the azimuth angle as a function of time is shown, while (b) shows the zenith angle.

time. The time-dependent direction, and its uncertainty, are taken into account in the analysis of the polarization of the radio signals from EAS.

Chapter 5

Analysis methods

In this chapter we describe how physics parameters are derived from the measurements with the radio detectors. The focus of this chapter is on parameters that describe the polarization of the radio signal. In section 5.1 the Hilbert transformation is explained, which allows us to go to a complex notation of the radio signal. This notation will be used in section 5.2 to define the Stokes parameters, which provide a base for polarization studies. In section 5.3 the general method for testing and validating calculated uncertainties is explained. This will be applied in section 5.4 and 5.6 to the Stokes parameters and derivatives of the Stokes parameters. How biases due to background can be removed from the Stokes parameters is described in section 5.5.

5.1 Hilbert transformation and envelope

There are benefits by going to a complex representation of measured values, for instance when calculating envelopes and Stokes parameters on the time dependent electric field. A way of doing this is by performing a Hilbert transformation on the time-series, which will result in a analytical complex representation of the time-series. The Hilbert transform is obtained by performing a Fourier transformation on the time-series, and rotating the complex phase of the positive frequencies by $\frac{-\pi}{2}$ and the negative frequencies by $\frac{\pi}{2}$, followed by the inverse Fourier transformation. This procedure provides the imaginary propagation of the measured values as a function of time. We will write this out explicitly for the typical scenario we have. Lets x_l be the l-th measurement out of a time-series with n subsequent measurements, then the discrete Fourier transformations are given by

$$
\begin{aligned}
f_k &= \frac{1}{\sqrt{n}} \sum_{l=1}^{n} x_l e^{-2\pi\imath\, kl/n} && (5.1)\\
x_l &= \frac{1}{\sqrt{n}} \sum_{k=1}^{n} f_k e^{2\pi\imath\, kl/n}, && (5.2)
\end{aligned}
$$

in which f_k gives the representation of the measurement in the frequency domain. The amplitudes of the positive frequencies are given by f_k with $1 \leq k < (n-1)/2$, while the negative frequencies are given by f_k with $(n+1)/2 < k \leq n$. The Hilbert transformation is obtained by shifting the phase of the complex frequencies by $\frac{-\pi}{2}$ for positive and $\frac{\pi}{2}$ for negative frequencies,

$$
\hat{f}_k = \begin{cases} \frac{1}{\sqrt{n}} \sum_{l=1}^{n} -\imath\, x_l e^{-2\pi\imath\, kl/n} & \text{if } k < n/2 \\ \frac{1}{\sqrt{n}} \sum_{l=1}^{n} x_l \imath\, e^{-2\pi\imath\, kl/n} & \text{if } k > n/2 \\ 0 & \text{if } k = n/2, \end{cases}
$$

where $\hat{f}_k$ now describes the Hilbert transformed frequency spectrum. Performing the inverse Fourier transformation on $\hat{f}_k$ results in the Hilbert transform of time sample m

$$\begin{aligned}
\hat{x}_m &= \frac{1}{\sqrt{n}}\sum_{k=1}^{n}\hat{f}_k e^{2\pi\imath\, km/n} \\
&= \frac{1}{n}\Big(-\sum_{k=1}^{n/2}\sum_{l=1}^{n}\imath\, x_l e^{\frac{2\pi\imath\, k(m-l)}{n}} + \sum_{k=n/2}^{n}\sum_{l=1}^{n}\imath\, x_l e^{\frac{2\pi\imath\, k(m-l)}{n}}\Big) \\
&= \frac{1}{n}\Big(\sum_{k=1}^{n/2}\sum_{l=1}^{n}x_l\big(\sin(\frac{2\pi k(m-l)}{n}) - \imath\,\cos(\frac{2\pi k(m-l)}{n})\big) \\
&+ \sum_{k=n/2}^{n}\sum_{l=1}^{n}x_l\big(-\sin(\frac{2\pi k(m-l)}{n}) + \imath\,\cos(\frac{2\pi k(m-l)}{n})\big)\Big).
\end{aligned} \tag{5.3}$$

This can be simplified by using the following relations,

$$\sum_{k=1}^{n/2}\cos(\frac{2\pi k(m-l)}{n}) = \sum_{k=n/2}^{n}\cos(\frac{2\pi k(m-l)}{n}) \tag{5.4}$$

$$\sum_{k=1}^{n/2}\sin(\frac{2\pi k(m-l)}{n}) = -\sum_{k=n/2}^{n}\sin(\frac{2\pi k(m-l)}{n}). \tag{5.5}$$

Equation (5.3) becomes

$$\hat{x}_m = \frac{2}{n}\sum_{k=1}^{n/2}\sum_{l=1}^{n}x_l\sin(\frac{2\pi k(m-l)}{n}) \tag{5.6}$$

$$= \sum_{l=1}^{n}F_{lm}x_l, \tag{5.7}$$

with

$$F_{lm} = \frac{2}{n}\sum_{k=1}^{n/2}\sin(\frac{2\pi k(m-l)}{n}). \tag{5.8}$$

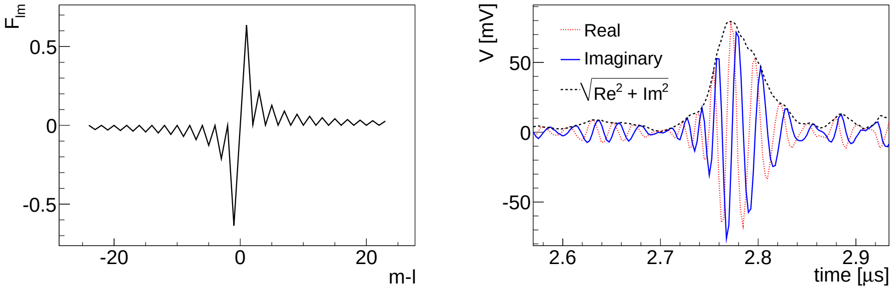

(a) (b)

Figure 5.1: In (a) F_{lm} is shown as a function of $m-l$ for $n = 256$. In (b) the real measured signal x_l, its imaginary propagation obtained by a Hilbert transform $\hat{x}_m$ (equation (5.6)), and the calculated envelope (equation (5.12)) are shown.

As an example the F_{lm} terms as a function of $m-l$ are shown in figure 5.1(a) for $n = 256$. From this it is clear that the contribution to the Hilbert transformation drops rapidly when $|m-l|$ is increasing. From equation (5.8) and figure 5.1(a) the following useful properties can be derived,

$$F_{lm} = 0, \qquad \text{if } l - m \text{ is even,} \tag{5.9}$$

and,

$$F_{lm} = -F_{ml}. \tag{5.10}$$

A general property of a Hilbert transform H is,

$$H(H(\vec{x})) = -\vec{x}. \tag{5.11}$$

One application of the Hilbert transform is to calculate an envelope on a bandpass limited time-series. Let $\vec{x}$ be a time-series, then the envelope $\vec{\tilde{x}}$ of $\vec{x}$ can be calculated by

$$\tilde{x}_i = \sqrt{x_i^2 + \hat{x}_i^2}. \tag{5.12}$$

An example of the Hilbert transformation to calculate the complex propagation and the envelope of a time-series are shown in Figure 5.1(b).

5.2 Stokes parameters

The Stokes parameters form the standard base in which classical radio astronomy describes average polarization properties of a signal. We will use this parameterization to describe polarization signature of the radio emission of EAS. Let $\vec{x}$ be the time-series of the East - West component of the electric field, and $\vec{y}$ the North - South component of the electric field. Then we can define the Stokes parameters in the horizontal plane as

$$
\begin{aligned}
S_0 &= I \equiv \frac{1}{n}\sum_{i=1}^{n}(x_i^2 + \hat{x}_i^2 + y_i^2 + \hat{y}_i^2) && (5.13)\\
S_1 &= Q \equiv \frac{1}{n}\sum_{i=1}^{n}(x_i^2 + \hat{x}_i^2 - y_i^2 - \hat{y}_i^2) && (5.14)\\
S_2 &= U \equiv \frac{2}{n}\sum_{i=1}^{n}(x_i y_i + \hat{x}_i \hat{y}_i) && (5.15)\\
S_3 &= V \equiv \frac{2}{n}\sum_{i=1}^{n}(\hat{x}_i y_i - x_i \hat{y}_i), && (5.16)
\end{aligned}
$$

in which $\hat{x}_i$ and $\hat{y}_i$ are the complex propagation obtained by equation (5.6). Note that there are two conventions on the notation of the Stokes parameters, they are both given here for completeness. In the following we will stick to the S_i convention, since this allows us to write some equations in a more compact way. Stokes parameter S_0 gives the total intensity of the signal, S_1 and S_2 give the linear components of the polarization, while S_3 gives the circular component.

An application of the Stokes parameter S_0 is to define signal windows around a short pulse. Instead of averaging S_0 (equation (5.13)) over a number of samples, a time-series can be constructed in which the intensity is calculated for each sample. On such a time-series a signal window can

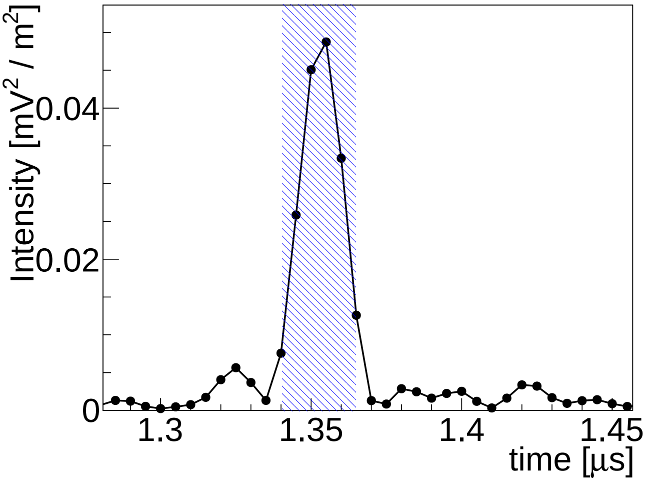

Figure 5.2: Example of a signal window. The shaded area shows a full width half maximum window. The edges are rounded to the neighboring sample in such a way that the window size is slightly increased.

be determined independent of the polarization of the signal. In figure 5.2 an example of a signal window is shown. The signal window here is defined as the full width half maximum window (FWHM), in which the edges are rounded to the nearest sample away from the mean, such that the window size (slightly) increases.

5.3 Calculating and testing uncertainties on parameters

Before calculating the uncertainties on the Stokes parameters, we first describe a general method that will be applied to calculate and validate the uncertainties on parameters derived from the time-series.

The uncertainties on variables $\{x_1 \ldots x_i \ldots x_n\}$ are propagated to the parameter $P(x_1, \dots, x_i, \dots, x_n)$ using standard error propagation:

$$\sigma_P = \sqrt{\sum_{i=1}^{n} \sum_{j=1}^{n} \frac{\partial P}{\partial x_i} \frac{\partial P}{\partial x_j} \mathrm{Cov}(x_i, x_j)}, \tag{5.17}$$

in which $\mathrm{Cov}(x_i, x_j)$ gives the covariance of variable x_i with x_j.

In the measured time-series the main contribution to the uncertainty is due to background radiation. Our signal pulses are typically in the order of 50 ns long. However, after receiving a trigger the radio detector stations are read out typically for 10 μs (depending on the settings of the data acquisition). This provides us with a measurement of the background at practically the same moment at which the signal from an air shower was measured. From this background measurement the covariances in equation (5.17) will be estimated. If $\{x_1 \dots x_i \dots x_N\}$ represent the subsequent samples in a time-series then the covariance is calculated as the auto covariance $R(k)$

$$\mathrm{R}(k) = \mathrm{Cov}(x_i, x_j) = \sum_{l=0}^{N-k} \frac{(x_l - \mu_x)(x_{l+k} - \mu_x)}{N - k - 1}, \tag{5.18}$$

in which μ_x is the mean value of x_i over N samples. $R(k)$ gives the estimate of the covariance between a sample and the sample at time lag $k = |i - j|$ from it. Due to the limited bandwidth (~50 MHz) in which the radio signal is measured with respect to the sampling rate (200 MHz or 400 MHz, depending on the setup) the samples in the time-series are correlated. An example of the correlation coefficients $R(k)/R(0)$ is given in figure 5.3 (the noise is generated using the procedure described later in this section). The oversampling fraction, q , can be calculated as:

$$q = \frac{f}{2\Delta f}, \tag{5.19}$$

in which f is the sampling frequency, and Δf the bandwidth. The noise shown in figure 5.3 is oversampled by a factor 4. Therefore, more or less 5 neighboring samples are correlated. To estimate the uncertainty on a

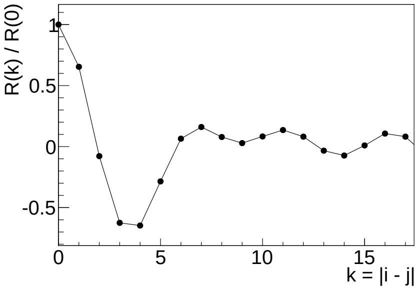

Figure 5.3: The correlation coefficient as a function of the time lag between samples. The correlation coefficient is calculated in noise that is generated with a sampling rate of 400 MHz which has been bandpass filtered between 30 - 80 MHz.

parameter derived from multiple samples in a time-series, it is crucial to take the covariances between the samples into account. To validate and interpret the uncertainty σ_P on a parameter P, as calculated with equations (5.17) and (5.18), we simulate the influence of background on simulated air shower signals. The air shower simulations used are MGMR simulations that are generated for the MAXIMA 2010 RD - SD coincidences (section 4.6). For each event the electric field is simulated at each RDS, with a total of 124 coincidences this results in 492 simulated signal pulses.
The noise time-series are obtained by generating a flat amplitude spectrum with a Gaussian fluctuation on it. To each frequency bin a phase drawn from a random uniform distribution is assigned. To generate correlations between samples, the noise spectra are bandpass filtered between 30 and 80 MHz. This corresponds to the design frequency band of the AERA setup. Performing an inverse Fourier transformation on the frequency spectrum results in a noise time-series. An example is shown in figure 5.4. This generated noise is added to simulated signals in the frequency domain. Afterwards, a bandpass filter is applied on the combined spectrum between 30 and 80 MHz. An example of noise added to one component of the electric field from a simulated signal is shown in figure 5.5. Within a time-series we

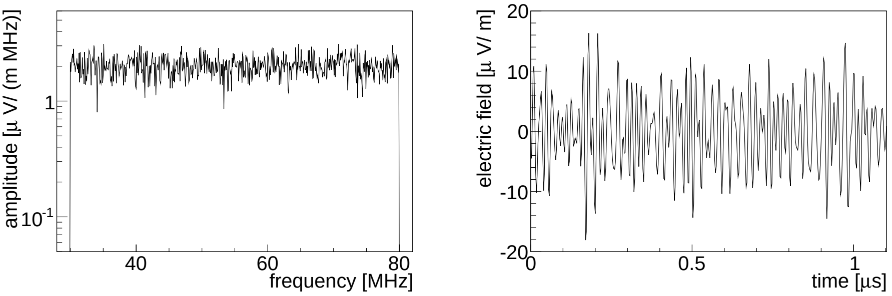

(a) (b)

Figure 5.4: Example of generated noise. Figure (a) shows the generated amplitude spectrum, which is bandpass filtered between 30 and 80 MHz. The amplitudes are randomly drawn from a Gaussian distribution with mean of $2\,\mu\mathrm{V\,m^{-1}\,MHz^{-1}}$ and a spread of $0.4\,\mu\mathrm{V\,m^{-1}\,MHz^{-1}}$. To each amplitude a randomly drawn phase is added. In (b) the time-series obtained after a Fourier transformation of the frequency spectrum is shown.

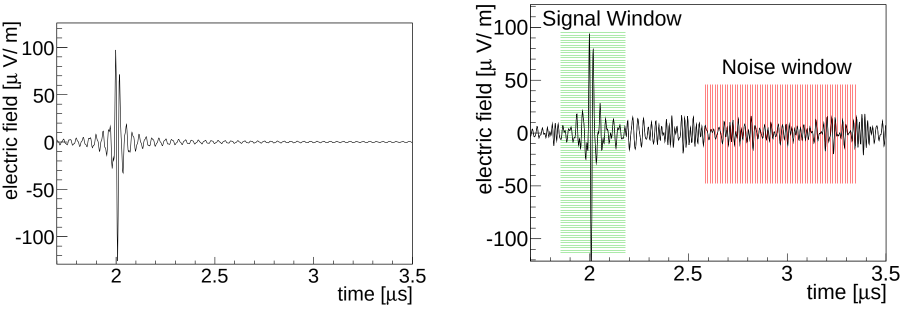

(a) (b)

Figure 5.5: Example of generated noise added to a simulated signal. In (a) the east west component of a bandpass filtered simulated signal is shown. In (b) noise is added to the signal and possible choices of a signal window and a noise window are shown.

choose a signal window in which a parameter P is calculated. The covariance between the samples is obtained from a noise window. This window should be chosen such that the background is dominant. An example of a signal and noise window is shown in figure 5.5(b). To test the influence of noise on parameter P we add noise to each simulated signal time-series and repeat this N times. This results in distribution of calculated Ps. For each time P is calculated, the uncertainty σ_P is calculated as well. From these distributions the mean values can be obtained, $\bar{P}$ and $\bar{\sigma}_P$. To interpret the calculated uncertainty on P, the fraction F_P of P's that is between $\bar{P} - \bar{\sigma}_P$ and $\bar{P} + \bar{\sigma}_P$ is calculated,

$$F_P = \frac{\int_{\bar{P}-\bar{\sigma}_P}^{\bar{P}+\bar{\sigma}_P} f(P)dP}{\int_{-\infty}^{\infty} f(P)dP}, \tag{5.20}$$

with $f(P)$ the distribution of P's after adding noise. Equation (5.20) tells us how to interpret the calculated uncertainties and gives us the possibility to compare them to a Gaussian expectation.

To the whole set of simulated pulses we add a constant noise level as described above. Since the simulated pulses have different properties, we can study the dependency of the uncertainty on different signal to noise levels for a parameter. In the following sections the results are shown for several parameters.

5.4 Uncertainties on the Stokes parameters

Each Stokes parameter is a function of time-series $\vec{x}$ and $\vec{y}$. Using standard error propagation (equation (5.17)) the uncertainty on Stokes parameter S_k can be obtained from:

$$\begin{aligned}
\sigma_{S_k}^2 &= \sum_{i=1}^{n}\sum_{j=1}^{n}\Big(\frac{\partial S_k}{\partial x_i}\frac{\partial S_k}{\partial x_j}\mathrm{Cov}(x_i, x_j) + \frac{\partial S_k}{\partial y_i}\frac{\partial S_k}{\partial y_j}\mathrm{Cov}(y_i, y_j) \\
&+ \frac{\partial S_k}{\partial x_i}\frac{\partial S_k}{\partial y_j}\mathrm{Cov}(x_i, y_j) + \frac{\partial S_k}{\partial x_j}\frac{\partial S_k}{\partial y_i}\mathrm{Cov}(x_j, y_i)\Big),
\end{aligned} \tag{5.21}$$

with the covariances calculated using equation (5.18).

As an example we will write out the complete calculation of the uncertainty on S_0. Let us first examine the partial derivatives in the first term of equation (5.21),

$$\begin{aligned}
\frac{\partial S_0}{\partial x_i} &= \frac{1}{n}\frac{\partial}{\partial x_i}\Big(\sum_{k=1}^{n}(x_k^2+\hat{x}_k^2+y_k^2+\hat{y}_k^2)\Big) \\
&= \frac{1}{n}\frac{\partial}{\partial x_i}\Big(\sum_{k=1}^{n}(x_k^2+\hat{x}_k^2)\Big) \\
&= \frac{1}{n}\frac{\partial}{\partial x_i}\sum_{k=1}^{n}(x_k^2)+\frac{1}{n}\frac{\partial}{\partial x_i}\sum_{k=1}^{n}(\hat{x}_k^2). \qquad (5.22)
\end{aligned}$$

The first term in equation (5.22) becomes

$$\frac{1}{n}\frac{\partial}{\partial x_i}\Big(\sum_{k=1}^{n}(x_k^2)\Big)=\frac{2x_i}{n}. \qquad (5.23)$$

The second term in equation (5.22) becomes

$$\begin{aligned}
\frac{1}{n}\frac{\partial}{\partial x_i}\Big(\sum_{k=1}^{n}(\hat{x}_k^2)\Big) &= \frac{1}{n}\frac{\partial}{\partial x_i}\Big(\sum_{k=1}^{n}(\sum_{l=1}^{n}F_{lk}x_l)(\sum_{m=1}^{n}F_{mk}x_m)\Big) \\
&= \frac{1}{n}\sum_{k=1}^{n}\frac{\partial}{\partial x_i}\Big((\sum_{l=1}^{n}F_{lk}x_l)(\sum_{m=1}^{n}F_{mk}x_m)\Big) \\
&= \frac{1}{n}\sum_{k=1}^{n}\Big(F_{ik}\sum_{m=1}^{n}F_{mk}x_m+F_{ik}\sum_{l=1}^{n}F_{lk}x_l\Big) \\
&= \frac{1}{n}\sum_{k=1}^{n}2F_{ik}\hat{x}_k \\
&= \frac{1}{n}\sum_{k=1}^{n}-2F_{ki}\hat{x}_k \\
&= \frac{2x_i}{n}. \qquad (5.24)
\end{aligned}$$

In the last steps properties of the Hilbert transformation are used (equation (5.10) and (5.11)). Therefore, equation (5.22) becomes

$$\frac{\partial S_0}{\partial x_i} = \frac{4x_i}{n} \tag{5.25}$$

Taking the derivatives with respect to y_i can be done in the same way. The uncertainty on S_0 becomes,

$$\begin{aligned} \sigma^2_{S_0} &= \frac{16}{n^2}\sum_{i=1}^{n}\sum_{j=1}^{n}\Big(x_i x_j \mathrm{Cov}(x_i,x_j) + y_i y_j \mathrm{Cov}(y_i,y_j) \\ &+ x_i y_j \mathrm{Cov}(x_i,y_j) + x_j y_i \mathrm{Cov}(x_j,y_i)\Big), \end{aligned} \tag{5.26}$$

with the covariances estimated from equation (5.18). The derivation of the uncertainty on the other Stokes parameters can be performed in a similar way. The results are,

$$\begin{aligned} \sigma^2_{S_1} &= \frac{16}{n^2}\sum_{i=1}^{n}\sum_{j=1}^{n}\Big(x_i x_j \mathrm{Cov}(x_i,x_j) + y_i y_j \mathrm{Cov}(y_i,y_j) \\ &- x_i y_j \mathrm{Cov}(x_i,y_j) - x_j y_i \mathrm{Cov}(x_j,y_i)\Big) \end{aligned} \tag{5.27}$$

$$\begin{aligned} \sigma^2_{S_2} &= \frac{16}{n^2}\sum_{i=1}^{n}\sum_{j=1}^{n}\Big(y_i y_j \mathrm{Cov}(x_i,x_j) + x_i x_j \mathrm{Cov}(y_i,y_j) \\ &+ x_j y_i \mathrm{Cov}(x_i,y_j) + x_i y_j \mathrm{Cov}(x_j,y_i)\Big) \end{aligned} \tag{5.28}$$

$$\begin{aligned} \sigma^2_{S_3} &= \frac{16}{n^2}\sum_{i=1}^{n}\sum_{j=1}^{n}\Big(\hat{y}_i \hat{y}_j \mathrm{Cov}(x_i,x_j) + \hat{x}_i \hat{x}_j \mathrm{Cov}(y_i,y_j) \\ &- \hat{x}_i \hat{y}_j \mathrm{Cov}(x_i,y_j) - \hat{x}_j \hat{y}_i \mathrm{Cov}(x_j,y_i)\Big). \end{aligned} \tag{5.29}$$

To validate the calculation of the uncertainty we will perform the test described in section 5.3. Noise is added 300 times to each simulated signal. This is done to each component of the electric field independently. In each

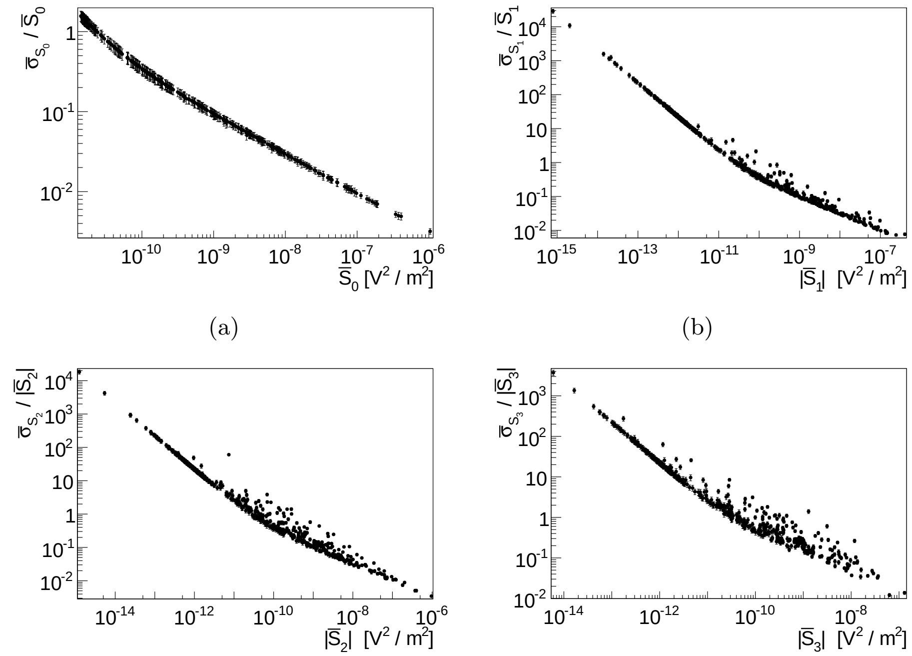

(a) (b)

(c) (d)

Figure 5.6: Relative uncertainty on the four Stokes parameters. The error bars on the points indicate the uncertainties on the uncertainties, which are estimated by the root mean square of the distributions of the uncertainties after adding 300 time noise to a simulated signal.

of the time-series we now estimate the covariances in a noise window of 1 μs. The Stokes parameters are calculated in a signal window, which is defined as the full width half maximum window (FWHM) in the time-series of S_0 as described in section 5.2. The maximum amplitude that is used for the FWHM window is the maximum in a window of 400 ns wide around the location where we know our simulated signal to be. The relative uncertainty as a function of the strength of the Stokes parameter is shown in figure 5.6. As an estimation of the relative uncertainty, the mean of the distribution of uncertainty $\bar{\sigma}_{S_i}$ is divided by the mean of the distribution of the parameter $|\bar{S}_i|$. For each Stokes parameter the relative uncertainty drops as a function of the strength of the parameter. For S_0 this goes rather smoothly, while for the other parameters there seems to be some scatter on it.

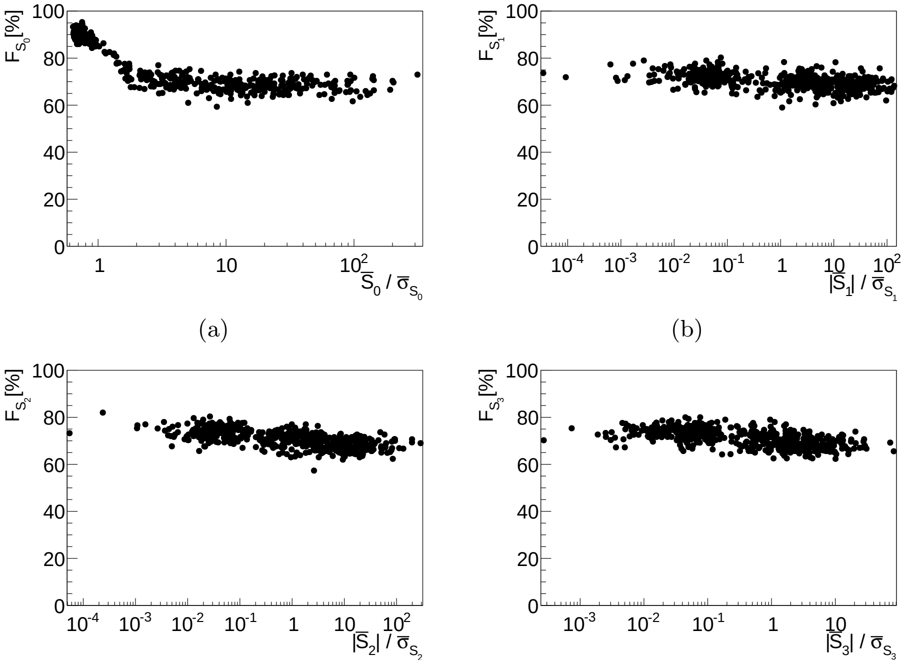

(a) (b)

(c) (d)

Figure 5.7: The fraction F_{S_i} (equation 5.20) as a function of signal to noise for all Stokes parameters. Signal to noise is defined as $\bar{S}_i/\bar{\sigma}_{S_i}$.

To understand the meaning of the calculated uncertainties the fraction, F_{S_i} (equation (5.20)), of S_i's that is between $\bar{S}_i - \bar{\sigma}_{S_i}$ and $\bar{S}_i + \bar{\sigma}_{S_i}$ is shown as a function of the strength of the parameters in figure 5.7. These figures give an indication at what signal to noise level, the calculation of uncertainties become unusable as an standard deviation estimate. It is clear that the uncertainty on S_0 gives is overestimated for low signal to noise levels ($S_0/\sigma_{S_0} < 2$), whereas the other Stokes parameters seem to be rather reliable for all signal to noise levels. In figure 5.8 the distributions of F_{S_i} are shown for each Stokes parameter above the signal to noise cut $\bar{S}_i/\bar{\sigma}_{S_i} > 3$. To each distribution a Gaussian function is fitted. This shows that ∼68 % of the noise realizations would have been between $\bar{P} - \bar{\sigma}_P$ and $\bar{P} + \bar{\sigma}_P$. The width of the Gaussian fit shows that this is in agreement with an one σ spread of a normal distributed variable (for which $F = 68.3\,\%$). The χ^2/ndf shows that the shape is well described by a Gaussian.

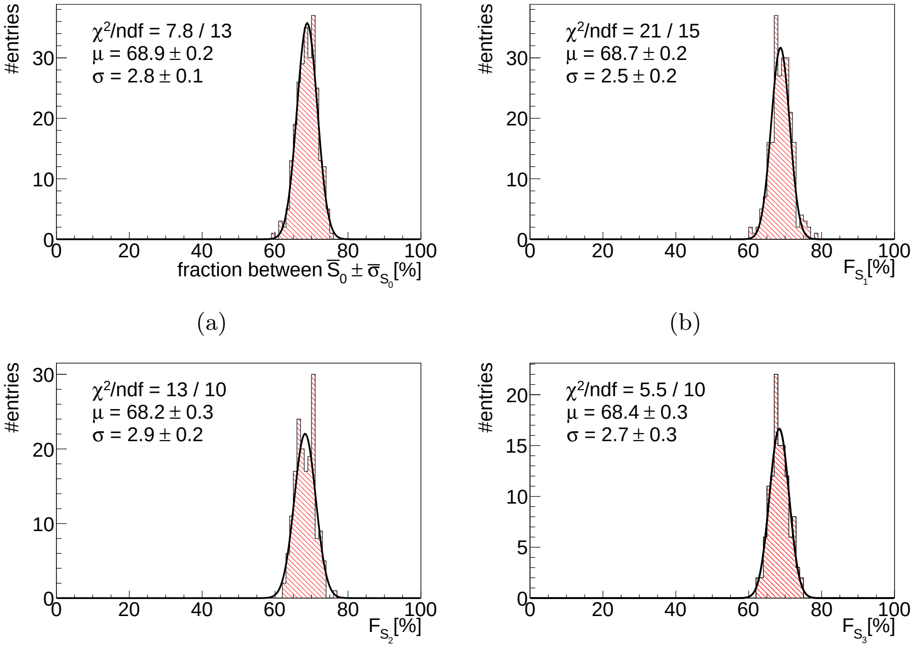

(a)

(b)

(c)

(d)

Figure 5.8: Distribution of the fraction F_{S_i} after a signal to noise cut $\bar{S}_i/\bar{\sigma_{S_i}} > 3$. To each distribution a Gaussian function is fitted.

5.5 Biases on the Stokes parameters

The presence of noise can introduce a bias on the measured value of a parameter. To obtain the true value of this parameter it is necessary to correct the Stokes parameters for these biases. Let us consider a time sample x_i which consist out of a signal ($\vec{s}$) and a noise ($\vec{b}$) component, $x_i = s_{xi} + b_{xi}$. To estimate the bias on S_0 and S_1 let us consider,

$$\sum_{i=1}^{N} x_i^2 = \sum_{i=1}^{N} (s_{xi}^2 + b_{xi}^2 + 2b_{xi}s_{xi}) \approx \sum_{i=1}^{N} (s_{xi}^2 + b_{xi}^2). \tag{5.30}$$

The approximation in the last term is valid if the phases between the signal and background are uncorrelated, the bias that remains is the $\sum_i^N b_{xi}^2$. A way to correct for this is to estimate b_{xi}^2 in a noise window. The true value of the signal can be estimated by,

$$\sum_{i=1}^{N} s_i^2 \approx \sum_{i=1}^{N} (x_{xi}^2 - b_{xi}^2) \approx \sum_{i=1}^{N} (x_{xi}^2 - \overline{b_x^2}), \tag{5.31}$$

in which $\overline{b_x^2}$ is the mean value of b_{xj}^2 determined in a noise window. Removing the bias from Stokes parameters S_0 and S_1 will result in,

$$S_0 \approx \frac{1}{n} \sum_{i=1}^{n} (x_i^2 + \hat{x}_i^2 + y_i^2 + \hat{y}_i^2 - \overline{b_x^2} - \overline{b_{\hat{x}}^2} - \overline{b_y^2} - \overline{b_{\hat{y}}^2}) \tag{5.32}$$

$$S_1 \approx \frac{1}{n} \sum_{i=1}^{n} (x_i^2 + \hat{x}_i^2 - y_i^2 - \hat{y}_i^2 - \overline{b_x^2} - \overline{b_{\hat{x}}^2} + \overline{b_y^2} + \overline{b_{\hat{y}}^2}). \tag{5.33}$$

It is clear that S_0 will always needed to be corrected for the bias from the noise. However, on S_1 there will only be a bias if the noise levels in $\vec{x}$ and $\vec{y}$ are different. To estimate the biases on S_2 and S_3 lets consider the cross terms between time-series $\vec{x}$ and $\vec{y}$,

$$\begin{aligned}\sum_i^N x_i y_i &= \sum_{i=1}^N ((s_{xi}+b_{xi})(s_{yi}+b_{yi})) \\ &= \sum_{i=1}^N (s_{xi}s_{yi}+s_{xi}b_{yi}+b_{xi}s_{yi}+b_{xi}b_{yi}) \\ &\approx \sum_{i=1}^N s_{xi}s_{yi}. \qquad (5.34)\end{aligned}$$

This approximation is valid if the phases of the noise in both channels are uncorrelated and if the phases between the signal in one channel and the noise in the other channel are uncorrelated. Since S_2 and S_3 only consist out of cross terms between $\vec{x}$ and $\vec{y}$ no bias is expected. To verify the approximations and the calculation on the biases we perform a test. To one simulated pulse we add noise 6500 times. The noise level added to the x component of the electric field is 3 times bigger than the noise level added to the y component. The noise is generated similar to the validation test in section 5.3. Two sets of data are generated, one in which no correction on the Stokes parameters is applied, and another one in which the biasses are corrected according to equations (5.32), (5.33) and (5.34). The resulting distributions are compared with the true value of each Stokes parameter in Figure 5.9. It is clear that the uncorrected S_0 and S_1 show a bias. The corrections proposed in equation (5.32) and (5.33) result in a distribution of which the mean values are in agreement with the true value of S_0 and S_1. From the distributions shown in Figure 5.9(c) and 5.9(d) it is clear that S_2 and S_3 do not need to be corrected for any biases.

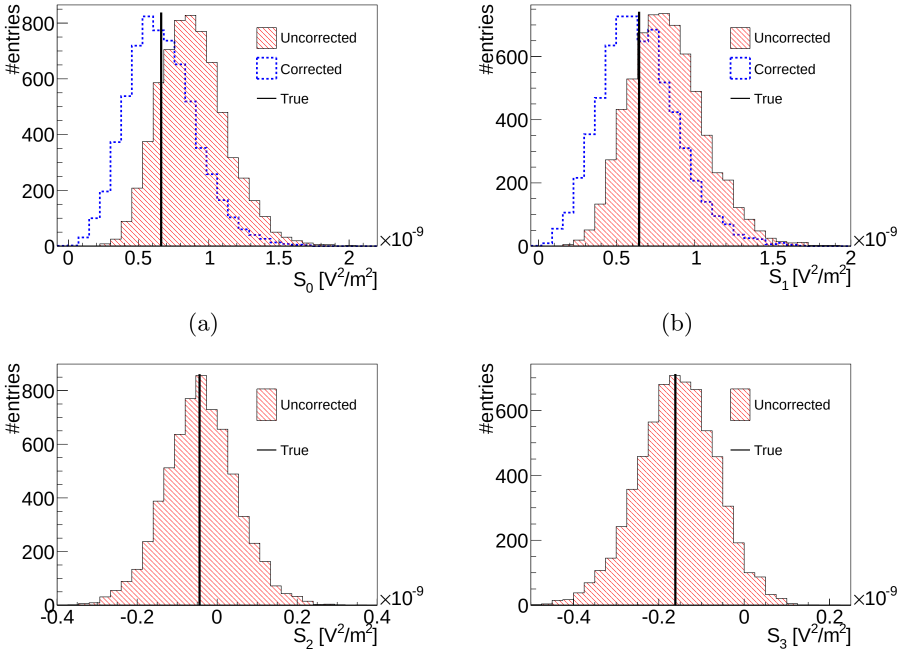

(a) (b)

(c) (d)

Figure 5.9: Verification of the procedure to remove the biases on the signal introduced by background. Each figure shows the distribution of the uncorrected Stokes parameter after adding noise 6500 times. These distribution are compared with the true value of the corresponding Stokes parameter. For Stokes parameters S_0 (a) and S_1 (b) also the corrected distributions are shown. For S_0 the mean of the corrected distribution is $(6.68 \pm 0.03) \times 10^{-10}\,\mathrm{V}^2/\mathrm{m}^2$, while the true value is $6.68 \times 10^{-10}\,\mathrm{V}^2/\mathrm{m}^2$. For S_1 the mean of the corrected distribution is $(6.479 \pm 0.03) \times 10^{-10}\,\mathrm{V}^2/\mathrm{m}^2$, while the true value is $6.47 \times 10^{-10}\,\mathrm{V}^2/\mathrm{m}^2$. For S_2 the mean of the uncorrected distribution is $-4.024 \times 10^{-11}\,\mathrm{V}^2/\mathrm{m}^2$, while the true value is $-4.023 \times 10^{-11}\,\mathrm{V}^2/\mathrm{m}^2$. For S_3 the mean of the uncorrected distribution is $-1.572 \times 10^{-11}\,\mathrm{V}^2/\mathrm{m}^2$, while the true value is $-1.5785 \times 10^{-11}\,\mathrm{V}^2/\mathrm{m}^2$.

5.6 Derivatives of Stokes parameters

Because the Stokes parameters might not provide the ideal basis to understand the physics underlying the polarization signature, we will introduce a few variables based on the Stokes parameters. The intensity of the part of the signal that is polarized is given by

$$I_p = \sqrt{S_1^2 + S_2^2 + S_3^2}. \tag{5.35}$$

The intensity of the signal that is linear polarized is given by

$$L = \sqrt{S_1^2 + S_2^2}. \tag{5.36}$$

By using equation 5.35 and 5.36, the semi-major axis, A, and the semi-minor axis, B, of the polarization ellipse are obtained using

$$A = \sqrt{\frac{I_p + L}{2}}, \tag{5.37}$$

$$B = \sqrt{\frac{I_p - L}{2}}. \tag{5.38}$$

The angle of polarization, ϕ_p, that A makes with respect to the x-axis (East - West) is given by

$$\phi_p = \frac{1}{2}\tan^{-1}(S_2/S_1), \tag{5.39}$$

in which the relative sign of S_2, and S_1 will be taken into account to determine the correct quadrant in which ϕ_p lies. To complete the full description of the polarization ellipse we now only need the helicity of the ellipse,

$$h = \begin{cases} 1 & \text{if } S_3 \geq 0 \\ -1 & \text{if } S_3 < 0. \end{cases} \tag{5.40}$$

From section 2.6 it is clear that the interference between the different emission mechanisms give rise to a change in ϕ_p and introduce a circular component. Therefore, it will be useful to determine a parameter, C, which describes the amount and the helicity of circular polarization,

$$C = \frac{hB}{A}. \tag{5.41}$$

For all parameters derived from the Stokes parameters the uncertainty can be calculated by propagating the uncertainties derived on the Stokes parameters. The uncertainty σ_P on a parameter $P(\vec{S})$ is given by,

$$\sigma_P = \sqrt{\sum_{i=0}^{3}\sum_{j=0}^{3} \frac{\partial P}{\partial S_i}\frac{\partial P}{\partial S_j}\mathrm{Cov}(S_i, S_j)}. \tag{5.42}$$

Stokes parameter S_1, S_2, and S_3 are assumed to be uncorrelated. Therefore, equation (5.42) simplifies for parameters $P(S_1, S_2, S_3)$ to,

$$\sigma_P = \sqrt{\sum_{i=1}^{3} \left(\frac{\partial P(S_1, S_2, S_3)}{\partial S_i}\right)^2 \sigma_{S_i}^2}, \tag{5.43}$$

with σ_{S_i} from equations (5.27), (5.28), and (5.29).

To calculate the uncertainty on ϕ_p we have to take the partial derivatives to the individual Stokes parameters,

$$\begin{aligned} \frac{\partial \phi_p}{\partial S_1} &= \frac{1}{2}\frac{\partial}{\partial S_1}\left(\tan^{-1}(S_2/S_1)\right) \\ &= \frac{1}{2(1+(S_2/S_1)^2)}\frac{\partial}{\partial S_1}\frac{S_2}{S_1} \\ &= \frac{-1}{2(1+(S_2/S_1)^2)}\frac{S_2}{S_1^2} \\ &= \frac{-S_2}{2(S_1^2+S_2^2)}, \end{aligned} \tag{5.44}$$

and similar,

$$\frac{\partial \phi_p}{\partial S_2} = \frac{S_1}{2(S_1^2+S_2^2)}. \tag{5.45}$$

By using equation (5.43) the uncertainty on ϕ_p becomes,

$$\begin{aligned} \sigma_{\phi_p} &= \sqrt{(\frac{\partial \phi_p}{\partial S_1}\sigma_{S_1})^2 + (\frac{\partial \phi_p}{\partial S_2}\sigma_{S_2})^2} \\ &= \sqrt{\frac{(\sigma_{S_1}^2 S_2^2 + \sigma_{S_2}^2 S_1^2)}{4(S_2^2 + S_1^2)^2}}. \end{aligned} \tag{5.46}$$

To validate the calculation of σ_{ϕ_p} a test similar to the one in described section 5.3 is performed. To each simulated signal, noise is added 300 times independently in the x and y component of the electric field. Then, for each time noise is added, the Stokes parameters and their uncertainties are calculated according to the method described in section 5.4. From these parameters ϕ_p and σ_{ϕ_p} are calculated. Since ϕ_p only depends on S_1 and S_2, it is expected that σ_{ϕ_p} depends on the uncertainty on L (equation (5.36)). To express this quantity, the following signal to noise ratio is defined,

$$\mathrm{SNR}_L \equiv \frac{\overline{\sqrt{S_1^2 + S_2^2}}}{\sqrt{\overline{\sigma_{S_1}}^2 + \overline{\sigma_{S_1}}^2}} = \frac{\overline{L}}{\sqrt{\overline{\sigma_{S_1}}^2 + \overline{\sigma_{S_1}}^2}}, \tag{5.47}$$

This is calculated using the average of the 300 times noise is added to the simulated signal. In Figure 5.10(a) the dependence of σ_{ϕ_p} is shown as a function of SNR_L. To interpret the value of σ_{ϕ_p}, the fraction F_{ϕ_p} (equation 5.20) is calculated. The calculation of the mean of the uncertainty is straight forward, $\bar{\sigma}_{\phi_p} = \sum_{i=0}^{n=300} \sigma_{\phi_p,i}$. This is however not the case for calculating the mean of ϕ_p. Due to its nature, the range of ϕ_p is limited between -90° and +90° (equation (5.39)). Let $\phi_{p,i}$ be the polarization angle calculated from a single time noise is added to a simulated signal, then the mean of the distribution can be calculated using

$$\bar{\phi}_p = \tan^{-1}\left(\frac{\sum_{i=1}^{n} \sin(\phi_{p,i})}{\sum_{i=1}^{n} \cos(\phi_{p,i})}\right). \tag{5.48}$$

However, this will not work if the distribution is around +90°, which is the same as -90°. In this case the mean can be calculated using the following procedure. First shift all the negative angles of the distribution by

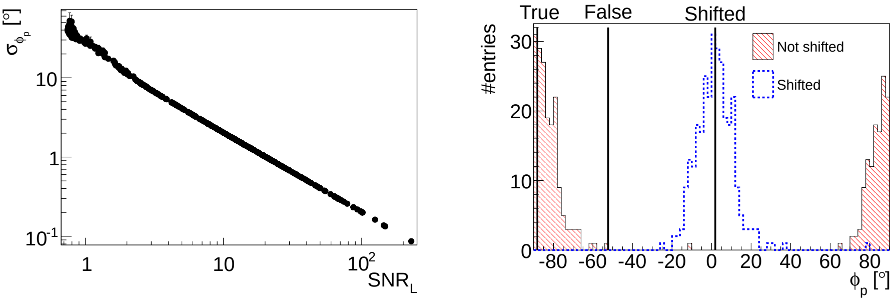

(a) (b)

Figure 5.10: In (a) the dependence of σ_{ϕ_p} on the SNR_L (equation (5.47)) is shown. The markers are drawn at the mean of the distribution of the 300 calculated values of σ_{ϕ_p} per pulse. The error bars give the root mean square of this distribution. In (b) an example is shown in which the mean of the distribution (Not shifted) can not simply be calculated by equation (5.48). The line labeled False gives the result if you would simply use equation (5.48). By shifting the positive angles -90° and the negatives +90° the shifted distribution is obtained, from which the mean (line labeled Shifted) can be calculated by equation (5.48). After shifting back, the calculated mean of the shifted distribution, the true mean of the distribution is obtained (line with label True).

+90° and the positive angles by -90 degree. This procedure results in a distribution around 0°, from which the mean can be calculated according to equation (5.48). If the mean angle is positive we obtain the true mean of the distribution by shifting it -90°, while for a negative mean we need to shift it by +90°. An example of this procedure is shown in figure 5.10(b). The shifting procedure will be applied when the following condition applies:

$$\Big(\sum_{i=1}^{n} \sin(\phi_{p,i}) < \sum_{i=1}^{n} \cos(\phi_{p,i})\Big) \ \textbf{and}\ \Big(\sum_{i=1}^{n} |\sin(\phi_{p,i})| > \sum_{i=1}^{n} \cos(\phi_{p,i})\Big). \tag{5.49}$$

A $\phi_{p,i}$ falls within the range $\bar{\phi}_p \pm \sigma_{\phi_p}$, when $|\bar{\phi} - \phi_{p,i}| < \bar{\sigma}_{\phi_p}$ or when

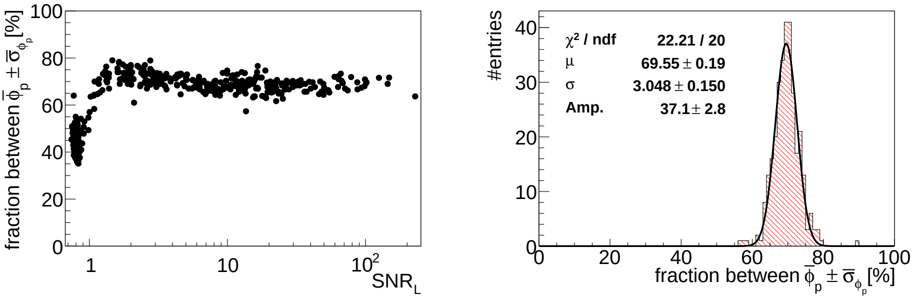

(a) (b)

Figure 5.11: Figure (a) shows the fraction of the ϕ_p distribution obtained by adding noise 300 times to a pulse that falls within $\bar{\phi}_p \pm \bar{\sigma}_{\phi_p}$. The fraction is plotted as a function of the SNR_L. Figure (b) shows the distribution of this fraction after a $\mathrm{SNR}_L > 1$. A Gauss function with mean μ and standard deviation σ is fitted to this distribution.

$|\bar{\phi} - \phi_{p,i} - 180°| < \bar{\sigma}_{\phi_p}$. The fraction of the $\phi_{p,i}$'s that fall within $\bar{\phi}_p \pm \bar{\sigma}_{\phi_p}$, as an function of SNR_L is shown in Figure 5.11(a). This figure shows that for $\mathrm{SNR}_L < 2$ the value of sigma σ_{ϕ_p} can not be used as an reliable estimator for the uncertainty. For values of $\mathrm{SNR}_L > 2$ the value of σ_{ϕ_p} becomes stable. The distribution of the fraction above $\mathrm{SNR}_L = 2$ is shown in Figure 5.11(b). To this distribution a Gauss function is fitted, which describes this distribution well. The fitted mean is 69.6 % and the width is 3.0 %. Therefore we conclude that the uncertainty on ϕ_p (calculated by equation (5.46)) due to uncorrelated noise can be interpreted such that 69±3 % of all values would fall between $\phi_p \pm \sigma_p$.

Chapter 6

Emission mechanisms and their polarization

In this chapter the polarization of radio signals from EAS is analyzed. In section 6.1, the polarization angle expected for a geomagnetic emission model is compared with the measured polarization angle. In section 6.2, the influence of a charge-excess contribution on the polarization angle is presented. In the next section the polarization angle is used to calculate the relative strength of the charge-excess and geomagnetic contributions. The dependence of this strength on EAS parameters is investigated in section 6.4. Afterwards, a one-to-one comparison between simulations and measurements is performed. In chapter7, conclusions are drawn from the polarization study and the results are discussed.

6.1 Polarization signature of geomagnetic radiation

From theory and experiment, it is expected that the dominant contribution to the radio emission of EASs in the MHz regime is due to the propagation of the EAS through the geomagnetic field. In the late sixties and early seventies several experiments recorded radio pulses that were in agreement with geomagnetic emission. A review of these experiments and their findings is given in [7]. More recently, the dominant geomagnetic contribution has been confirmed by the CODALEMA experiment [42].

If the particles in the EAS are propagating with velocity $\vec{v}$ through the geomagnetic field $\vec{B}$ then the electric field $\vec{E}$ is polarized as

$$\vec{E}^G = |E^G|\hat{e}^G \propto \hat{d} \times \hat{b}, \tag{6.1}$$

with $\hat{e}^G$ a unit vector in the direction of the electric field, $\hat{d}$ the direction of the shower axis, and $\hat{b}$ the unit vector in the direction of the geomagnetic field.

The RDSs of the used setups provide measurements of E_x (east - west) and E_y (north - south). The angle of polarization in the horizontal plane for pure geomagnetic radiation, ϕ_G, is expected to be

$$\phi_G = \tan^{-1}\left(\frac{e_y^G}{e_x^G}\right) = \tan^{-1}\left(\frac{(\hat{d} \times \hat{b})_y}{(\hat{d} \times \hat{b})_x}\right), \tag{6.2}$$

which can be rewritten as

$$\phi_G = \tan^{-1}\left(\frac{\sin\phi_d \sin\theta_d \cos\theta_b - \cos\theta_d \sin\phi_b \sin\theta_b}{-\sin\theta_d \cos\phi_d \cos\theta_b + \cos\theta_d \sin\theta_b \cos\phi_b}\right), \tag{6.3}$$

in which ϕ_d and ϕ_b are respectively the azimuth angles (measured from east, positive to north) of the EAS axis and the geomagnetic field, while θ_d and θ_b are their zenith angles. The orientation of the geomagnetic field as a function of time in Malargüe can be found in section 4.8. In case of an RD-SD coincidence, the EAS axis is obtained from the reconstruction of the SD event. The uncertainty on ϕ_G is obtained by propagating the uncertainties on $\hat{d}$ and $\hat{b}$,

$$\begin{aligned}
\sigma_{\phi_G} &= \sqrt{\left(\frac{\partial\phi_G}{\partial e_x}\sigma_{e_x})^2 + (\frac{\partial\phi_G}{\partial e_y}\sigma_{e_y}\right)^2} \\
&= \sqrt{\left(\frac{1}{1+(e_y/e_x)^2}\right)^2\left(\left(\frac{\sigma_{e_x}e_y}{e_x^2}\right)^2 + \left(\frac{\sigma_{e_y}}{e_x}\right)^2\right)}, \qquad (6.4)
\end{aligned}$$

with

$$\begin{aligned}
\sigma_{e_x}^2 &= \left(\frac{\partial e_x}{\partial\theta_d}\sigma_{\theta_d}\right)^2 + \left(\frac{\partial e_x}{\partial\phi_d}\sigma_{\phi_d}\right)^2 + \left(\frac{\partial e_x}{\partial\theta_b}\sigma_{\theta_b}\right)^2 + \left(\frac{\partial e_x}{\partial\phi_b}\sigma_{\phi_b}\right)^2 \qquad (6.5) \\
\sigma_{e_y}^2 &= \left(\frac{\partial e_y}{\partial\theta_d}\sigma_{\theta_d}\right)^2 + \left(\frac{\partial e_y}{\partial\phi_d}\sigma_{\phi_d}\right)^2 + \left(\frac{\partial e_y}{\partial\theta_b}\sigma_{\theta_b}\right)^2 + \left(\frac{\partial e_y}{\partial\phi_b}\sigma_{\phi_b}\right)^2, \qquad (6.6)
\end{aligned}$$

in which

$$\begin{aligned}
\frac{\partial e_x}{\partial\theta_d} &= b_z\cos\theta_d\sin\phi_d + b_y\sin\theta_d \qquad (6.7) \\
\frac{\partial e_x}{\partial\phi_d} &= b_z\sin\theta_d\cos\phi_d \qquad (6.8) \\
\frac{\partial e_x}{\partial\theta_b} &= -d_y\sin\theta_b - d_z\cos\theta_b\sin\phi_b \qquad (6.9) \\
\frac{\partial e_x}{\partial\phi_b} &= -d_z\sin\theta_b\cos\phi_b, \qquad (6.10)
\end{aligned}$$

and

$$\begin{aligned}
\frac{\partial e_y}{\partial\theta_d} &= -b_z\cos\theta_d\cos\phi_d - b_x\sin\theta_d \qquad (6.11) \\
\frac{\partial e_y}{\partial\phi_d} &= b_z\sin\theta_d\sin\phi_d \qquad (6.12) \\
\frac{\partial e_y}{\partial\theta_b} &= +d_x\sin\theta_b + d_z\cos\theta_b\cos\phi_b \qquad (6.13) \\
\frac{\partial e_y}{\partial\phi_b} &= -d_z\sin\theta_b\sin\phi_b. \qquad (6.14)
\end{aligned}$$

The polarization angle, and the uncertainty on it, are extracted from the radio data using the Stokes parameters as described in section 5.6. The Stokes parameters are determined in a full width half maximum window as described in section 5.2.
In figure 6.1, the polarization angles as derived from the measurements are compared to the geomagnetic polarization angles obtained with equation (6.2). All figures are made with a cut of $\mathrm{SNR}_L > 2$ (equation (5.47)), and the possible influences by thunderstorms are indicated. A simple linear function, $\phi_p = A + B\phi_G$, is fit to the data, once for events where there is no indication of thunderstorms, and once for the combination of events with no indication of thunderstorm and no monitoring.
The data that was measured during thunderstorm conditions show extreme deviations from the general trend. This indicates that the polarization angle is strongly influenced by the presence of thunderstorms.

A combination of the data, for which the antenna alignment was measured (section 4.3) and which is flagged as "No thunder", is shown in figure 6.2. For each setup the correlation coefficient between geomagnetic and the measured polarization angle is calculated and listed in table 6.1.

Setup	No thunder	No thunder + no monitoring
BLS	0.91	0.78
MAXIMA 2010	0.58	0.69
MAXIMA 2011	0.84	0.78
AERA	0.94	0.94
Combined	0.88	0.83

Table 6.1: Correlation coefficients between ϕ_p and ϕ_G.

From the fit results and the correlation coefficients, it is clear that the geomagnetic and measured polarization angles are positively correlated. For a purely geomagnetic polarized signal, the fit parameter A should be compatible with 0, B with 1, and $\chi^2/d \approx 1$ (d = degrees of freedom). A deviation from $A \approx 0$ could arise from an incorrect assumption on the ori-

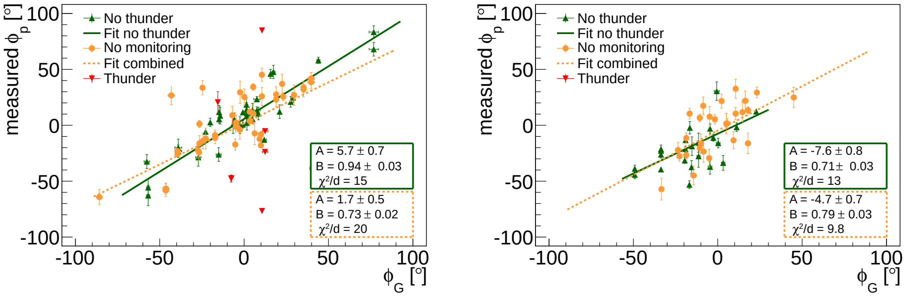

(a) BLS (b) MAXIMA 2010

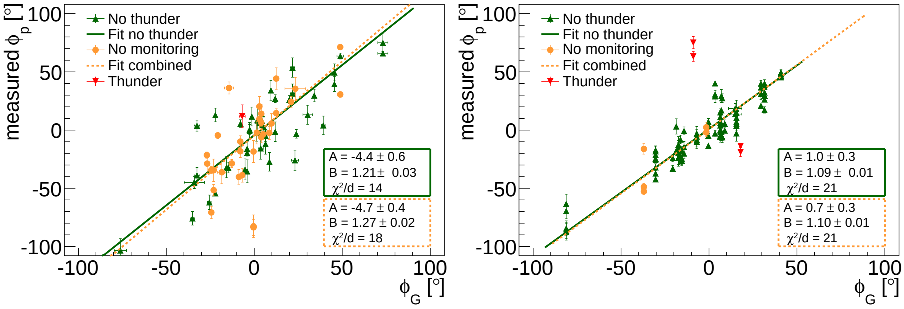

(c) MAXIMA 2011 (d) AERA

Figure 6.1: The predicted polarization angle for pure geomagnetic emission, ϕ_G, versus the measured polarization angle for the different setups. Different markers indicate the information from the thunderstorm monitoring system. The errors are calculated from equations (6.4) and (5.46). Note that the errors on ϕ_G are usually smaller than the marker size. A linear function, $\phi_p = A + B\phi_G$, is fitted to the data sets for which no indication of a thunderstorm was present, and to the combined data sets of having no monitoring and no indication of thunderstorms.

entation of the antennas. Since the antenna orientation from the BLS setup and the MAXIMA 2010 (before 20th of May 2010) were not measured a systematic offset cannot be excluded. However, the fit results indicate that

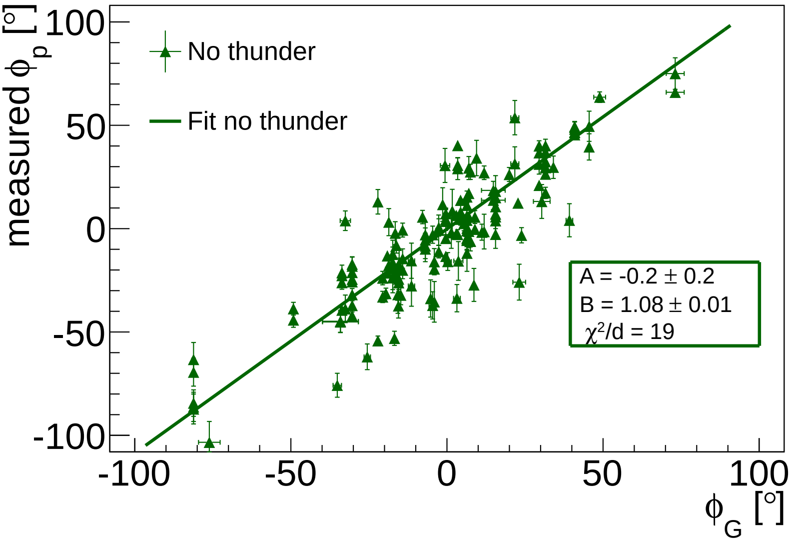

Figure 6.2: The predicted polarization angle for a pure geomagnetic emission versus the observed polarization angle for the combined data set. The combined data set consists of data that was measured with RDSs for which the antenna orientation was measured and which are not influenced by thunderstorms. A linear function, $\phi_p = A + B\phi_G$, is fit to the data, and the fit results are presented.

the data from all setups have systematic offsets. The values of parameter B and the χ^2/d are also not compatible with pure geomagnetic polarization. This indicates that although the geomagnetic polarization signature is clearly present in the data, it cannot fully explain the measured polarization angles.

6.2 Polarization signature of charge-excess radiation

In the previous section it was shown that polarization due to the geomagnetic emission cannot fully explain the observed polarization angles. In this section, we investigate whether the deviation from the pure geomagnetic polarization is radially inwards with respect to the EAS axis. Such a polarization is expected for a charge-excess contribution (section 2.4).

For a radially polarized electric field around the EAS axis, the polarization angle depends on the position of the RDS with respect to the EAS axis. When placing the EAS axis in the center of the coordinate system,

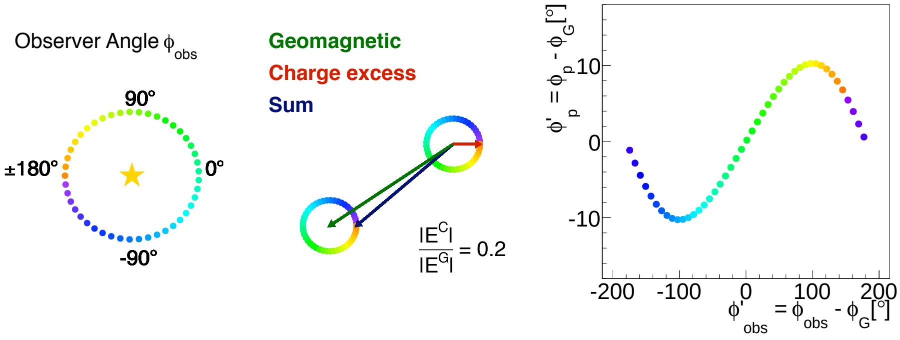

(a) (b) (c)

Figure 6.3: In (a) the color coding gives the observer angle, and the star shows the location of the shower axis. The interference of the geomagnetic and the charge-excess mechanisms is shown in (b) (with a relative strength of 0.2). The colored circles track the end point of the individual contribution and the sum as a function of observer angle. The electric field of the geomagnetic emission is independent of ϕ_{obs}. In (c) the polarization signature of the charge-excess contribution is shown for a relative strength of 0.2. The modified observer angle, ϕ'_{obs}, corrects for the phase shift of this pattern due the orientation of the geomagnetic component.

the observer angle, ϕ_{obs}, can be defined as the angle of the position of the RDS with respect to the east (positive towards north) as shown in the left panel of figure 6.3(a).

In figure 6.3(b), the influence of a charge-excess contribution to the total electric field as a function of the observer angle is shown. Since the orientation of the geomagnetic polarization depends on the direction of the shower axis, a modified observer angle is defined with respect to the geomagnetic polarization angle

$$\phi'_{\text{obs}} \equiv \phi_{\text{obs}} - \phi_G. \tag{6.15}$$

The deviation in polarization angle from a purely geomagnetic polarized signal is given by

$$\phi'_p = \phi_p - \phi_G. \tag{6.16}$$

in which ϕ_G is obtained using equation (6.2) and ϕ_p is calculated using equation (5.39). Using ϕ'_{obs}, the directional dependence of the geomagnetic contribution is taken out. If the strength of the charge-excess contribution with respect to the geomagnetic contribution would be constant, a polarization signature as shown in figure 6.3(c) is expected.

The polarization signature changes for different relative strengths of both contributions, this is illustrated in figure 6.4. For small fractions of $|E^C|/|E^G|$, the polarization signature has a sinusoidal pattern. For a larger relative fraction, the linear behavior extends to larger observer angles, after which there is a sharp drop.

To verify the charge-excess polarization signature, which is based on simple geometric arguments, ϕ'_p as a function of ϕ'_{obs} is plotted in figure 6.4(b) for the MGMR simulations of the MAXIMA 2010 RD - SD coincidences. Despite the richness of different shower parameters in this set of simulations, the polarization signature of the charge-excess is clearly present.

The MGMR simulations show some outliers to the general trend. These outliers are either at small distances to the shower axis ($< 50\,\text{m}$) or at large distances ($> 900\,\text{m}$). At small distances from the EAS axis, the geomagnetic component diverges in the MGMR simulations, and a cut-off parameter is introduced, which could influence the polarization angle. At large distances to the shower axis, the charge-excess contributions becomes dominant in

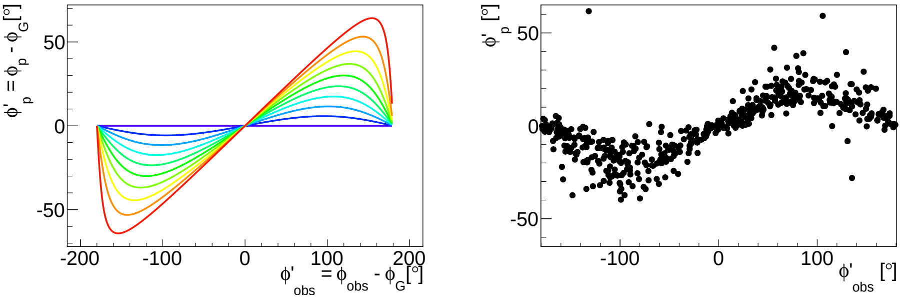

(a)

(b)

Figure 6.4: In (a) the polarization signature of a charge-excess contribution is shown as a function of the relative strength of both contributions. The relative strength is increased from 0 (violet) to 0.9 (red) in steps 0.1. In (b) charge-excess signature is shown for MGMR simulations.

the MGMR model [13], and the polarization signature presented in figure 6.4(a) no longer holds.

In figure 6.5, ϕ'_p as a function of ϕ'_{obs} is shown for the different setups. The same selection cuts are applied to the data as described in section 6.1. The uncertainties on ϕ'_{obs} are not displayed in figure 6.5 in order to keep the figures readable. Thunderstorm events are rejected, since it is clear from the results in section 6.1 that the polarization signature of these events is significantly influenced. The pattern that is expected for an inwards radial polarized contribution is present in all data sets. However, this pattern is not really strong in the BLS data set. A reason for this could be an offset in the antenna orientations and/or that the contamination induced by the trigger system is not negligible. Furthermore, there are some obvious outliers to the general pattern, even in the data sets for which there is no indication of thunderstorms. A reason for this can be that the position of the EAS axis is not reconstructed properly. Especially in the case of the BLS and both MAXIMA data sets, a large number of the coincidences with the SD are only measured in 3 tanks, and do not meet the recommended quality cuts of the SD reconstruction. Since the radial polarization depends on the

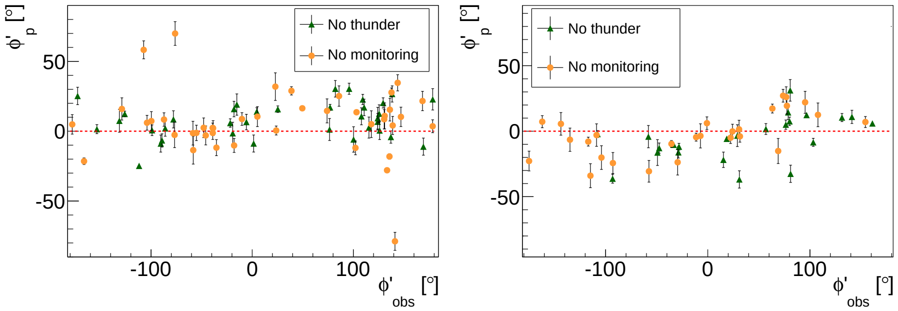

(a) BLS (b) MAXIMA 2010

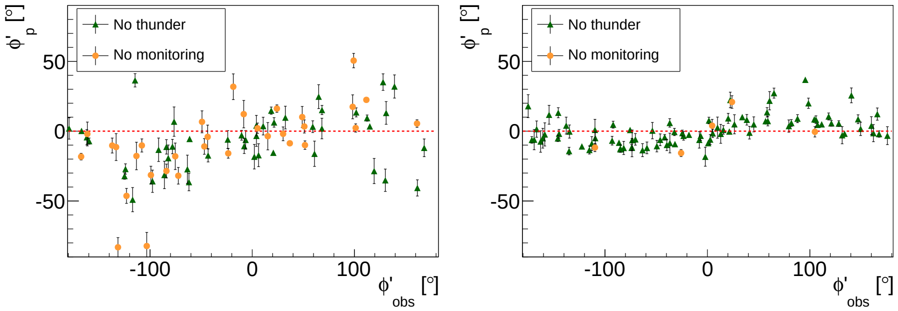

(c) MAXIMA 2011 (d) AERA

Figure 6.5: The modified polarization angle as a function of the modified observer angle. The different panels show the results for the different setups.

position of the antenna with respect to the EAS axis, a mis-reconstructed shower axis has consequences on the calculated ϕ'_{obs}.

Figure 6.6 shows the result of the combined data set with the same selection criteria as used in figure 6.2. The uncertainties on ϕ'_{obs} in this figure are estimated using

$$\sigma_{\phi_{obs}} \approx \sqrt{\frac{1}{1+\frac{Y^2}{X^2}}\left(\frac{\sigma_X^2 Y^2}{X^4}+\frac{\sigma_Y^2}{X^2}\right)}, \tag{6.17}$$

in which X (positive to east) and Y (positive to north) are the distances

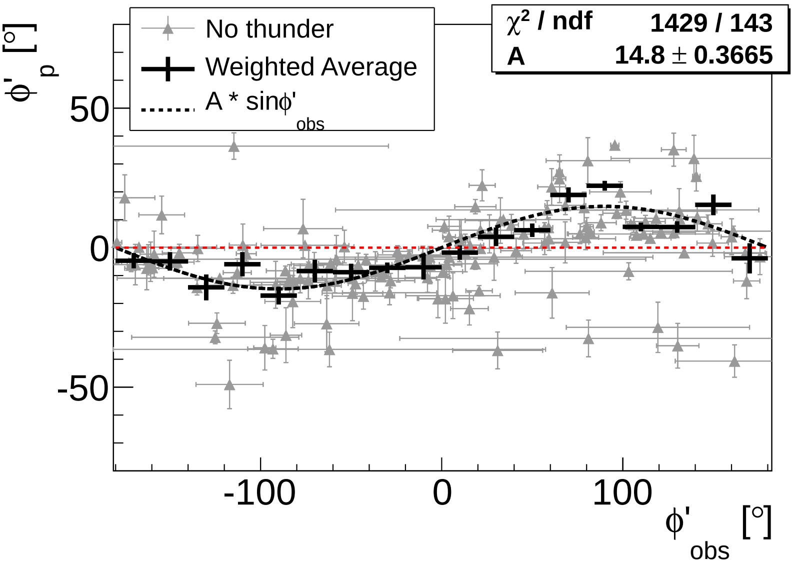

Figure 6.6: The ϕ'_p as a function of the $\phi'_{\rm obs}$, The combined data set consists of data where the monitoring system did gave an indication that there was no thunderstorm. In addition, the restriction is made that the antenna orientation was measured.

from the RDS on ground to the shower axis, σ_X and σ_Y are the uncertainties on the position of the shower axis as given by the SD-reconstruction. To clarify the pattern, a weighted average is calculated using bins of 20° in $\phi'_{\rm obs}$. The weight of an individual point is calculated as $1/(\sigma^2_{\phi'_{\rm obs}} + \sigma^2_{\phi'_p})$. To the unbinned data, a simple function $\phi'_p = A\sin(\phi'_{\rm obs})$ is fit. Although the high χ^2/d of this fit indicates that the fit function is not appropriate for this data, it still results in a significant amplitude indicating an oscillation as a function of $\phi'_{\rm obs}$.

6.3 Strength of the radial component

In the previous section it was shown that qualitatively the polarization signature of a charge-excess contribution is present in the data. In this section the strength of this radial component is estimated for each measurement.

6.3.1 Geometry and polarization angle

In the approximation that there is only a radial and a geomagnetic component, the total electric field can be written as

$$\vec{E} = \vec{E}^G + \vec{E}^C = |E^G|\vec{e}^{\,G} + |E^C|\vec{e}^{\,C}. \tag{6.18}$$

One dependency of the strength of E^G is well known

$$|E^G| \propto |\sin\alpha|, \tag{6.19}$$

where α is the angle between the geomagnetic field and the shower axis. The relative strength of a radial contribution with respect to the geomagnetic contribution is defined as

$$a \equiv \sin\alpha\frac{|E^C|}{|E^G|}, \tag{6.20}$$

in which the geomagnetic component is corrected for $\sin\alpha$.
The polarization angle ϕ_p describes the orientation of $\vec{E}$ with respect to east in the horizontal plane; it is defined to be positive towards north. Using both contributions to the electric field, the expected polarization angle of $\vec{E}$ is given by

$$\phi_p = \tan^{-1}\left(\frac{E_y}{E_x}\right) = \tan^{-1}\left(\frac{\sin(\phi_G) + \frac{a}{|\sin\alpha|}\sin(\phi_C)}{\cos(\phi_G) + \frac{a}{|\sin\alpha|}\cos(\phi_C)}\right), \tag{6.21}$$

in which ϕ_G is the azimuth angle of the geomagnetic contribution and ϕ_C is the azimuth angle of the charge-excess contribution.
The angle ϕ_C can be obtained from the location of the shower axis on

the ground as reconstructed by the SD $(X_{\mathrm{Core}}, Y_{\mathrm{Core}})$ with respect to the location of the RDS $(X_{\mathrm{RDS}}, Y_{\mathrm{RDS}})$

$$\phi_C = \tan^{-1}\left(\frac{Y_{\mathrm{Core}} - Y_{\mathrm{RDS}}}{X_{\mathrm{Core}} - X_{\mathrm{RDS}}}\right) = \tan^{-1}\left(\frac{Y}{X}\right), \tag{6.22}$$

in which the relative signs of X and Y have to be taken into account. The angle ϕ_G can be calculated using the direction of the shower axis obtained from the SD-reconstruction $\hat{d}_{\mathrm{SD}}$ and the direction of the geomagnetic field $\hat{b}$

$$\begin{aligned} \cos(\phi_G) &= (\hat{d}_{\mathrm{SD}} \times \hat{b})_x \\ &= \sin\theta_{\mathrm{SD}} \sin\phi_{\mathrm{SD}} \cos\theta_b - \sin\theta_b \sin\phi_b \cos\theta_{\mathrm{SD}} \qquad (6.23) \\ \sin(\phi_G) &= (\hat{d}_{\mathrm{SD}} \times \hat{b})_y \\ &= -\sin\theta_{\mathrm{SD}} \cos\phi_{\mathrm{SD}} \cos\theta_b + \sin\theta_b \cos\phi_b \cos\theta_{\mathrm{SD}}, \qquad (6.24) \end{aligned}$$

in which the $(\theta_{\mathrm{SD}}, \phi_{\mathrm{SD}})$ are the zenith and azimuth angle of the shower axis respectively. The angle between the shower axis and the geomagnetic field can be obtained using

$$\begin{aligned} \alpha &= \cos^{-1}(\hat{d}_{\mathrm{SD}} \cdot \hat{b}) \\ &= \cos^{-1}\big(\sin\theta_{\mathrm{SD}} \cos\phi_{\mathrm{SD}} \sin\theta_b \cos\phi_b \\ &+ \sin\theta_{\mathrm{SD}} \sin\phi_{\mathrm{SD}} \sin\theta_b \sin\phi_b + \cos\theta_{\mathrm{SD}} \cos\theta_b\big) \qquad (6.25) \end{aligned}$$

By using equations (6.20), (6.21) and (6.25), the polarization angle ϕ_p can be calculated for a given fraction a if the geometry of the event is known:

$$\phi_p(\theta_{\mathrm{SD}}, \phi_{\mathrm{SD}}, X, Y, \theta_b, \phi_b | a) = \phi_p(\vec{u}|a). \tag{6.26}$$

The vector $\vec{u} = \{\theta_{\mathrm{SD}}, \phi_{\mathrm{SD}}, X, Y, \theta_b, \phi_b\}$ is introduced to have a compact notation. Note that in a single event ϕ_C depends on the position of the RDS, while ϕ_G is the same for all RDSs.

The polarization angle in equation (6.26) can be compared to the measured polarization angle. The measured polarization angle can be obtained from the Stokes parameters as described in section 5.6.

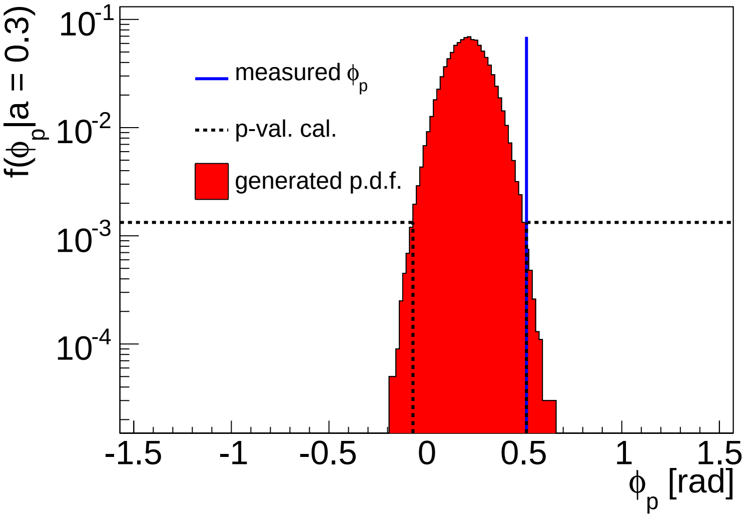

Figure 6.7: Example of the generated probability density function f for an $a = 0.3$ for event 11531810 station 11. It is generated by drawing 10^5 random samples using equation (6.27). Also the measured value of ϕ_p is displayed. The dotted horizontal line gives the value of f under which the p-value is calculated (eq. (6.28)).

6.3.2 Generating probability density functions

By assuming that the uncertainties on the parameters $\vec{u}$ are Gaussian distributed, and adding the uncertainty on the measured polarization angle σ_{ϕ_p}, a random realization i of ϕ_p (equation 6.26) can be drawn

$$\phi_p^i = \phi_p(\vec{u}^i|a) + \Delta_p^i. \qquad (6.27)$$

In which $\vec{u}^i$ is the vector containing random values drawn from normal distributions with mean values $\{\theta_{\mathrm{SD}}, \phi_{\mathrm{SD}}, X, Y, \theta_b, \phi_b\}$ and widths $\{\sigma_{\theta_{\mathrm{SD}}}, \sigma_{\phi_{\mathrm{SD}}}, \sigma_X, \sigma_Y, \sigma_{\theta_b}, \sigma_{\phi_b}\}$. In equation (6.27) Δ_p^i gives a random drawn value from a normal distribution with mean zero and width σ_{ϕ_p}. In equation (6.27) a is given by equation (6.20).

For $\sigma_{\theta_{\mathrm{SD}}}$ and $\sigma_{\phi_{\mathrm{SD}}}$ the uncertainties as given by the SD-reconstruction are used. It is assumed that the uncertainty on the reconstructed core position is much larger than the uncertainty on the positions of the RDSs and therefore we choose $\sigma_X = \sigma_{X,\mathrm{SD}}$ and $\sigma_Y = \sigma_{Y,\mathrm{SD}}$. The orientation of the magnetic field can be assumed to be constant (within its uncertainties) over the period the data was taken. Therefore, the direction of the geomagnetic field is fixed and given by $(\theta_b = 54.8°, \phi_b = 87.6°)$ with uncertainties of $(\sigma_{\theta_b} = 0.6°, \sigma_{\phi_b} = 0.3°)$ (see section 4.8).

By drawing many samples using equation (6.27), the probability density function f for a given value of a is generated $f(\phi_p|a)$. An example of a generated f is shown in figure 6.7. From f a p-value is obtained using

$$p(\phi_p|a) = \int_{f(\phi'_p)<f(\phi_p)} f(\phi'_p)d\phi'_p, \tag{6.28}$$

in which ϕ_p is the measured polarization angle. To take into account the periodicity of ϕ_p the integrals boundaries are chosen differently compared to a standard p-value calculation.

The p-value can be evaluated as a function of a. An example of this is given in figure 6.8. The maximum of $p(\phi_p|a)$ occurs at the most probable value of a for the measured ϕ_p. The (asymmetric) uncertainties on the most probable a are estimated by summing $p(\phi_p|a)$ from the most probably value in the direction of the next largest probable value until 68% of the total sum is reached.

For computational reasons, we decide to evaluate a in the range (-1,1). An value of $a = 1$ corresponds to a radial inwards polarized contribution of equal strength as the geomagnetic contribution, while $a = -1$ corresponds to a radial outwards polarized contribution of equal strength.

6.3.3 The relative strength of the radial component in individual measurements

In figure 6.9 the estimation of the most probable values of a are shown for the AERA data set. Only those measurements are shown for which there

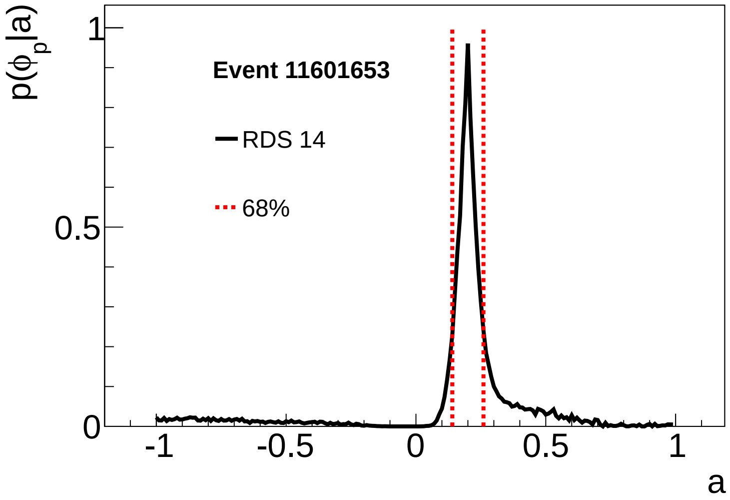

Figure 6.8: $p(\phi_p|a)$ in the range $-1 < a < 1$ for stations 14 in event 11601653. The estimated uncertainties on the most probable value of a are indicated with the dotted lines.

was no indication of thunderstorms and the monitoring system was on. Each individual measurement a_i of the most probable value of a has its own uncertainty. Therefore quantities derived for the whole sample need to be calculated using weights that take into account the uncertainty on individual measurements σ_i. The weighted mean $\bar{a}$ on the sample of n measurements is calculated using

$$\bar{a} = \frac{\sum_{i=1}^{n} w_i a_i}{\sum_{i=1}^{n} w_i}, \tag{6.29}$$

in which, in the case of symmetric uncertainties, the weight w_i is given by

$$w_i = \frac{1}{\sigma_i^2}. \tag{6.30}$$

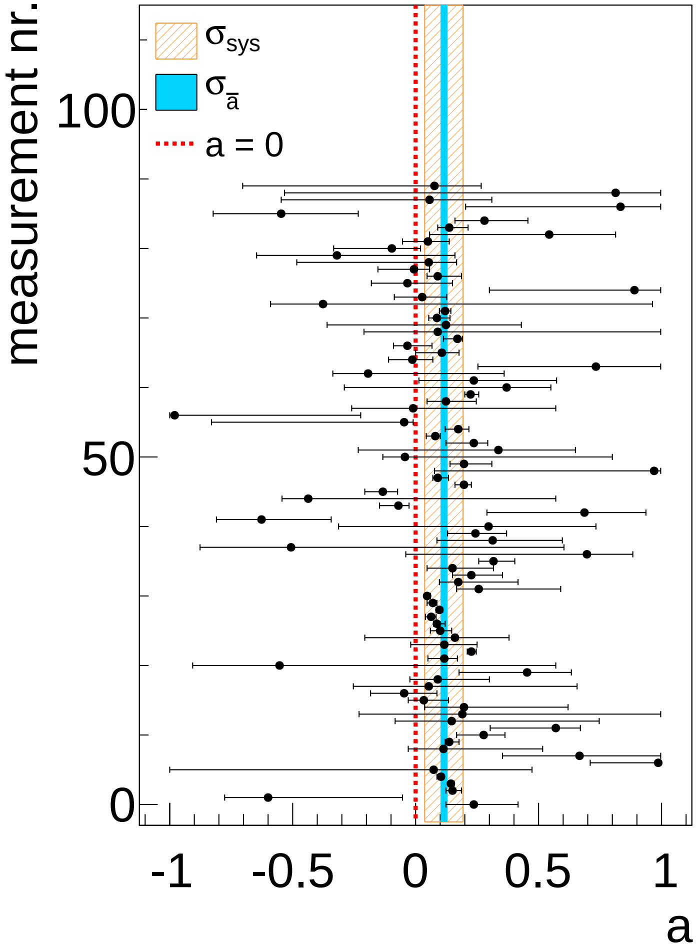

Figure 6.9: The estimation of the most probable values of a per measurement.

However, the uncertainty on an individual measurement is asymmetric. Therefore the uncertainty for calculating the weight is chosen in direction towards the mean,

$$\sigma_i = \begin{cases} \sigma_{h,i} & \text{if } a_i < \bar{a} \\ \sigma_{l,i} & \text{if } a_i > \bar{a}. \end{cases} \tag{6.31}$$

The uncertainty $\sigma_{h,i}$ is the higher bound on a_i, while $\sigma_{l,i}$ is the lower bound. When we decide which uncertainty to use, $\bar{a}$ needs to be known. This can be achieved by an iterative process which should converge to one value of $\bar{a}$. In the first iteration, the uncertainty to calculate the weight is chosen to be $\sigma_i = (\sigma_h + \sigma_l)/2$. In the following iteration(s) $\bar{a}$ is obtained using the weights of the previous iteration (equation (6.31)). Usually convergence is reached within four iterations, to be on the save side we decided to use twelve iterations.

There are two methods to obtain the uncertainty on $\bar{a}$, the first one is

$$\sigma_{\bar{a}} = \sigma_S = \frac{S}{\sqrt{n}} \tag{6.32}$$

in which S is the spread of the sample. The spread of the sample is estimated by a weighted root mean square

$$S = \sqrt{\frac{\sum_{i=1}^{n} w_i (a_i - \bar{a})^2}{\sum_{i=1}^{n} w_i}}. \tag{6.33}$$

A second estimation can be obtained using the weights:

$$\sigma_{\bar{a}} = \sigma_w = \frac{1}{\sqrt{\sum_{i=1}^{n} w_i}}. \tag{6.34}$$

If spread S on the sample is only due to the uncertainties on the measurements σ_i, then $\sigma_S = \sigma_w$. However if $\sigma_w > \sigma_S$, it is an indication that the uncertainties on the measurements are overestimated. In the case that $\sigma_w < \sigma_S$ either the uncertainties on the measurements are underestimated or there is additional spread due to an underlying distribution

For the data displayed in figure 6.9 we find that $\sigma_w < \sigma_S$. The additional spread due to an underlying distribution can be obtained by adding a systematic uncertainty σ_{sys} to the individual measurement uncertainties

$$\sigma_i' = \sqrt{\sigma_i^2 + \sigma_{sys}^2}. \tag{6.35}$$

The weights (equation (6.31)) can be recalculated using σ_i'. The σ_{sys} that results in $\sigma_w = \sigma_S$ gives the estimation of the spread due to the underlying distribution (or average underestimation of σ_i) and the correct value for $\sigma_{\bar{a}}$. An example to illustrate this method, using pseudo experiments, is shown in Appendix A.

For the measurements shown in figure 6.9 the mean value is calculated to be $\bar{a} = 0.115$ and the uncertainty on it is $\sigma_{\bar{a}} = 0.014$. The estimation for the systematic uncertainty is $\sigma_{sys} = 0.078$, as shown in Appendix A. The σ_{sys} is taken into account while calculating $\bar{a}$ and $\sigma_{\bar{a}}$ by replacing the uncertainty per measurement σ_i by σ_i'. In the case that the polarization of the radio signal was purely due to the geomagnetic effect the value $\bar{a}$ should be in agreement with 0. This hypothesis can be excluded with 8.2σ significance.

In table 6.2 the results are presented for the individual setups. The AERA data set gives by far the most accurate result, although the data from all setups are in agreement. For the BLS data, the additional uncertainty due to the unknown antenna orientation is not taken into account.

	$\bar{a}$	$\sigma_{\bar{a}}$
BLS	0.121	0.040
MAXIMA 2010	0.066	0.062
MAXIMA 2011	0.127	0.049
AERA	0.115	0.014

Table 6.2: The average relative strength $\bar{a}$ and the uncertainty on it $\sigma_{\bar{a}}$ for each of the data sets.

In table 6.3 the estimation of the additional spread on the relative strength is given. The larger systematic uncertainties in the BLS, MAXIMA 2010, and MAXIMA 2011 data might be due to the SD reconstruction quality.

	σ_{sys}
BLS	0.177
MAXIMA 2010	0.228
MAXIMA 2011	0.265
AERA	0.078

Table 6.3: The estimated systematic uncertainty per measurement, σ_{sys} for the different data sets.

The events measured at the AERA site are measured with the denser infill array leading to a higher SD tank multiplicity per event. Note that σ_{sys} is taken into account according to equation (6.35) while calculating $\bar{a}$ and $\sigma_{\bar{a}}$ in table 6.2.

6.4 Dependencies on EAS parameters

Disentangling the emission mechanisms using the polarization angle becomes impossible when the polarization directions due to both effects are aligned. This becomes visible as large uncertainties on the most probable value of a. This is illustrated in figure 6.10 in which a is displayed as a function of $\cos(\phi_G - \phi_C)$.

In the cases when both effects are almost parallel ($\cos(\phi_G - \phi_C) \approx 1$ or $\cos(\phi_G - \phi_C) \approx -1$), the uncertainties on a become large. In these cases the most probable values of a can end up near (or on) the boundaries in the chosen interval $-1 < a < 1$, which influences the reliability of the parameters that are estimated on the sample. To investigate this further, the influence of a cut on $|\cos(\phi_G - \phi_C)|$ is shown in figure 6.11.

The cut on $|\cos(\phi_{\text{obs}} - \phi_{\text{G}})|$ does not influence $\bar{a}$ significantly. However, the significance ($\bar{a}/\sigma_{\bar{a}}$) of the sample is influenced by the cut. It increases until $|\cos(\phi_{\text{obs}} - \phi_{\text{G}})| \approx 0.6$. For a looser cut, this value stays rather constant. The estimated systematic uncertainty decreases with an increasing number of measurements until the cut reaches a value of $|\cos(\phi_{\text{obs}} - \phi_{\text{G}})| < 0.6$. After this value, the systematic uncertainty increases again. These obser-

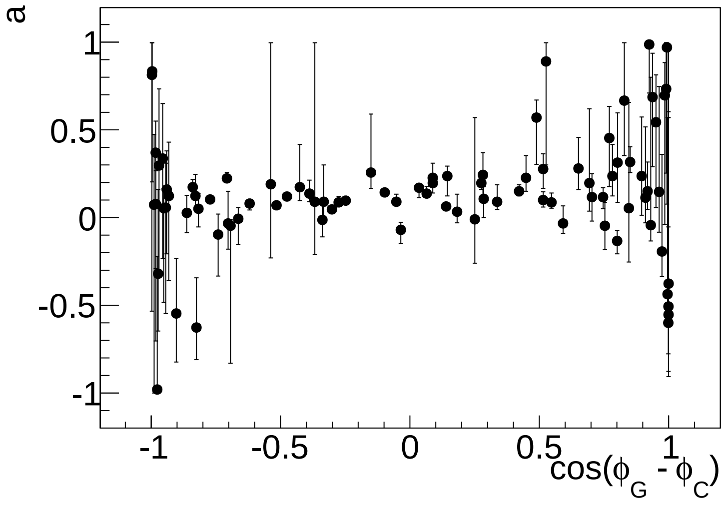

Figure 6.10: The most probable value of a as a function of $\cos(\phi_G - \phi_C)$.

vations indicate that the method presented in this section is most sensitive below $|\cos(\phi_{\mathrm{obs}} - \phi_{\mathrm{G}})| = 0.6$.

Figure 6.12 shows a for measurements for which $|\cos(\phi_{\mathrm{obs}} - \phi_{\mathrm{G}})| \leq 0.6$. The mean on this sample is $\bar{a} = 0.119 \pm 0.013$. The uncertainty introduced to estimate the additional spread on each measurement in this sample is $\sigma_{sys} = 0.054$. This value of σ_{sys} is reduced significantly with respect to the full sample. Note that σ_{sys} is taken into account while calculating $\bar{a}$ and $\sigma_{\bar{a}}$.

In figure 6.13, the correlations of a with the geometry and the energy of the EAS are shown. This figure is produced using the cut $|\cos(\phi_{\mathrm{obs}}-\phi_{\mathrm{G}})| \leq 0.6$. There is a rather strong correlation with respect to the zenith angle, while for the other parameters the correlation is low.

In figure 6.13(a) the correlation between a and the zenith angle is fitted with a linear function. This function can be used to remove the dependency of a on the zenith angle. Therefore we introduce a_{38} which is the

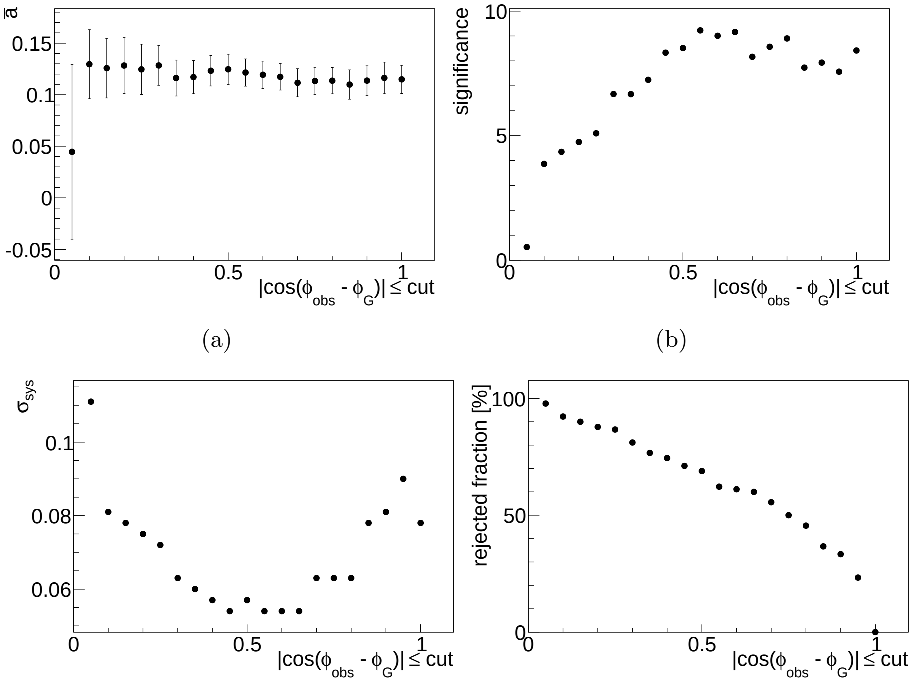

(a)

(b)

(c)

(d)

Figure 6.11: The influence of a cut on $|\cos(\phi_{\text{obs}} - \phi_{\text{G}})|$. Panel (a) shows the influence of the cut on the estimation of $\bar{a}$, while (b) shows the influence on the significance $\bar{a}/\sigma_{\bar{a}}$. The estimated systematic uncertainty as a function of the cut is shown in panel (c). The percentage of events that are rejected as a function of the cut is shown in (d).

value of a corrected by the linear fit to a at 38°. Figure 6.14 shows a_{38} for measurements with $|\cos(\phi_{\text{obs}} - \phi_{\text{G}})| \leq 0.6$. The mean on this sample is: $\bar{a}_{38} = 0.139 \pm 0.010$. The uncertainty introduced to estimated the additional spread per point on this sample is $\sigma_{sys} = 0.030$. The value of σ_{sys} is reduced, which indicates that most (0.044) of the additional spread originates from a zenith angle dependence of a. Note again that σ_{sys} is taken

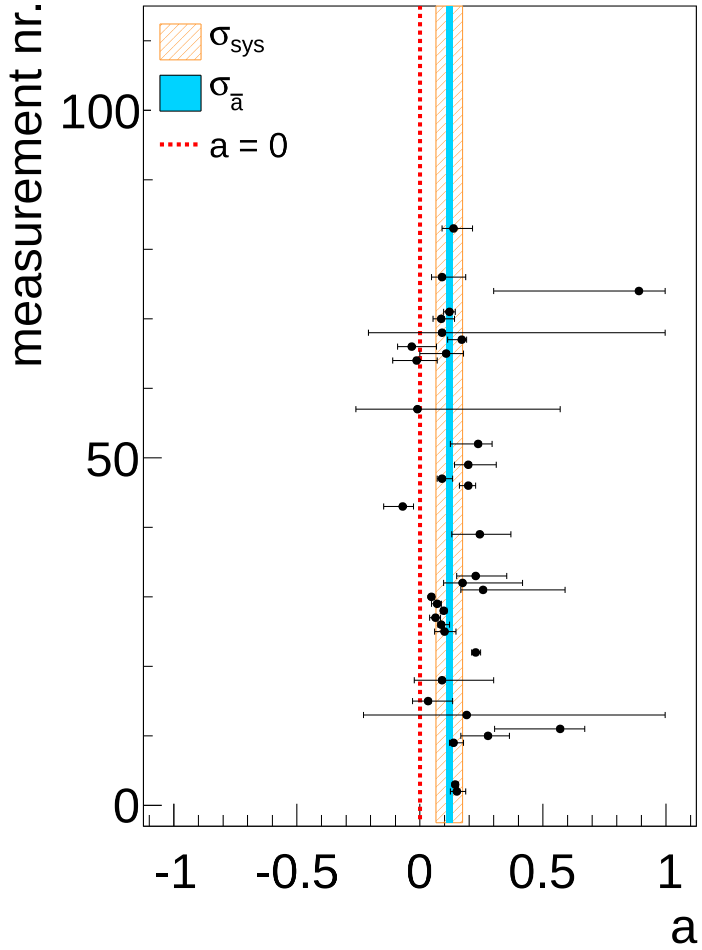

Figure 6.12: The estimation of the most probable values of a for measurements for which $|\cos(\phi_{\mathrm{obs}} - \phi_{\mathrm{G}})| \leq 0.6$.

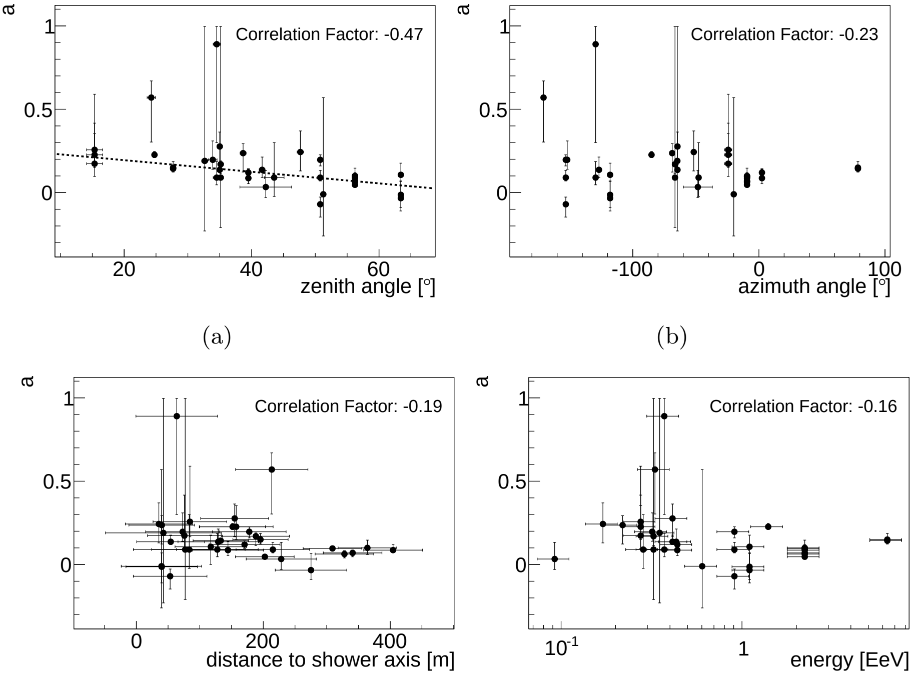

(a) (b)

(c) (d)

Figure 6.13: Correlation of a with shower parameters. In (a) the correlation with the zenith angle is shown. This correlation is fit with a simple linear function indicated by the dotted line. The fit results are $a = 0.27 - 0.0035\theta$, with θ the zenith angle. In (b) the correlation with the azimuth angle is shown. In (c) the correlation with the distance to the shower axis is shown. In (d) the correlation with the energy is shown.

into account while calculating $\bar{a}$ and $\sigma_{\bar{a}}$.

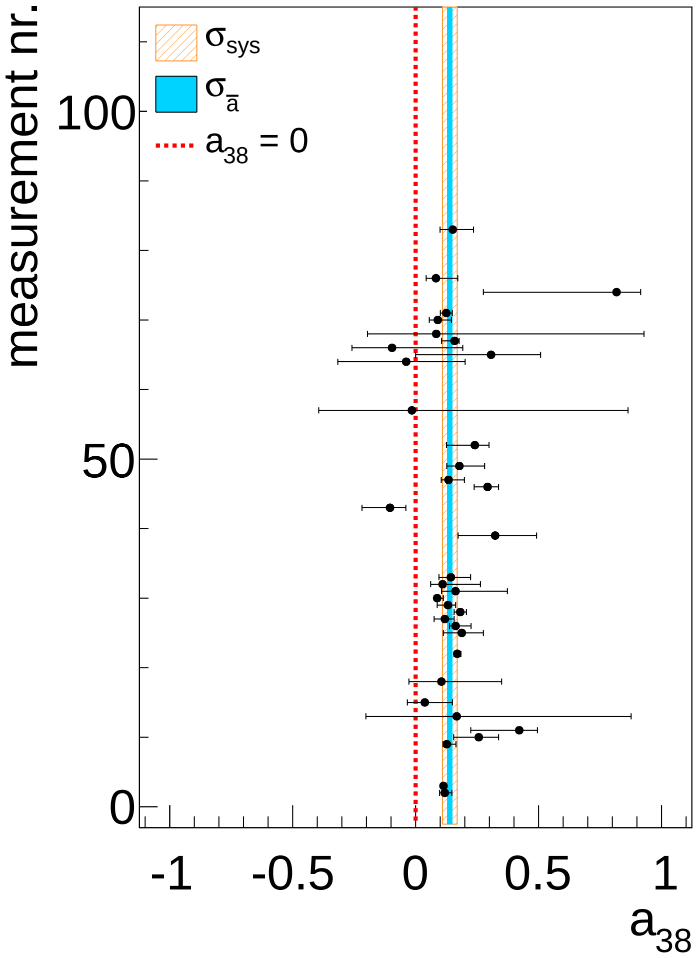

Figure 6.14: The estimation of the most probable values of a_{38} for measurements for which $|\cos(\phi_{\text{obs}} - \phi_{\text{G}})| \leq 0.6$.

6.4.1 Simulations

To investigate the known dependencies of a with EAS parameters, MGMR-simulations are analyzed qualitatively. These simulations are generated from the EAS parameters obtained from the SD-reconstruction of the RD-SD coincidences of the MAXIMA 2010 data (section 4.6). In this section only the simulations generated from the true SD values are used. The simulations are bandpass filtered between 30-80 MHz to match, more or less, the frequency band of the RDSs.

Since the true parameters that have been used to generate the simulations are known, no uncertainties have to be taken into account. By rewriting equation (6.21), the value of a can be obtained directly when the polarization angle is known

$$a = \sin(\alpha)\frac{|E^C|}{|E^G|} = \sin(\alpha)\frac{\sin\phi_G - \tan\phi_p\cos\phi_G}{\tan\phi_p\cos\phi_C - \sin\phi_C}. \tag{6.36}$$

The polarization angle is obtained by calculating the Stokes parameters on a full width half maximum window (similar to the measurements). No noise is added to the simulations, therefore no uncertainty is assigned to the obtained ϕ_p.

The correlations of a with respect to the EAS parameters are presented in figure 6.15. A negative correlation with the zenith angle is present in the simulation. However, this correlation is weaker than the one observed in the data. The distance to shower axis shows a positive correlation with a. The azimuth angle shows a low correlation, while the correlation with the energy is negligible.

The geomagnetic contribution is expected to be polarized perpendicular to the shower axis. However the charge-excess contribution has a component along the shower axis. If this component is significant, it will contribute to the charge-excess signal in the horizontal plane for non-vertical showers. Therefore, the angular dependencies could arise from an unfortunate choice of coordinates. To resolve this issue, all calculations are redone in the plane perpendicular to the shower axis (the shower plane). Therefore, any dependencies related to the charge-excess component along the shower

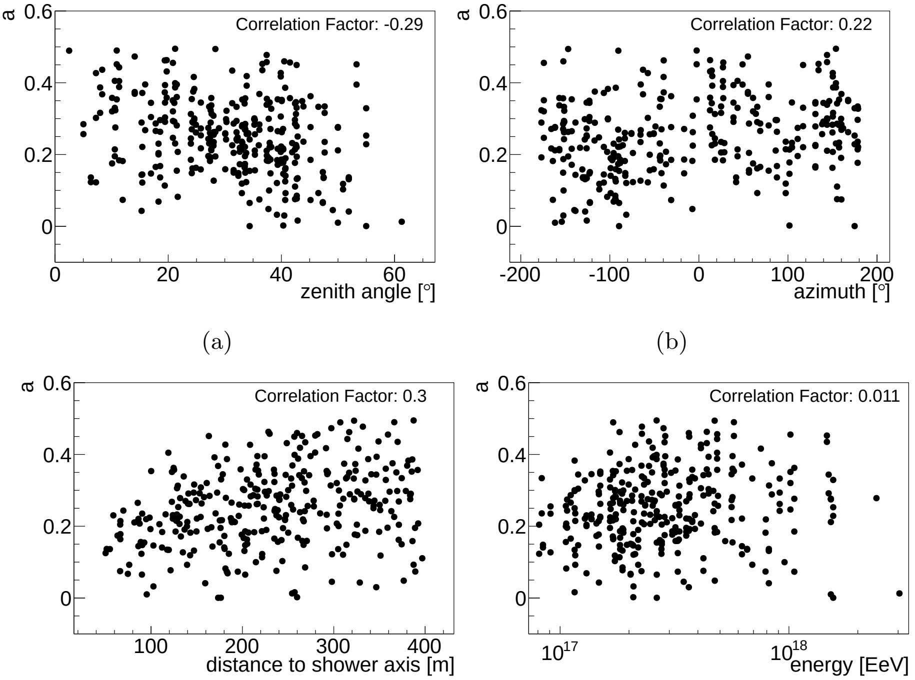

(a) (b)

(c) (d)

Figure 6.15: Correlation of a with shower parameters from MGMR simulations. In (a) the correlation with the zenith angle is shown. In (b) the correlation with the azimuth angle is shown. In (c) the correlation with the distance to the shower axis is shown. In (d) the correlation with the energy is shown.

axis should disappear. This change of coordinate system means that the polarization angle, the observer angle, and the orientation of the Lorentz force are recalculated in the shower plane. The resulting dependencies of a are shown in figure 6.16.

The dependencies on the distance to shower axis and zenith angle didn't disappear, in fact they become more prominent. Therefore, it is unlikely

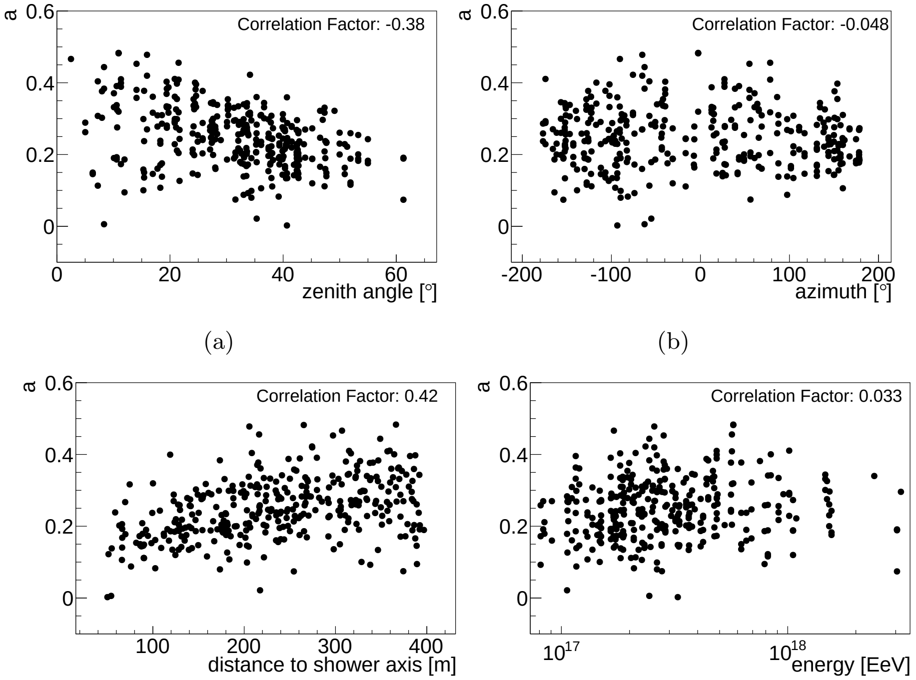

(a) (b)

(c) (d)

Figure 6.16: Correlation of a, calculated in shower plane coordinates, with shower parameters. In (a) the correlation with the zenith angle is shown. In (b) the correlation with the azimuth angle is shown. In (c) the correlation with the distance to the shower axis is shown. In (d) the correlation with the energy is shown.

that the zenith angle dependency in data arises from the fact that the calculations were performed in the horizontal coordinate system.

6.5 One-to-one comparison to MGMR simulations

For the measurements of the MAXIMA 2010 data set that have $\mathrm{SNR}_L > 2$ (equation (5.47)), the polarization angle and its uncertainty are determined. The set of measurements, that were not measured during thunderstorms, is compared to MGMR simulations (section 4.6) generated from the SD reconstructed event. A similar analysis on this data set, based on a slightly different parameterization, can be found in [43].
According to the uncertainties on the SD reconstruction, an additional 100 simulations were generated. These additional simulations are used to propagate the influence of the uncertainty on SD-parameters to the polarization angle.
From the 100 simulations per measurement, the most probable polarization angle is estimated in the following way:

- The polarization angles, $\phi_{p,i}$, are sorted by their value.
- From these sorted angles, the median polarization angle is selected. Starting from this median, subsequently the polarization angle is selected that is nearest to the set that is already selected. This iterative procedure is continued until 68% of all 100 simulations are selected.
- On this 68% selection a new median is determined, which gives the estimation of the most probable polarization angle $\phi_{p,\mathrm{sim}}$. To $\phi_{p,\mathrm{sim}}$ high and low uncertainties are assigned by taking the values at the edge of the 68% selection: $\sigma_{h,\mathrm{sim}} = \phi_{p,\mathrm{high}} - \phi_{p,\mathrm{sim}}$ and $\sigma_{l,\mathrm{sim}} = -\phi_{p,\mathrm{low}} + \phi_{p,\mathrm{sim}}$.

These three steps are illustrated below by a simple example on 15 simulations:

$$\begin{aligned}
\vec{\phi}_p &= [18, 21, 14, 24, 26, 14, -7, 28, 20, 9, 23, 10, 29, 23, 11] \\
\vec{\phi}_p &= [-7, 9, 10, 11, 14, 14, 18, 20, 21, 23, 23, 24, 26, 28, 29] \\
\vec{\phi}_p &= [-7, 9, 10, 11, 14, \mathit{14}, \mathit{18}, \mathit{20}, \mathit{21}, \mathit{23}, \mathbf{23}, \mathit{24}, \mathit{26}, \mathit{28}, \mathit{29}]
\end{aligned}$$

The bold blue number in the last step gives the estimation of $\phi_{p,\mathrm{sim}}$, while the italic red numbers shows the region between $\phi_{p,\mathrm{sim}} - \sigma_{l,\mathrm{sim}}$ and $\phi_{p,\mathrm{sim}} + \sigma_{h,\mathrm{sim}}$.

The deviation from the geomagnetic polarization angle, $\phi'_p = \phi_p - \phi_G$, as a function of the modified observer angle, $\phi'_{\mathrm{obs}} = \phi_{\mathrm{obs}} - \phi_G$, is shown in figure 6.17 for simulations and measurements. This is shown once for the MGMR simulations that contain a charge-excess contribution, and once for the simulations without a charge-excess contribution. From figure 6.17, it is clear that the polarization angle for the simulations without a charge-excess contribution hardly deviate from the geomagnetic polarization angle.

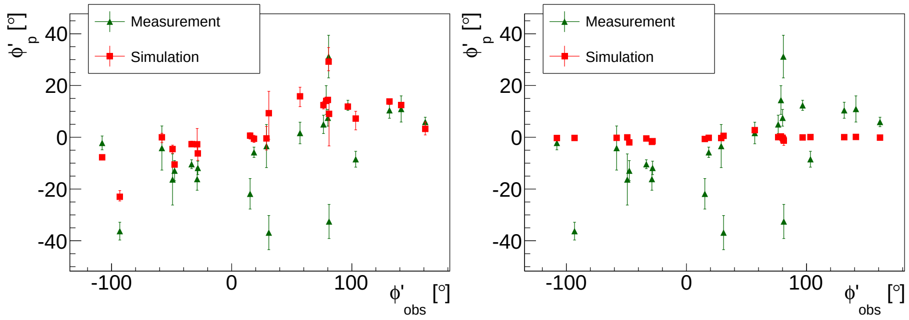

(a) (b)

Figure 6.17: Comparison of the polarization signature of a charge-excess contribution between measurements and the corresponding simulations. In (a) the simulations with charge-excess contribution are shown, while (b) shows simulations without a charge-excess contribution.

To investigate the agreement between measurement and simulation, it is more convenient to plot ϕ'_p of the measurements against the ϕ'_p from simulations as shown in figure 6.18. To get a measure of the agreement between simulation and measurement a χ^2_i value is calculated for each measurement i

$$\chi^2_i = \frac{(\phi'_{p,\mathrm{sim}} - \phi'_{p,\mathrm{meas}})^2}{\sigma^2_{(h,l),\mathrm{sim}} + \sigma^2_{\mathrm{meas.}}}. \tag{6.37}$$

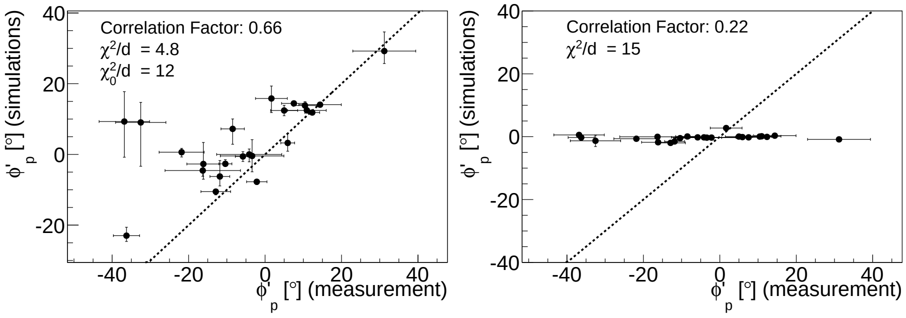

(a) (b)

Figure 6.18: Comparison of the deviation from the geomagnetic polarization angle between data and simulation. In (a) the charge-excess contribution is included in the simulations, while in (b) no charge-excess contributions is included. The definition of χ^2/d and χ_0^2/d are given by equation (6.38) and (6.39). The dotted line indicates a one-to- one correlation.

If $\phi'_{p,\mathrm{sim}} > \phi'_{p,\mathrm{meas}}$ then the lower uncertainty $\sigma_{l,\mathrm{sim}}$ on the simulations is used, while $\sigma_{h,\mathrm{sim}}$ is used when $\phi'_{p,\mathrm{sim}} < \phi'_{p,\mathrm{meas}}$. To get a measure of the agreement between simulation and measurement over the whole sample we calculate

$$\chi^2/d = \sum_{i=1}^{d} \frac{\chi_i^2}{d}, \tag{6.38}$$

in which d denotes the number of degrees of freedom, which corresponds to the number of measurements in the sample. The values of χ^2/d, are given in figure 6.18.

The charge-excess contribution depends on the location of the shower core. Hence, the uncertainty propagated from the SD-parameters will increase when charge excess is included in the simulations. Therefore, the value of the χ^2/d will be reduced. However, this doesn't necessary imply that the reduced χ^2/d is due to a correct implementation of the charge-excess in the simulations. There are two approaches to test wether the simulations with charge-excess agree better with measurements than simulations without.

The first one is to check wether the correlation, not taking into account the uncertainties, actually increases. This is indeed the case, as shown in figure 6.18. A second approach is to calculate the χ^2/d with uncertainties from simulations with charge excess, but with values ϕ'_p of simulations without charge excess:

$$\chi_0^2/d = \frac{(\phi'_{p,\mathrm{NoChx}} - \phi'_{p,\mathrm{meas}})^2}{\sigma^2_{(h,l),\mathrm{sim}} + \sigma^2_{\mathrm{meas.}}} \approx \frac{(\phi'_{p,\mathrm{meas}})^2}{\sigma^2_{(h,l),\mathrm{sim}} + \sigma^2_{\mathrm{meas.}}} \tag{6.39}$$

If the χ_0^2/d is larger than the χ^2/d for simulations with charge-excess, it is an indication that including charge-excess indeed results in better agreement between measurement and simulations. The value of χ_0^2/d is shown in figure 6.18.

To assign a probability that simulations and measurements are in agreement, the probability density function (pdf) of χ^2/d needs to be known. Since χ^2/d is obtained from values with asymmetric uncertainties, the standard χ^2-pdf cannot be used. However, by performing a set of pseudo experiments the pdf can be simulated:

- For each measurement, a randomly drawn simulation is selected from the 100 simulations per measurement. This simulation will function as a pseudo-measurement.

- To the polarization angle of this pseudo-measurement, a random value, drawn from a Gaussian probability function with a width equal to the uncertainty on the real measurement, is added. The uncertainty assigned to the pseudo-measurement, is the uncertainty on the polarization angle from the real measurement.

- All the pseudo-measurements form one pseudo-experiment. From this pseudo-experiment, a χ^2/d can be obtained.

By generating many pseudo-experiment, a probability density function of χ^2/d is simulated. The pdf's for simulations with and without charge excess are shown in figure 6.19. In total 10000 pseudo-experiments are performed

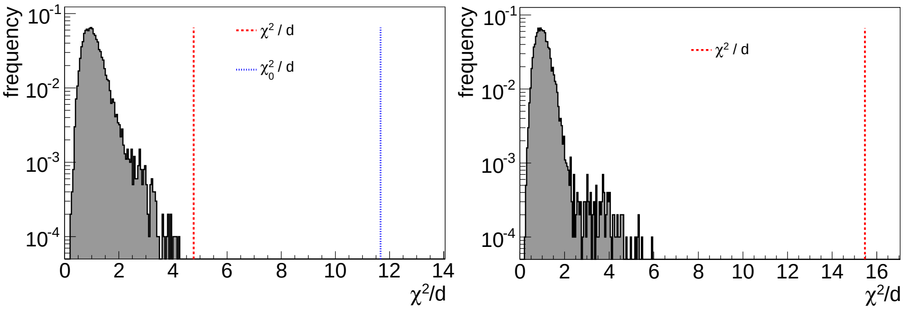

(a)

(b)

Figure 6.19: Simulated probability density functions of χ^2/d for simulations with (a) and without(b) a charge-excess contribution.

to generate these pdf's. From figure 6.19 a p-value could be obtained. The p-value is the probability of obtaining a χ^2/d, from the pseudo-experiments which is at least as extreme as the ones observed from the measurements. In our case, all our values of χ^2/d are so large that no pseudo-experiment resulted in such a χ^2/d, therefore only an upper limit on the p-value is obtained, p-value $< 10^{-4}$. The study presented in [43] gave similar results.

Chapter 7

Discussion and Conclusion

In this chapter, the results obtained from studying the polarization of radio emission from EASs is discussed. In section 6.1, it is shown which polarization angle from geomagnetic radiation is expected. This expectation is compared to the polarization angle obtained from the measurements of three setups. In data from all three setups a positive correlation is found between measurement and geomagnetic expectation. Fitting a linear function indicates that the correlation is close to a one-to-one correlation. This confirms the contribution of the geomagnetic emission to the observed radio pulses. However, at the same time, the fit results indicate that the geomagnetic emission alone does not explain the observed polarization angles.

In [40], large amplitudes of the radio emission from EAS were reported during thunderstorms. In section 6.1, it is shown that the polarization angles also show large deviations from the geomagnetic expectation during thunderstorm conditions. Therefore, these events should be rejected during standard polarization studies. However, studying the polarization of these measurements could lead to better understanding of the radio emission processes during thunderstorms.

In section 6.2, the influence of a radially polarized charge-excess contribution on the polarization angle is explained. The deviation it causes from the geomagnetic polarization angle is periodic with the observer angle. This typical polarization signature is visible in the measurements from all three setups. This gives a qualitative confirmation that the polarization signature of a charge-excess contribution is present in the measurements.

In section 6.3, the relative strength, a, of a radial contribution with respect to the geomagnetic contribution is estimated. This relative strength is estimated in the horizontal plane. A method is presented to estimate this strength, and its uncertainty for each individual measurement. The results on the individual AERA measurements are presented in section 6.3.3. The average relative strength in the AERA measurements is $\bar{a} = 0.115 \pm 0.014$. This shows that there is a significant (8.2σ) contribution that is polarized radially towards the shower axis, as expected for a charge-excess contribution. The results obtained from the other data sets are in agreement with the measurement from AERA, but are less accurate.

The uncertainties on the individual measurements of a are not sufficient to explain the observed spread on the whole data set. A systematic uncertainty per measurement is estimated from the measurements to explain the additional spread. For the AERA measurements a value of $\sigma_{sys} = 0.078$ was found. The additional spread can be due to an inaccurate SD-reconstruction or/and due to unknown dependencies of the relative strength on EAS parameters. Note that this systematic uncertainty is taken into account in the quoted accuracy of $\bar{a}$.

In the BLS and MAXIMA data set, the systematic uncertainty is larger than at AERA. A possible explanation for this is the difference in quality of the SD reconstruction. The water-tank multiplicity of the EAS recorded by the SD in the vicinity of the BLS is low (typically 3 or 4 tanks). Therefore, the influence of the additional off-grid water tank *Olaia* is significant, which may introduce biases in the SD reconstruction [44]. Many of these events do not fulfill the criteria of the standard SD-reconstruction. AERA, on the other hand, is co-located with AMIGA, which results in higher tank multiplicity (typically $\sim$8) per recorded SD event.

For the AERA measurements, the dependency of the relative strength on EAS parameters is studied (see section 6.4). When the polarization of the radial contribution aligns with the geomagnetic contribution, it becomes impossible using the methods in this thesis to calculate the relative strength. Therefore, the sensitivity of the relative strength depends on the angle between both contributions. When the angle between both effects decreases, the method starts to become less sensitive. As a result, the uncertainty stops decreasing when including measurements with a large value of $|\cos(\phi_G - \phi_C)|$. These measurement do not influence the mean value of a significantly, but they have an influence on the σ_{sys}. This is mainly due to the fact that we limit ourselves to the range $-1 \leq a \leq 1$, therefore underestimating the uncertainties on the measurements when $|\cos(\phi_G - \phi_C)| \approx 1$. When introducing the cut $|\cos(\phi_G - \phi_C)| \leq 0.6$ we obtain

$$\bar{a} = 0.119 \pm 0.013,$$

and the systematic uncertainty is reduced to $\sigma_{sys} = 0.054$.

The relative strength of the AERA measurements shows a rather strong, negative, correlation with the zenith angle. The energy of the EAS, the distance to the shower axis, and the azimuth angle show a rather low correlation with the relative strength. If we fit the zenith angle dependence with a simple linear function, and correct the relative strength to a zenith angle of 38°, we obtain

$$\bar{a}_{38} = 0.139 \pm 0.010$$

The systematic uncertainty is further reduced to $\sigma_{sys} = 0.030$, indicating that a large part of the original additional spread is due to a dependence of a on the zenith angle.

In section 6.4.1, the dependencies of the relative strength on shower parameters are investigated qualitatively in MGMR simulations. In these simulations a negative correlation between the relative strength and the zenith angle is observed. However, this correlation is weaker than the one observed in the measurements. In addition, there is a correlation between the relative strength and the distance to the shower axis, which is not observed in the measurements. A smaller correlation with the azimuth angle is observed in simulations, while the correlation with the energy is really low. The correlation with zenith and azimuth angle might be due to the charge-excess component in the direction of the shower axis. To investigate this hypothesis, all calculations were repeated in the coordinate system perpendicular to the shower axis. This results in an enhanced correlation with the zenith angle and the distance to shower axis. Therefore, it is concluded that correlation of the relative strength with the zenith angle cannot be explained by the component of the charge-excess contribution along the shower axis. To fully understand the dependencies of the relative strength on EAS-parameters more studies are needed.

Using the measurements from the MAXIMA 2010 data set, a one-to-one comparison is performed with simulations (section 6.5). The agreement, and correlation, between measurements and simulations improves when charge-excess is included in the simulations. However, the overall agreement between measurement and simulation remains rather poor even when charge-excess is included. The reasons for this can be twofold: the simulations are inaccurate, or the parameters obtained from the SD reconstruction are not reliable. From the current data set, it is hard to draw a conclusion. To get a more fair comparison between measurement and simulation, events measured at AERA should be compared to simulations. Since the simulations used in this thesis do not include Cherenkov effects (refractive index > 1), it might be interesting to compare measurements to simulations including this physics. Especially to understand the dependence of the relative strength on the geometry of the event Cherenkov effects might be crucial.

From this thesis we conclude that in addition to the geomagnetic emission mechanism, a radially inwards polarized contribution is measured. A contribution with such a polarization was already predicted by Askaryan 50 years ago [3]. A similar observation, like the one presented in this thesis, was performed by Hough and Prescott in 1970[45]. Although their setup was quite different, they came to the similar conclusion that the charge-excess emission contributes on average about 15% to the total signal. Recently, at higher frequencies and in denser media, the prediction from Askaryan has been confirmed at the SLAC Final Focuss Test Beam in 2000[46]

The interference of both effects causes a non-radial lateral distribution function of the radio signal. Therefore, the strength of the radial component of the electric field has to be taken into account in a lateral distribution function.

The results obtained in this thesis are limited by the frequency bandwidth of our setup, and the range of air shower parameters that were probed. However, within these limitations, an empirical relation between the polarization angle in the horizontal plane and the event geometry is obtained:

$$\phi_p = \tan^{-1}\left(\frac{\sin\phi_G + \frac{a_{38} f(\theta) g(d)}{R_B |\sin\alpha|}\sin\phi_C}{\cos\phi_G + \frac{a_{38} f(\theta) g(d)}{R_B |\sin\alpha|}\cos\phi_C}\right), \tag{7.1}$$

which can be tested globally when correcting for the strength of the local geomagnetic field

$$R_B = \frac{B_{\text{local}}}{B_{\text{Malargüe}}}. \tag{7.2}$$

The dependence of a on the distance to shower axis d is described by $g(d)$, which in the limitations of our measurement range can be approximated by $g(d) = 1$. The zenith angle dependence of the relative strength is approximated with a simple linear function

$$f(\theta) = 1.94 - 0.025\,\theta \tag{7.3}$$

The relative strength at 38° of the charge-excess contribution is $a_{38} = 0.139 \pm 0.01$. If the direction and location of the shower axis are known, ϕ_C, ϕ_G and α are easily obtained.

Appendix A

Validation of the estimation of the uncertainty on a

To validate the method for estimating the uncertainty on $\bar{a}$, a set of pseudo-experiments is generated with similar properties as the data. Random samples are drawn from a gaussian distribution with mean $\bar{a}$ and width σ_G. For each pseudo experiment $N = 87$ values a_i are drawn, which corresponds to the number of measured signals. To each a_i a higher bound $\sigma_{h,i}$ and lower bound $\sigma_{l,i}$ on the uncertainties are assigned. They are randomly drawn from a fit to the distribution of uncertainties on the measurements (σ_i). For each a_i an additional value c is drawn from a gaussian function with width 1 and mean 0. If c is negative then we add $c \times \sigma_{h,i}$ to the value a_i, if c is positive then $c \times \sigma_{l,i}$ is added to a_i. This gives the additional spread on a_i due to the measurement uncertainty. Applying this to each a_i provides us with one pseudo experiment. From a pseudo experiment $\bar{a}$, σ_S and σ_w can be calculated (see section 6.3.3). By repeating the pseudo experiment K times, the distributions of $\bar{a}$, σ_S and σ_w are obtained. The root mean square (RMS) of the distribution of $\bar{a}$ gives an estimate of the uncertainty on $\bar{a}$, which can be compared to the mean value of the distribution of σ_S and σ_w.

In figure A.1 $K = 1000$ pseudo experiments are generated from a Gaus-

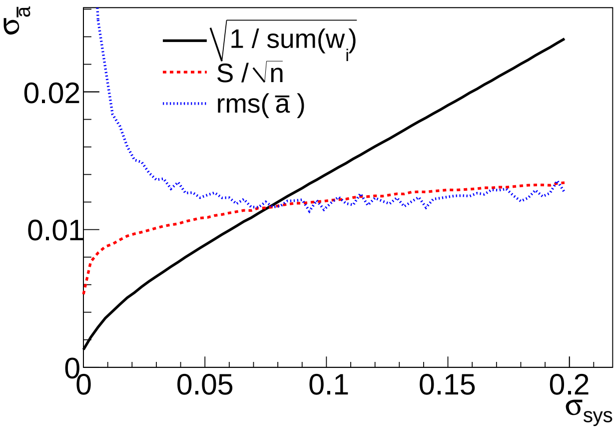

Figure A.1: Different ways to calculate the uncertainty on $\bar{a}$ as a function of σ_{sys}. Per data point in σ_{sys} 1000 pseudo experiments are generated. Displayed are the RMSs of the distribution of $\bar{a}$, the mean of the distribution of $\sigma_w = 1/\sqrt{\text{sum}(w_i)}$, and the mean of the distribution of $\sigma_S = S/\sqrt{n}$.

sian distribution with mean $\hat{a} = 0.14$ and width $\sigma_G = 0.8$. This is done for different values of σ_{sys}. The different methods of estimating the uncertainty on $\bar{a}$ converge exactly at the point where $\sigma_S = \sigma_G$. Therefore it is concluded that when $\sigma_w = \sigma_S$, the systematic uncertainty σ_{sys} is actually an estimation of the spread σ_G of the underlying distribution. However, in the case of the data, it is not possible to distinguish between the spread of the underlying distribution and an underestimate of the measurement uncertainty.

In figure A.2 $\sigma_{\bar{a}}$ is estimated at $\sigma_w = \sigma_S$ for AERA data.

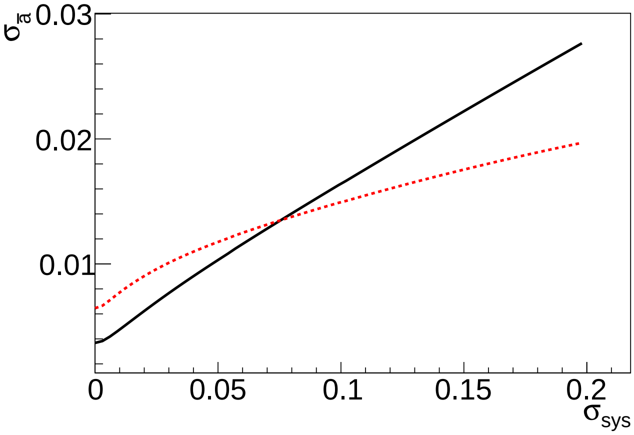

Figure A.2: At $\sigma_S = \sigma_w$ the systematic uncertainty is $\sigma_{sys} = 0.078$. The mean is estimated to be $\bar{a} = 0.115$ and the uncertainty on it $\sigma_{\bar{a}} = 0.014$.

References

[1] P. Auger, P. Ehrenfest, R. Maze, J. Daudin, and R. A. Fréon, *Extensive Cosmic-Ray Showers*, Rev. Mod. Phys. **11** (Jul, 1939) 288–291. `http://link.aps.org/doi/10.1103/RevModPhys.11.288`.

[2] J. Linsley, *Evidence for a Primary Cosmic-Ray Particle with Energy* 10^{20} *eV*, Phys. Rev. Lett. **10** (Feb, 1963) 146–148. `http://link.aps.org/doi/10.1103/PhysRevLett.10.146`.

[3] G. A. Askaryan, *Excess negative charge of an electron-photon shower and its coherent radio emission*, Sov. Phys. JETP **14** (1962) no. 2, 441–443.

[4] J. V. Jelley, J. H. Fruin, N. A. Porter, T. C. Weekes, F. G. Smith, and R. A. Porter, *Radio Pulses from Extensive Cosmic-Ray Air Showers*, Nature **205** (January, 1965) 327–328. `http://dx.doi.org/10.1038/205327a0`.

[5] I. Lerche, *Theory of Radio Pulses from Cosmic Ray Air Showers*, Nature **215** (1966) 268–269. `http://dx.doi.org/10.1038/215268a0`.

[6] F. D. Kahn and I. Lerche, *Radiation from Cosmic Ray Air Showers*, Proceedings of the Royal Society of London. Series A. Mathematical and Physical Sciences **289** (1966) no. 1417, 206–213, `http://rspa.royalsocietypublishing.org/content/289/1417/206.full.pdf+html`

`http://rspa.royalsocietypublishing.org/content/289/1417/206.abstract`.

[7] H. R. Allan, *Progress in Elementary Particles and Cosmic Ray Physics.* J. G. and Wouthuysen S. G. North-Holland, Amsterdam, 10 ed., 1971. pages 171-304, and references therein.

[8] M. Ludwig and T. Huege, *REAS3: Monte Carlo simulations of radio emission from cosmic ray air showers using an end-point formalism*, Astroparticle Physics **34** (2011) no. 6, 438 – 446. `http://www.sciencedirect.com/science/article/pii/S0927650510002094`.

[9] M. DuVernois, B. Cai, and D. Kleckner, *Geosynchrotron radio pulse emission from extensive air showers: simulations with AIRES*, Proceedings of the 29th icrc, Pune, India, 2005.

[10] J. Alvarez-Muiz, W. R. C. Jr., and E. Zas, *Monte Carlo simulations of radio pulses in atmospheric showers using ZHAireS*, Astroparticle Physics **35** (2012) no. 6, 325 – 341. `http://www.sciencedirect.com/science/article/pii/S0927650511001927`.

[11] O. Scholten, K. Werner, and F. Rusydi, *A macroscopic description of coherent geo-magnetic radiation from cosmic-ray air showers*, Astroparticle Physics **29** (2008) no. 2, 94 – 103. `http://www.sciencedirect.com/science/article/pii/S0927650507001703`.

[12] T. Huege, M. Ludwig, O. Scholten, and K. de Vries, *The convergence of EAS radio emission models and a detailed comparison of REAS3 and MGMR simulations*, Nuclear Instruments and Methods in Physics Research Section A: Accelerators, Spectrometers, Detectors and Associated Equipment (2010) no. 0, –. `http://www.sciencedirect.com/science/article/pii/S0168900210025040`.

[13] K. D. de Vries, A. M. van den Berg, O. Scholten, and K. Werner, *The lateral distribution function of coherent radio emission from extensive air showers: Determining the chemical composition of cosmic rays*,

Astroparticle Physics **34** (2010) no. 5, 267 – 273. `http://www.sciencedirect.com/science/article/pii/S092765051000143X`.

[14] K. D. de Vries, A. M. van den Berg, O. Scholten, and K. Werner, *Coherent Cherenkov Radiation from Cosmic-Ray-Induced Air Showers*, Phys. Rev. Lett. **107** (Aug, 2011) 061101. `http://link.aps.org/doi/10.1103/PhysRevLett.107.061101`.

[15] J. D. Jackson, *Classical Electrodynamics.* John Wiley and sons. Inc, third ed., 1999.

[16] T. Huege and H. Falcke, *Radio emission from cosmic ray air showers: Coherent geosynchrotron radiation*, A&A **412** (2003) no. 1, 19– 34.

[17] K. Greisen, *Progess in Cosmic Ray Physics.* North Holland, 1956.

[18] K. Kamata and J. Nishimura, *The Lateral and the Angular Structure Functions of Electron Showers*, Progress of Theoretical Physics Supplement **6** (1958) 93–155. `http://ptp.ipap.jp/link?PTPS/6/93/`.

[19] M. Dova, L. Epele, and A. Mariazzi, *The effect of atmospheric attenuation on inclined cosmic ray air showers*, Astroparticle Physics **18** (2003) no. 4, 351 – 365. `http://www.sciencedirect.com/science/article/pii/S0927650502001500`.

[20] The Pierre Auger Collaboration, *The surface detector system of the Pierre Auger Observatory*, Nuclear Instruments and Methods in Physics Research Section A: Accelerators, Spectrometers, Detectors and Associated Equipment **586** (2008) no. 3, 409 – 420. `http://www.sciencedirect.com/science/article/pii/S0168900207024680`.

[21] The Pierre Auger Collaboration, *The fluorescence detector of the Pierre Auger Observatory*, Nuclear Instruments and Methods in Physics Research Section A: Accelerators, Spectrometers, Detectors and Associated Equipment **620** (2010) no. 2-3, 227 – 251.

`http://www.sciencedirect.com/science/article/pii/S0168900210008727`.

[22] P. W. Gorham, N. G. Lehtinen, G. S. Varner, J. J. Beatty, A. Connolly, P. Chen, M. E. Conde, W. Gai, C. Hast, C. L. Hebert, C. Miki, R. Konecny, J. Kowalski, J. Ng, J. G. Power, K. Reil, L. Ruckman, D. Saltzberg, B. T. Stokes, and D. Walz, *Observations of microwave continuum emission from air shower plasmas*, Phys. Rev. D **78** (Aug, 2008) 032007. `http://link.aps.org/doi/10.1103/PhysRevD.78.032007`.

[23] The Pierre Auger Collaboration, *Microwave detection of cosmic ray showers at the Pierre Auger Observatory*, in *32nd international cosmic ray conference, Beijing 2011.* 2011. `http://arxiv.org/abs/1107.4807v1`.

[24] The Pierre Auger Collaboration, *Autonomous detection and analysis of radio emission from air showers at the Pierre Auger Observatory*, in *32nd international cosmic ray conference, Beijing 2011.* 2011. `http://arxiv.org/abs/1107.4807v1`.

[25] O. Kromer, *Empfangssytem zur Radioobservation hochenergetischer komischer Schauren und sein Verhalten bei Selbstriggerung.* PhD thesis, Rijksuniveristeit Groningen, 2008.

[26] A. M. van den Berg, J. Coppens, S. Harmsma, S. de Jong, M. Leuthold, and C. Timmermans, *First detection of radio signals from cosmic rays at the Pierre Auger Observatory*, *Internal Publication Pierre Auger Observatory*, GAP 2007- 65, 2007.

[27] J. Coppens, for the Pierre Auger Observatory, *Observation of radio signals from air showers at the Pierre Auger Observatory*, Nuclear Instruments and Methods in Physics Research Section A: Accelerators, Spectrometers, Detectors and Associated Equipment **604** (2009) no. 1-2, Supplement, S41 – S43. `http://www.`

`sciencedirect.com/science/article/pii/S0168900209004732`. ARENA 2008.

[28] H. Schoorlemmer, A. van den Berg, J. Coppens, E. D. Fraenkel, S. Grebe, S. Harmsma, S. de Jong, and C. Timmermans, *Measurements of the radio background between 30 and 80 MHz*, *Internal Publication Pierre Auger Observatory*, gap 2009- 53, 2009.

[29] S. Harmsma, *Radio signals of cosmic-ray-induced air showers at the Pierre Auger Observatory.* PhD thesis, Rijksuniveristeit Groningen, 2011.

[30] J. Coppens, *Cosmic rays are on the air: Studying the properties of radio signals from cosmic-ray induced air showers.* PhD thesis, Radboud universiteit Nijmegen, 2011.

[31] A. Aminaei, A. M. van den Berg, J. Coppens, W. Doctors, H. Falcke, E. D. Fraenkel, S. Grebe, S. Harmsma, J. R. Horhandel, S. de Jong, A. Nelles, O. Scholten, H. Schoorlemmer, C. Timmermans, K. D. de Vries, and G. Zarza, *Physics data set from MAXIMA*, *Internal Publication Pierre Auger Observatory*, gap 2011- 009, 2011.

[32] S. Argiro, S. Barroso, J. Gonzalez, L. Nellen, T. Paul, T. Porter, L. P. Jr., M. Roth, R. Ulrich, and D. Veberic?, *The offline software framework of the Pierre Auger Observatory*, Nuclear Instruments and Methods in Physics Research Section A: Accelerators, Spectrometers, Detectors and Associated Equipment **580** (2007) no. 3, 1485 – 1496. `http://www.sciencedirect.com/science/article/pii/S0168900207014106`.

[33] The Pierre Auger Collaboration, *Advanced functionality for radio analysis in the Offline software framework of the Pierre Auger Observatory*, Nuclear Instruments and Methods in Physics Research Section A: Accelerators, Spectrometers, Detectors and Associated Equipment **635** (2011) no. 1, 92 – 102. `http://www.sciencedirect.com/science/article/pii/S0168900211001276`.

[34] M. Erdmann, S. Fliescher, O. Seeger, and K. Weidenhaupt, *Absolute Calibration of the Small Black Spider Antenna for the Pierre Auger Observatory*, *Internal Publication Pierre Auger Observatory*, gap 2011- 002, 2011.

[35] G. Burke, A. Poggio, and N. O. S. C. S. D. CA., *Numerical Electromagnetic Code (NEC)-Method of Moments. A User-Oriented Computer Code for Analysis of the Electromagnetic Response of Antennas and other Metal Structures. Part I. Program Description-Theory. Part II. Program Description-Code. Volume 1. Revised.* Defense Technical Information Center, 1977. `http://books.google.nl/books?id=bYOHNwAACAAJ`.

[36] *SD reconstruction*, `http://www.auger.org.ar/CDAS/Herald/`.

[37] E. W. Weisstein, *Apodization Function*, From mathworld, a wolfram web resource `http://mathworld.wolfram.com/ApodizationFunction.html`.

[38] B. Fuchs, D. Fraenkel, T. Huege, and M. Melissas, *A comparison of the reconstructed E-field from BLS radio data with simulations based on Offline*, *Internal Publication Pierre Auger Observatory*, GAP 2011- 135, 2011.

[39] N. Mandolesi, G. Morigi, and G. Palumbo, *Radio pulses from extensive air showers during thunderstorms, the atmospheric electric field as a possible cause*, Journal of Atmospheric and Terrestrial Physics **36** (1974) no. 8, 1431 – 1435. `http://www.sciencedirect.com/science/article/pii/0021916974902219`.

[40] S. Buitink et al., *Amplified radio emission from cosmic ray air showers in thunderstorms*, A&A **467** (2007) no. 2, 385–394. `http://dx.doi.org/10.1051/0004-6361:20066006`.

[41] M. Melissas, T. Huege, and H. Schieler, *Weather monitoring at the central radio station*, *Internal Publication Pierre Auger Observatory*, GAP 2011- 66, 2011.

[42] D. Ardouin and *et al*, *Geomagnetic origin of the radio emission from cosmic ray induced air showers observed by CODALEMA*, Astroparticle Physics **31** (2009) no. 3, 192 – 200. `http://www.sciencedirect.com/science/article/pii/S0927650509000140`.

[43] E. D. Fraenkel, K. D. de Vries, W. Docters, O. Scholten, and A. M. van den Berg, *Observation of the charge-excess effect in cosmic-ray-induced radio pulses*, *Internal Publication Pierre Auger Observatory*, GAP 2011- 097, 2011.

[44] A. Fitzner, *Accuracy tests and a new angular reconstruction using surface detector data*, *Internal Publication Pierre Auger Observatory*, gap 2009- 53, 2009. `http://www.ru.nl/publish/pages/557611/hen-469.pdf`.

[45] J. H. Hough and J. R. Prescott, *Mechanisms for radio emission associated with extensive air showers*, in *Proceedings of the VI interamerican seminar on cosmic rays, La Paz, Bolivia.* 2011.

[46] D. Saltzberg, P. Gorham, D. Walz, C. Field, R. Iverson, A. Odian, G. Resch, P. Schoessow, and D. Williams, *Observation of the Askaryan Effect: Coherent Microwave Cherenkov Emission from Charge Asymmetry in High-Energy Particle Cascades*, Phys. Rev. Lett. **86** (Mar, 2001) 2802–2805. `http://link.aps.org/doi/10.1103/PhysRevLett.86.2802`.

Summary

In this thesis the polarization of radio signals emitted by extensive air showers is studied. The polarization of the radio signal depends on the emission mechanisms.
In chapter 2, the theoretical foundation of radio emission from extensive air showers is explained. There are two emission mechanisms identified that contribute to the radio signal: One is due to the deflection of charges in the geomagnetic field. The change of the current in the atmosphere results in radiation in the MHz domain. The other emission mechanism describes the radiation due to a buildup of a negative charge excess in the shower front. The radiation from the geomagnetic emission will be polarized perpendicular to the geomagnetic field and the direction of the shower axis, while the charge-excess emission will be polarized towards the shower axis. Combining the emission from both mechanisms leads to a circular component in the polarization and influences the direction of the polarization.
In chapter 3, a short overview of the Pierre Auger Observatory is given, after which the three radio detectors that delivered data for this thesis are described. Two of them were operated near the balloon launching station, and functioned as prototypes for the AERA (Auger Engineering Radio Array), while the third one is the first stage of AERA.
From the measured radio signals, the time-dependent electric field at the location of a radio station is reconstructed using the Offline software package.
In chapter 4, the selection of coinciding radio and surface detector events is explained. The radio part of these measurements is cleaned from the

influence of narrowband transmitters, and the signal regions are identified. The events are separated according the atmospheric electric field conditions under which they were measured.

In chapter 5, polarization parameters are obtained from the measured time series. The complex propagation of the time series is obtained by a Hilbert transformation. Using this complex representation, the polarization of a signal can be described with the Stokes parameters. By estimating the covariances from a background region in the time series, the uncertainties on the Stokes parameters are obtained. Simulated radio pulses with superimposed simulated noise are used to validate the calculation of the uncertainties. The biases introduced on the Stokes parameters by background noise are identified and corrected for. From the Stokes parameters, the polarization angle in the horizontal plane is obtained. The polarization angle depends only on the linearly polarized part of the signal. Therefore, a signal to noise ratio depending on the amount of linear polarization is defined, SNR_L. It is shown that for an $\mathrm{SNR}_L > 2$, the estimated uncertainty on the polarization angle is reliable.

In chapter 6, the polarization angle obtained from measured radio signals is used to study the emission mechanisms. The expected polarization angle for geomagnetic emission, ϕ_G, is easily obtained when the shower axis and the orientation of the geomagnetic field are known. The polarization angle obtained from the measurements,ϕ_p, from all setups show a clear correlation with ϕ_G. This confirms the leading contribution of the geomagnetic emission to the radio signal. However, fitting a simple linear function indicates that geomagnetic emission alone cannot explain the polarization angle obtained from the measurements.

The polarization angle from measurements show a large deviation from ϕ_G during thunderstorms. This provides the first observation that not only the amplitude of the radio signal is affected by thunderstorms, but also its polarization.

The radiation of a charge-excess contribution is polarized radially towards the shower axis. Therefore, it depends on the location of the radio detector station. The orientation of a radio detector station with respect to the shower axis is described by the observer angle ϕ_{obs}. If the deviation from the geomagnetic polarization angle $\phi'_p = \phi_p - \phi_G$ is due to a charge-excess contribution, one expect a periodic behavior of ϕ'_p with the ϕ_{obs}. This polarization signature is observed in the measurements from all setups. This gives a qualitative indication that ϕ'_p is polarized radially inwards, as expected for the charge-excess contribution.

From the geometry of the event the relative strength a of the radial contribution with respect to the geomagnetic contribution to the electric field is estimated for each measurement. After correction for the dependence of the geomagnetic emission on alpha, it was noted that the method for determining a depends on the angle between both emission mechanisms. When using only data with a large angle between both mechanisms, an additional dependence on the zenith angle of the air shower was found. Such a dependence was also qualitatively seen in simulations. However it appears stronger in data. After correcting a for the zenith angle dependence to a zenith angle of 38 degrees, we find that $a_{38} = 0.139 \pm 0.01$. For each measurement we are left with an unexplained systematic uncertainty of 0.03, which could be due to an underestimate of uncertainties on the core position of the SD reconstruction. For the measurements in the MAXIMA 2010 data set MGMR simulations have been generated. For these events a one-to-one comparison between measurements and simulations is performed. Including charge-excess into the simulations results in better agreement between measurement and simulation. However, the overall agreement between measurement and simulation is still poor at best. The lack of agreement between data and simulations might be due to a unreliable SD-reconstruction from which the simulations are generated. To get a more fair comparison between measurement and simulations it would be nice to compare the simulations to the measurements from AERA. However, these simulations were not available at the time of writing this thesis. The radially inwards polarized signal observed in this thesis indicates the first observation of Askaryan radiation outside the laboratory. The analysis in this thesis led to an empirical relation between event geometry and polarization angle that can be tested elsewhere in the world.

Samenvatting

Een eeuw geleden, in 1912, maakte Victor Hess ballonvluchten en nam een elektrometer mee aan boord. Hoe hoger hij vloog met zijn ballon, hoe sneller zijn elektrometer zich ontlaadde. Hij concludeerde hieruit dat er straling van boven moest komen. Deze straling is vandaag de dag bekent onder de naam kosmische straling en bestaat uit subatomaire deeltjes die uit de ruimte komen.

Sommige deeltjes van de kosmische straling hebben een enorm hoge energie. Als de energie hoog genoeg is, ontstaat er door interacties in de atmosfeer een deeltjeslawine die op het aardoppervlak te meten is. Deze deeltjeslawines werden in 1932 ontdekt door Pierre Auger. Naar hem is het grootste kosmische straling observatorium ter wereld vernoemt: Het Pierre Auger Observatorium op de Pampa Amarilla in Argentinië.

Naarmate de energie van de kosmische straling hoger wordt neemt de flux af. Daarom is een groot oppervlakte nodig om kosmische straling met extreem hoge energie efficiënt te detecteren. Het Pierre Auger Observatorium combineert verschillende detectie technieken: Deeltjesdetectors beslaan een oppervlakte van 3000 km^2 en meten de afdruk van de deeltjeslawines op de grond. Hieruit wordt de energie en de richting van de kosmische straling bepaald. Aan de rand van dit gebied staan op vier locaties gebouwen met fluorescentie telescopen. Deze meten het ultraviolette licht dat wordt uitgestraald door atmosferische stikstof atomen die aangeslagen zijn door interactie met de deeltjeslawine. Door de ontwikkeling van de deeltjeslawine in de atmosfeer te meten kunnen we afschatten uit welk type deeltjes de kosmische straling bestaat. De fluorescentie telescopen kunnen alleen meten tijdens maanloze heldere nachten.

Momenteel worden op het Pierre Auger Observatorium andere technieken ontwikkeld die mogelijk ook een meting geven van de aard van de kosmische straling. Een van deze technieken maakt gebruik van radio antennes die gevoelig zijn tussen 30-80 MHz en is het onderwerp van dit proefschrift.

Coherente radio straling van deeltjeslawines werd 50 jaar geleden door Askaryan voorspeld. Deze straling wordt veroorzaakt doordat er negatieve lading wordt opgebouwd wanneer de deeltjeslawine door de atmosfeer propageert. Kort daarna werd door Jelley korte radio pulsen afkomstig van deeltjeslawines waargenomen. In de jaren na de eerste observatie werd met verschillende experimenten meer data vergaard, daardoor werd het noodzakelijk om de stralingsprocessen beter te modelleren. Kahn en Lerche stelde dat straling ontstaat wanneer de geladen deeltjes in de deeltjeslawine worden afgebogen in het aardmagneetveld. De straling die op deze manier geproduceerd is heeft een andere polarisatie dan de straling die je zou verwachten door de negatieve ladingsopbouw: De *aardmagnetische-straling* is gepolariseerd loodrecht op het aardmagneetveld en de richting waarin de deeltjeslawine beweegt. Terwijl de *negatieve-ladings-straling* gepolariseerd is in de richting van de deeltjeslawine-as, waarbij we de deze as definiëren als de as waarlangs het centrum van de deeltjeslawine zich beweegt.

Aan het begin van deze eeuw beleefde de radiodetectie van kosmische straling een wederopstanding. De aanleiding hiervoor was de mogelijkheid om het signaal digitaal te verwerken en vooruitgang die gemaakt werd door het modelleren van deeltjeslawines met behulp van Monte Carlo simulaties. Verscheidende experimenten bevestigen de aardmagnetische contributie tot de straling.

Om het radio signaal te kalibreren tegen andere metingen, is besloten om het Pierre Auger Observatorium uit te breiden met een radiodetector: de Auger Engeneering Radio Array (AERA). Deze radiodetector gaat bestaan uit 160 stations die antennes hebben met twee polarisaties armen. In het totaal gaat AERA een oppervlakte 20 km^2 beslaan, inmiddels zijn 21 antennes van de eerste fase geïnstalleerd. In dit proefschrift zijn de metingen geanalyseerd die genomen zijn met deze stations en met een aantal prototypes radiodetectors.

Een typisch radio signaal bestaat uit een puls in het elektrische veld die in de orde van 50 ns duurt. De eigenschap die wij uit deze puls halen is de oriëntatie van de horizontale component van het elektrische veld. De oriëntatie wordt beschreven door de polarisatie hoek. De geometrie, oftewel de locatie en de aankomstrichting, van de deeltjeslawine kan worden bepaald met behulp van de deeltjesdetectors. De polarisatie hoek die je verwacht door het aardmagnetische emissiemechanisme kan bepaald worden uit de aankomstrichting van de van de deeltjeslawine. Bij het vergelijken van de verwachte polarisatie hoek met de gemeten polarisatie nemen we een duidelijke correlatie waar. Dit bevestig de dominante rol van het aardmagnetische emissiemechanisme. Echter, de spreiding op deze correlatie geeft een indicatie dat er mogelijk andere contributies bijdragen aan de waargenomen straling.

We kunnen de locatie van de radio antennes op de grond beschrijven ten opzichte van de deeltjeslawine-as in poolcoördinaten, oftewel een afstand tot de as en een hoek in het vlak waarin de antennes staan. Als we de afwijking van de gemeten polarisatiehoek ten opzichte van de aardmagnetische polarisatiehoek uitzetten tegen de hoek van de antenne, dan zien we een patroon ontstaan dat te verwachten is voor een contributie die gepolariseerd is in de richting van de deeltjeslawine-as, oftewel een bijdrage die je zou verwachten door *negatieve-ladings-straling*.

Na deze kwalitatieve observatie willen we natuurlijk weten hoe significant deze bijdrage is, en wat de sterkte is ten opzichte de aardmagnetische straling is. Doordat we de geometrie van de deeltjeslawine uit de metingen van de deeltjesdetectors van het observatorium weten, kunnen we de polarisatie van de afzonderlijke contributies bereken. Door de polarisatiehoek te meten kunnen we uitrekenen wat de relatieve sterkte van beide contributies is. De sterkte van de aardmagnetische straling hangt af van de hoek tussen de deeltjeslawine-as en het aardmagneetveld. Voor deze afhankelijkheid corrigeren we zodat de sterkte van de aardmagnetische straling maximaal zou zijn. Zodoende kunnen de relatieve sterkte van afzonderlijke deeltjeslawines met elkaar vergelijken. De gemiddelde relatieve sterkte van de *negatieve-ladings-straling* ten opzichte van de *aardmagnetische-straling* is $11.5 \pm 1.4\%$. De spreiding van de relatieve sterkte wordt geschat op 7.8 %.

Gedeeltelijk komt deze spreiding doordat onzekerheden worden onderschat als wanneer de elektrische velden van beide effect parallel zijn. Als we door een eenvoudige snede deze metingen niet meenemen komen we op een gemiddelde van 11.9 ± 1.3%. De spreiding in het sample neemt af tot 5.4%.
Op de overgebleven metingen hebben we de afhankelijkheid onderzocht naar verschillende parameters. De sterkste correlatie tussen de relatieve sterkte van beide contributies is gevonden met de zenithoek, de sterkte van de *negatieve-ladings-straling* neemt af naarmate de deeltjeslawines horizontaler binnenkomen.
In het laatste stuk van dit proefschrift vergelijken de polarisatie van de metingen met de polarisatie van gesimuleerde radio emissie. Uit deze vergelijking is het evident dat wanneer we *negatieve-ladings-straling* toevoegen aan het model, de overeenkomt met de data verbeterd. Echter, het is ook duidelijk dat de afwijking van het model ten opzichte van de metingen nog te groot zijn. We weten dat dit model nog niet compleet is, bijvoorbeeld wordt het effect van de brekingsindex van de atmosfeer nog niet meegenomen.
In dit proefschrift hebben we aangetoond dat er een radiaal gepolariseerde contributie bijdraagt aan het radio signaal van deeltjeslawines. Tevens hebben we enkele afhankelijkheden van deze contributie in kaart gebracht. Deze meting draagt bij aan het voortschrijdende inzicht in de oorsprong van het radio signaal dat geassocieerd kan worden met deeltjeslawines tengevolge van kosmische straling.

Acknowledgements

All things come to an end, also this thesis. Although, for some (most) readers this might be actually the first and only chapter they will read. This thesis wouldn't be complete without thanking a lot of people. Some of them contributed directly to the content of this thesis, while others were taking care of me while I needed to do something else than writing a thesis. First of all, I would like to thank my supervisor, Charles Timmermans. In the last 5 years, we had a blast working and laughing together. I learned a lot! Also a special thanks to my promoter Sijbrand de Jong. We had interesting physics discussions, and organizing a dance party steered by cosmic rays was a unique experience.

I had the pleasure of sharing "the loudest office in the building" with several people. Due to Jose and german Stefan our office turned into a duck shooting range, decorated with german flags and male-bimbo calendars. I'm thankful that we had nice students, which really contributed to the great atmosphere: Antje, Margot, Marie, Kimmely, Katherina, & Jeroen, bedankt! Luckily, I know that with the arrival of Guus and non-german Stefan, the reputation of our office will be in good hands. Enjoy it!

This period would have not been so much fun without my close friends and colleagues, Geert-Jan, Irene, Marcel, Magda, Melvin, Thijs and Yiannis. I think we were/are a unique group and we made the bars in Nijmegen flourish during my PhD research. I will miss the coffee breaks, together with you guys, and Annelies, Gemma, and Marjo. I'm curious to see where we all will be in five years.

Outside the university there have been numerous people, with whom I cy-

cled, traveled, partied, canoed, skied, and just had fun. I won't mention you name by name, because that will cost me a few extra pages. You know who you are! Thank you for showing me a good time, and good times will be ahead of us. A special thanks to my father, mother and brothers, who always have supported me and it is good to know that you always have a place that you can call home.
A final word to some-one special, Christina. Living so far from each other doesn't make things easy, but I enjoyed every minute when we were together. We both know that we have something special going on. Let us see what the future has in store for us.

We will keep in touch! Harm

Curriculum Vitae

Harm Schoorlemmer was born on the 8th of January 1983 in Bennebroek, the Netherlands. From September 2001 till January 2008 he studied physics and astronomy at the Radboud University in Nijmegen. In addition to his study he attended the two years interdisciplinary Honours program, which he finished in 2005. In 2007 he was CERN summer school student for a period of 11 weeks. In January 2008 he finished his master thesis on the correlation between cosmic rays and pulsars and magnetars.
In February 2008 he started his four years of PhD research at the Radboud University Nijmegen under the supervision of Prof. Dr. Sijbrand de Jong and Dr. Charles Timmermans. The topic of this research was radio detection of cosmic rays at the Pierre Auger Observatory in Argentina. He worked on several prototypes radio detectors and the first stage of the Auger Engineering Radio Array (AERA). His work included software development, data analyses and fieldwork. The main goal of his thesis was to understand the radio emission mechanisms using the polarization of the measured signals.
During his PhD he won the competition of the 'Academische Jaarprijs' as a member of the team *Cosmic Sensation*. From the awarded 100.000 euro they organized a three day festival at which music and video were steered by cosmic rays. It was visited by ±2300 people. Currently, he is employed as a junior researcher at the Radboud University Nijmegen.

List of publications

As a member of the Pierre Auger Collaboration

- “Limit on the diffuse flux of ultrahigh energy tau neutrinos with the surface detector of the Pierre Auger Observatory”, *The Pierre Auger Collaboration*, **Physical Review D 79, 102001 (2009)**.
- “Upper limit on the cosmic-ray photon fraction at EeV energies from the Pierre Auger Observatory”, *The Pierre Auger Collaboration*, **Astroparticle Physics 31 (2009) 399-406**
- “Atmospheric effects on extensive air showers observed with the surface detector of the Pierre Auger observatory”, *The Pierre Auger Collaboration*, **Astroparticle Physics 32 (2009) 89-99**
- “Trigger and aperture of the surface detector array of the Pierre Auger Observatory”, *The Pierre Auger Collaboration*, **Nuclear Instruments and Methods in Physics Research A613 (2010) 29-39**
- “A study of the effect of molecular and aerosol conditions in the atmosphere on air fluorescence measurements at the Pierre Auger Observatory”, *The Pierre Auger Collaboration*, **Astroparticle Physics 33 (2010) 108-129**
- “Measurement of the energy spectrum of cosmic rays above 10^{18} eV using the Pierre Auger Observatory, *The Pierre Auger Collaboration*,

Physics Letters B 685 (2010) 239-246

- “Measurement of the Depth of Maximum of Extensive Air Showers above 10^{18} eV”, *The Pierre Auger Collaboration*, **Physical Review Letters, 104, 091101 (2010)**
- “The northern site of the Pierre Auger Observatory”, *The Pierre Auger Collaboration*, **New Journal of Physics 12 (2010) 035001**
- “The fluorescence detector of the Pierre Auger Observatory”, *The Pierre Auger Collaboration*, **NIM A 620 (2010) 227-251**
- “Update on the correlation of the highest energy cosmic rays with nearby extragalactic matter”, *The Pierre Auger Collaboration*, **Astroparticle Physics 34 (2010) 314-326**
- “The exposure of the hybrid detector of the Pierre Auger Observatory”, *The Pierre Auger Collaboration*, **Astroparticle Physics 34 (2011) 368-381**
- “The Pierre Auger Observatory Scaler Mode for the Study of the Modulation of Galactic Cosmic Rays due to Solar Activity”, *The Pierre Auger Collaboration* , **JINST 6, P01003 (2011)**
- “Search for First Harmonic Modulation in the Right Ascension Distribution of Cosmic Rays Detected at the Pierre Auger Observatory”, *The Pierre Auger Collaboration*, **Astropart. Phys. 34 (2011), 627-639**
- “Advanced functionality for radio analysis in the Offline software framework of the Pierre Auger Observatory”, *The Pierre Auger Collaboration* , **Nuclear Instruments and Methods in Physics Research A 635 (2011) 92-102**
- “Anisotropy and chemical composition of ultra-high energy cosmic rays using arrival directions measured by the Pierre Auger Observatory”, *The Pierre Auger Collaboration*, **JCAP06 (2011) 022**

- “The Lateral Trigger Probability function for UHE Cosmic Rays Showers detected by the Pierre Auger Observatory”, *The Pierre Auger Collaboration*, **Astroparticle Physics 35 (2011) 266-276**

- “The effect of the geomagnetic field on cosmic ray energy estimates and large scale anisotropy searches on data from the Pierre Auger Observatory”, *The Pierre Auger Collaboration*, **JCAP 11 (2011) 022**

- “Search for ultrahigh energy neutrinos in highly inclined events at the Pierre Auger Observatory”, *The Pierre Auger Collaboration*, **Physical Review D 84, 122005 (2011)**

- “Search for signatures of magnetically-induced alignment in the arrival directions measured by the Pierre Auger Observatory”, *The Pierre Auger Collaboration*, **Astroparticle Physics 35 (2012) 354**

- “Description of Atmospheric Conditions at the Pierre Auger Observatory using the Global Data Assimilation System (GDAS)”, *The Pierre Auger Collaboration*, **Astroparticle Physics, in press (2012)**

Conference proceedings

- “Results from polarization studies of radio signals induced by cosmic rays at the Pierre Auger Observatory”, *H. Schoorlemmer for the Pierre Auger Collaboration*, Proceeding of 4th International workshop on Acoustic and Radio EeV Neutrino detection Activities, 2012, Published in NIM A, DOI: 10.1016/j.nima.2010.11.145

- “Cosmic rays detected with the Auger Engineering Radio Array”,*H. Schoorlemmer for the Pierre Auger Collaboration*, Proceedings of 13th ICATPP Conference on Astroparticle, Particle, Space Physics and Detectors for Physics Applications, In press in World scientific

Internal publications

- “Simulation of an Array of Antenna Detectors”,*T. Asch, M. Erdmann, S. Fliescher, T. Huege, M. Leuthold, J. Rautenberg, H. Schoorlemmer, K. Weidenhaupt, T. Winchen*, 2008, **nr. 177**

- “Measurements of the radio background between 30 and 80 MHz”,*H. Schoorlemmer, A.M. van den Berg, J. Coppens, E. D. Fraenkel, S. Grebe, S. Harmsma, S. de Jong, C. Timmermans*, 2009, **nr. 53**

- “The impact of RFI suppression on signal-to-noise calculations of events measured with the radio detection stations near the BLS”, *S. Grebe, H. Schoorlemmer*, 2009, **nr. 69**

- “Angular reconstruction with less than three SD stations using relative PMT signals”, *A. Fitzner, S. Grebe, H. Schoorlemmer, C. Timmermans*, 2010, **nr. 53**

- “The radio extension of Auger Offline”, *S. Fliescher, D. Fraenkel, B. Fuchs, S. Grebe, T. Huege, M. Konzack, M. Melissas, P. Oliva, N. Palmieri, J. Rautenberg, A. Schmidt, H. Schoorlemmer, F. Schröder, A. Stutz, K. de Vries*, 2010, **nr. 56**

- “Description of the measured local time dependent electric field using Stokes parameters”, *H. Schoorlemmer, S. Grebe*, 2010, **nr. 90**

- “Physics data set from MAXIMA”, *A.M. van den Berg, A. Aminaei, J. Coppens, W. Docters, H. Falcke, E. D. Fraenkel, S. Grebe, S. Harmsma, J.R. Hörhandel, S. de Jong, J.L. Kelley, A. Nelles, O. Scholten, H. Schoorlemmer, C. Timmermans, K.D. de Vries, G. Zarza*, 2011, **nr. 9**

- “The effect of noise on reconstructable parameters in radio detection”, *K. Holland, S. Grebe, H. Schoorlemmer, C. Timmermans*, 2011, **nr. 21**

- “Indication for heavy nuclei from Centaurus A above 55 EeV”, *G. van Aar, S. de Jong, S. Grebe, H. Schoorlemmer, C. Timmermans*, 2011, **nr. 26**
- “First Detection of Cosmic Ray Self-Triggered Radio Pulses with AERA in Coincidence with SD and FD”, *The AERA group*, 2011, **nr. 57**
- “Polarization of radio emission from extensive air showers”, *H. Schoorlemmer , S. Grebe, S. de Jong, C. Timmermans*, 2011, **nr. 105**
- “Dependence of the radio frequency spectrum on air shower parameters”, *S. Grebe, S. de Jong, H. Schoorlemmer, C. Timmermans*, 2011, **nr. 112**
- “RdMonitoring An Offline Module to monitor the raw data from AERA”, *S. Grebe, A. Nelles, H. Schoorlemmer*, 2011, **nr. 122**
- “Strength and significance of the charge-excess contribution to radio emission from air showers”, *H. Schoorlemmer , S. Grebe, S. de Jong, C. Timmermans* , 2011, **nr. 126**